

See discussions, stats, and author profiles for this publication at: <https://www.researchgate.net/publication/24401898>

ChemInform Abstract: Coherent Multidimensional Vibrational Spectroscopy of Biomolecules: Concepts, Simulations, and Challenges

ARTICLE *in* ANGEWANDTE CHEMIE INTERNATIONAL EDITION · MAY 2009

Impact Factor: 11.26 · DOI: 10.1002/anie.200802644 · Source: PubMed

CITATIONS

101

READS

20

3 AUTHORS, INCLUDING:



Shaul Mukamel

University of California, Irvine

852 PUBLICATIONS 23,665 CITATIONS

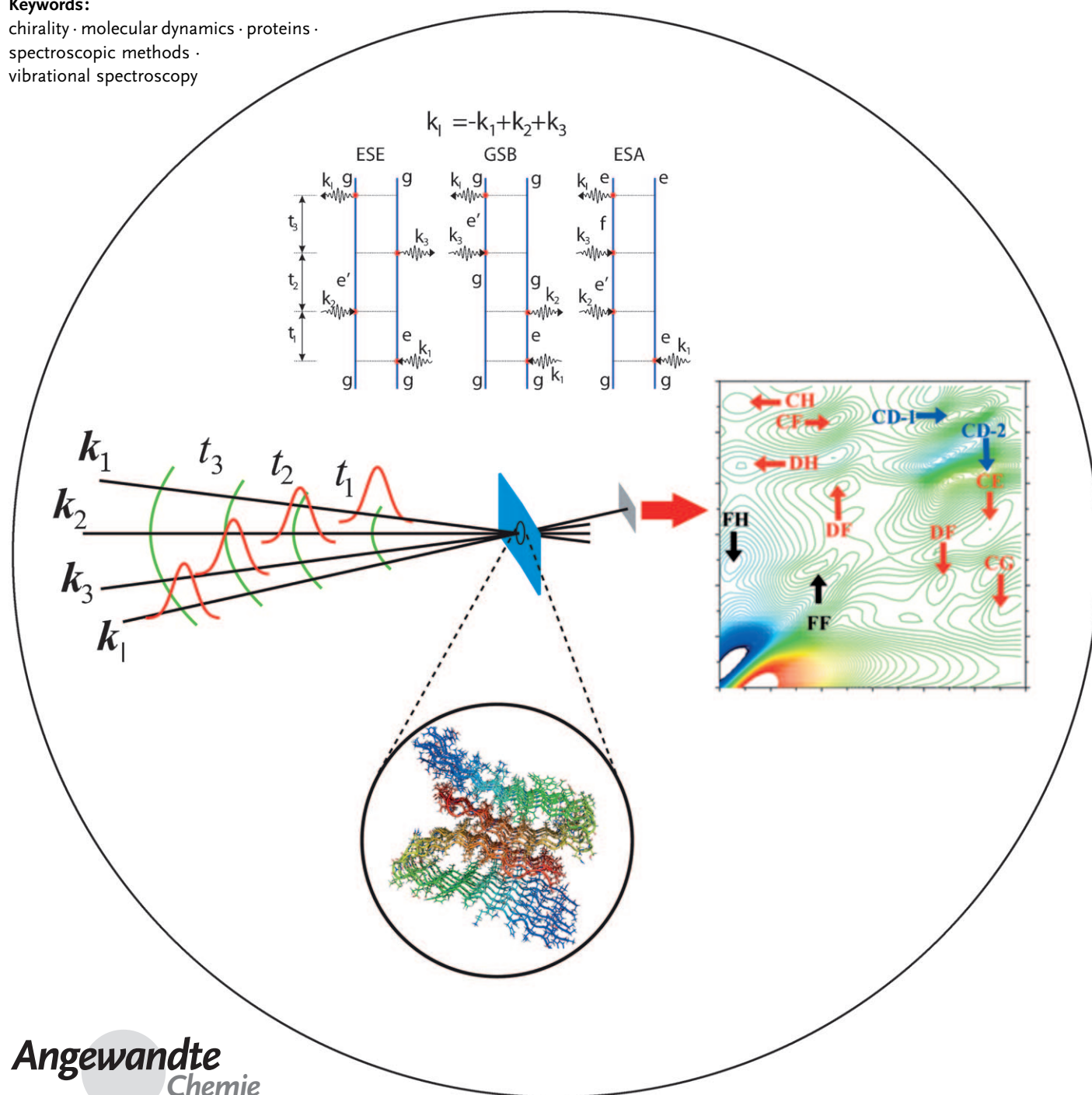
SEE PROFILE

Coherent Multidimensional Vibrational Spectroscopy of Biomolecules: Concepts, Simulations, and Challenges

Wei Zhuang, Tomoyuki Hayashi, and Shaul Mukamel*

Keywords:

chirality · molecular dynamics · proteins · spectroscopic methods · vibrational spectroscopy



The response of complex molecules to sequences of femtosecond infrared pulses provides a unique window into their structure, dynamics, and fluctuating environments. Herein we survey the basic principles of modern two-dimensional infrared (2DIR) spectroscopy, which analogous to those of multidimensional NMR spectroscopy. The perturbative approach for computing the nonlinear optical response of coupled localized chromophores is introduced and applied to the amide backbone transitions of proteins, liquid water, membrane lipids, and amyloid fibrils. The signals are analyzed using classical molecular dynamics simulations combined with an effective fluctuating Hamiltonian for coupled localized anharmonic vibrations whose dependence on the local electrostatic environment is parameterized by an ab initio map. Several simulation methods, (cumulant expansion of Gaussian fluctuation, quasiparticle scattering, the stochastic Liouville equations, direct numerical propagation) are surveyed. Chirality-induced techniques which dramatically enhance the resolution are demonstrated. Signatures of conformational and hydrogen-bonding fluctuations, protein folding, and chemical-exchange processes are discussed.

1. Introduction

The structure and function of biomolecules are intimately connected; this is one of the central principles of structural biology.^[1] Predicting protein structures requires understanding the interactions and driving forces which cause them to fold from a disordered, random-coiled, state into a unique native structure. Exploring the folding mechanism in detail requires techniques that can monitor the structures with adequate temporal and spatial resolution. X-ray crystallography can determine the static structure with atomic resolution.^[2] Time-resolved small-angle X-ray scattering gives mainly the radius of gyration with up to picosecond time resolution.^[3–6] Three-dimensional atomic-resolution structures can be determined using NMR spectroscopy^[7,8] but only on time scales longer than the radiowave period (microsecond).^[8] Higher temporal resolution is required for monitoring many elementary biophysical processes, for example, the α -helix formation,^[9] which occurs on a timescale of hundreds of nanosecond. Nanosecond to picosecond processes may sometimes be probed through the frequency dependence of NMR relaxation rates.^[10] Such measurements are indirect and their interpretation is model-dependent. Time-resolved X-ray diffraction provides picosecond snapshots of structures in crystals.^[11] Ultrafast electron pulses are being developed as well for time-resolved electron diffraction applications.^[12,13]

Over the past decade, time-resolved infrared spectroscopy carried out with 20–100 fs laser pulses has emerged as a powerful tool in the investigation of protein folding,^[14] thanks to fast laser triggering and the fairly localized nature of vibrational transitions.^[14–20] The coherent techniques surveyed

From the Contents

1. Introduction	3751
2. History of Multidimensional Vibrational Spectroscopy	3754
3. Hamiltonian Operators for the Amide Vibrations of Polypeptides	3756
4. Liouville-Space Pathways for Coupled Localized Vibrations	3760
5. Spectral Diffusion and Chemical Exchange: The Stochastic Liouville Equations	3764
6. The OH Stretch Band of Liquid Water	3766
7. Application to Phospholipids: Quasiparticle Representation of 2DIR Signals	3769
8. Double-Quantum-Coherence Spectroscopy	3772
9. Chirality Effects: Enhancing the Resolution	3772
10. The Structure of Amyloid Fibrils	3774
11. Summary and Outlook	3776

herein record the molecular response to sequences of pulses, and provide a multidimensional view of their structure. Multidimensional optical techniques are analogues of their NMR counterparts but with greatly improved temporal resolution.^[21,22] This and other differences are summarized in Table 1.^[23–25] NMR experiments are performed with intense pulses which manipulate the entire spin population. Pulse sequences involving hundreds of pulses are then possible. 2DIR studies use weak pulses which only excite a small fraction of the molecules. Unlike NMR spectroscopy, multiple intense IR pulses can trigger various photophysical and photochemical processes which are interesting on their own, but complicate the spectroscopic analysis. Therefore, in practice, only a few weak pulses are used, and the signals can be calculated perturbatively order by order in the incoming fields. The directionality of the signal (phase matching) stems from the fact that the sample is much

[*] Dr. W. Zhuang, Dr. T. Hayashi, Prof. S. Mukamel
Department of Chemistry, University of California at Irvine
CA 92697-2025 (USA)
Fax: (+1) 949-824-4759
E-mail: smukamel@uci.edu

Table 1: Comparison of coherent NMR and IR techniques.

	NMR	IR
Frequency	MHz	10^{13} – 10^{14} Hz
Time Resolution	Millisecond	Femtosecond
Hamiltonian	Spin Hamiltonian. Few universal parameters. Easier to invert spectra to get structures	Anharmonic vibrational Hamiltonian. Requires electronic structure calculation. Many parameters. Inversion of signals is more complex
Transition Dipoles	All dipoles of the same nucleus are equal and aligned. Pulse polarizations and spin states transform by rotating the sample	Varying dipole strength and orientation. Many independent parameters for the dipole
Pulse intensity	Strong saturating pulses. All spins excited, multiple pulse sequences possible	Weak, only few molecules are excited, sequences with few pulses possible
Modeling	The Bloch picture	Susceptibilities and response functions
Directionality of signal	Wavelength $\lambda \gg$ sample size, $kr \ll 1$, Signal is isotropic in space. Pathway selection by phase cycling	$\lambda \ll$ sample size, $kr \gg 1$, signal is highly directional. Pathway selection by spatial phase matching
Target degrees of freedom	Spins	Molecular vibrations
Temperature	High compared to frequencies. Simplifies calculations	Low compared to frequencies. Calculation more complicated
Phase control of pulses	Easy	Becomes harder as the frequency is increased

larger than the optical wavelength. In NMR spectroscopy the opposite limit holds: The signal is isotropic. However, the directional information may be retrieved by modifying the phases of the pulses (phase cycling). The anharmonic effective Hamiltonian necessary for 2DIR simulations is complex and requires extensive electronic-structure calculations. In contrast, the spin Hamiltonians in NMR spectroscopy are known and universal, greatly simplifying the simulations and analysis of signals. The dipole moments in NMR spectroscopy are aligned in parallel by the strong magnetic field. In contrast, the specific orientations of IR dipoles carry useful structural information that can be retrieved by varying the pulse polarizations. NMR spectroscopy has a remarkable structural resolution unmatched by IR signals. However, 2DIR provides a different window with complementary information.

A heterodyne-detected 2DIR experiment (Figure 1) involves the interaction of three laser pulses with wave vectors \mathbf{k}_1 , \mathbf{k}_2 , \mathbf{k}_3 , (in chronological order) with the peptide. The coherent signal field is generated along one of the phase-

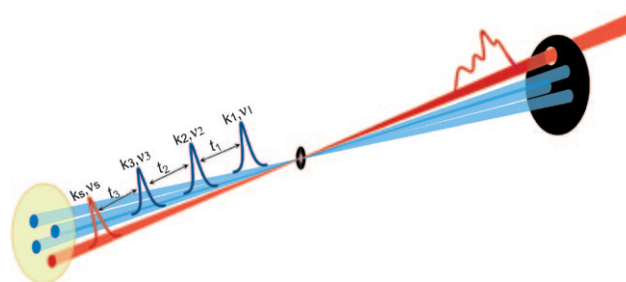


Figure 1. Pulse configuration for a heterodyne detected multidimensional four-wave mixing experiment. Signals are recorded versus the three time delays t_1 , t_2 , t_3 , and displayed as 2D correlation plots involving two of the time delays, holding the third time delay fixed [see Eq. (14)].

matching directions: $\mathbf{k}_s = \pm \mathbf{k}_1 \pm \mathbf{k}_2 \pm \mathbf{k}_3$ where all molecules emit in phase and are detected by interference with a 4th “local-oscillator” pulse with the desired wavevector \mathbf{k}_s . The signal $S(t_3, t_2, t_1)$ is given as the intensity change of the local-



Wei Zhuang studied chemistry at the University of California at Irvine until 2007, he is currently a postdoctoral fellow at University of California at Berkeley.



Tomoyuki Hayashi was born in Tokyo in 1973 and earned his PhD with Prof. Hiro-o Hamaguchi in 2002. He was an assistant specialist at University of California, Irvine until 2008. He is currently working on electron transfer in proteins at University of California, Davis with Professor Alexei Stuchebrukhov.

oscillator field induced by the interactions with the other fields. Its parametric dependence on the time intervals between pulses carries a wealth of information. 2DIR signals are typically displayed as two-dimensional correlation plots with respect to two of these intervals, say t_1 and t_3 , holding the third (t_2) fixed. Since such plots are highly oscillatory, the signal is double Fourier transformed with respect to the two desired time variables to generate a frequency–frequency correlation plot such as $S(\Omega_1, t_2, \Omega_3)$ where Ω_1 and Ω_3 are the frequency conjugates to t_1 and t_3 (Figure 1).

Heterodyne detection allows the whole signal field (both amplitude and phase) to be recorded. Thus both the real (in-phase) and the imaginary (out-of-phase) components of the response can be displayed. Coupled vibrational modes show new resonances (cross-peaks) whose intensities and profiles give direct signatures of the correlations between transitions. These are background-free features that vanish for uncoupled vibrations. Correlation plots of dynamic events taking place during controlled evolution periods can be interpreted in terms of multipoint correlation functions. These carry considerably more information than the two-point functions of linear spectroscopy, and therefore have the capacity to distinguish between possible models whose 1D responses are virtually identical.

Figure 2, shows simulated 2D photon-echo spectra of two coupled vibrations. The diagonal peaks at $(-2000, 2000)$ and $(-2100, 2100)$ resemble the linear absorption. The cross-peaks at $(-2000, 2100)$ and $(-2100, 2000)$ reveal the couplings between the two modes. The 2D line shapes are very sensitive to time scales and the degree of correlation of frequency fluctuations and provide valuable information about the fluctuating environment. Fast fluctuations (Figure 2, right panel) show circular diagonal peaks (homogeneous broadening) whereas slow fluctuations (Figure 2, left panel) yield elongated line shapes. In addition the left and middle panels of Figure 2 show strong variations of the cross-peaks with the degree of correlation. Bandshape analysis of 2D photon echoes of solute–solvent complexes showed a longer time scale for the slowest of two components in mixed solvents than in a pure solvent. This result was ascribed to composition variations of the first solvent shell.^[26] Such fine details are not available from 1D measurements.

Pump–probe (also known as transient absorption) is the simplest nonlinear experiment, both conceptually and technically since it only involves two laser pulses: the pump and the probe, and requires no phase-control. Typically, the two

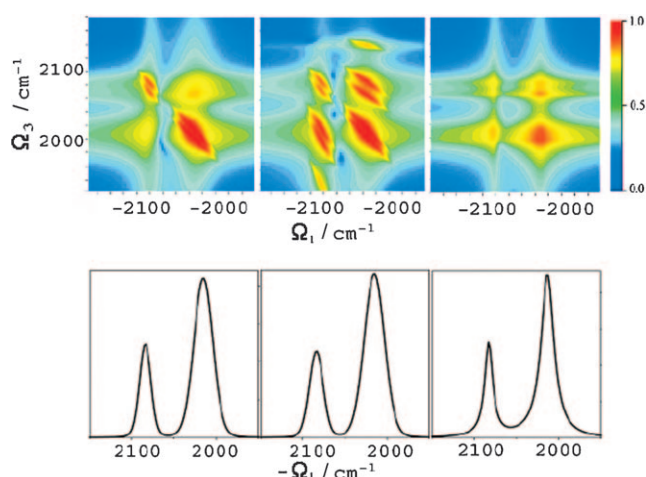


Figure 2. Top: 2D photon-echo spectra of two coupled vibrations in the phase-matching direction $\mathbf{k}_i = -\mathbf{k}_1 + \mathbf{k}_2 + \mathbf{k}_3$. Ω_1 and Ω_3 are the Fourier conjugate variables to t_1 and t_3 . The frequency fluctuations of the two modes are slow and anti-correlated (left panel), slow and correlated (middle panel), fast and anti-correlated (right panel). Adapted from ref. [27]. Bottom: Linear absorptions for the three models.

pulses are temporally well separated. The system first interacts with the pump pulse then with the probe pulse. The difference between the probe transmission with and without the pump, reveals information about structural changes and energy transport taking place during the delay between the two pulses. The Photon-echo signal generated in the direction $\mathbf{k}_s = -\mathbf{k}_1 + \mathbf{k}_2 + \mathbf{k}_3$ is another widely used technique.^[28] The excitations generated in the molecule during t_1 and t_3 acquire an opposite phase, exactly canceling inhomogeneous broadening in the signal and opening a window into motions and relaxation timescales. This is not possible with 1D techniques, such as linear absorption. Frequency-domain experiments involving longer pulses, which combine IR and Raman techniques have been carried out.^[29]

2D techniques have been widely applied towards exploring the equilibrated structures of biomolecules, monitoring peptide folding dynamics, studying the hydrogen-bonding structure and dynamics in liquid water, monitoring the electrostatic environment and its fluctuations around a chromophore, or investigating vibrational energy transfer pathways. A brief survey of these applications is presented in Section 2.

Fast peptide-folding (in the pico- to nanosecond range) has been extensively studied by Monte Carlo (MC) and molecular dynamics (MD) simulations.^[30–37] Simple lattice models^[35,36] help develop the big physical picture of the folding events, while all-atom molecular dynamics simulations^[32,37] provide more realistic and detailed information about structures and dynamics. Computational power restricts such calculations to trajectories of a few tens of nanoseconds. A 1998 study reported the protein folding with explicit representation of water for 1 microsecond.^[38] The direct simulation of protein folding is usually too demanding.^[39–41] However, MD simulations are gradually acquiring the capacity to unravel the folding mechanism of peptides and



Shaul Mukamel, the Chancellor Professor of Chemistry at the University of California, Irvine, is the author of over 600 publications and the textbook *Principles of Nonlinear Optical Spectroscopy*. He works on designing novel laser pulse sequences to study molecular structure, fluctuations, and energy and charge transfer processes.

small proteins, thanks to the design of simple model peptides that mimic protein complexity, yet are sufficiently small to allow detailed simulations^[33,40,42–44] and the development and implementation of powerful simulation algorithms^[45] with improved sampling of rare events.^[46,47] Since the visualization of folding processes strongly depends on simulations, it is highly desirable to perform experiments on time scales accessible to computer simulations. 2DIR and atomistic level MD simulations can be carried out on the same timescale. Thus developing MD methods for simulating 2DIR signals can help assign 2DIR features, and unravel the underlying motions. At the same time the quality of different MD force fields can be tested by comparing the predicted 2DIR signatures of different folding pathways with experiment.

The state-of-the-art computational techniques currently employed in the modeling of 2DIR signals of biomolecules will be surveyed in this Review.^[48–55] The amide vibrations of peptides,^[55–57] can be described by the Frenkel exciton model originally developed to describe coupled localized transitions of oligomers or polymers made out of similar repeat units. The necessary parameters can be obtained from electronic-structure calculations of individual chromophores, rather than the whole system, greatly reducing the computational demands. The spectrum consists of well-separated bands of energy levels representing single excitations, double excitations, and higher excitations. The molecular Hamiltonian conserves the number of excitations; they can only be changed by the optical fields. The lowest (single-exciton) manifold is accessible by linear optical techniques, such as absorption spectroscopy and circular dichroism (CD), whereas the doubly excited (two-exciton) and higher manifolds only show up in nonlinear spectroscopic techniques. A high-level fluctuating excitonic Hamiltonian for polypeptides is presented in Section 3. In Section 4 introduces the response function approach for simulating the signals. The modeling of the coherent vibrational response involves the following key steps:

1. Protein and solvent configurations are generated by an MD trajectory using existing molecular mechanics force fields such as CHARMM,^[58] GROMOS,^[59] and AMBER.^[60]
2. A fluctuating effective anharmonic vibrational–exciton Hamiltonian, $\hat{H}_S(t)$, and the transition dipole matrix $\mu(t)$ for the relevant states, is constructed for each configuration. This must be a higher-level Hamiltonian, than the molecular mechanics force fields used in step (1) to model the structure.
3. Four-point correlation functions of transition dipoles are calculated which describe the relevant motions and fluctuations.^[61]
4. The response functions are calculated by specific combinations of the four-point correlation functions which represent the quantum Liouville-space pathways relevant for the chosen technique.^[66]

Step 1 is well developed and documented and can use the broad arsenal of available algorithms and software packages. We shall therefore focus on steps 2–4. Section 2 presents a

brief survey of the history of coherent multidimensional spectroscopy. In Section 3 we review the methods for constructing the fluctuating excitonic Hamiltonian for the peptide amide bands. The theoretical framework for modeling the nonlinear optical signal is introduced in Section 4, where we further introduce a simple exactly solvable Gaussian fluctuation model. In this sum-over-state (SOS) approach^[62] the optical fields induce transitions between system eigenstates, and the nonlinear response is attributed to the anharmonicity of the system (note that harmonic vibrations are linear, their nonlinear response vanishes by interference between quantum pathways). The SOS method is practical for small peptides (as an example, the amide-I bands of a peptide with less than 30 residues). The stochastic Liouville equations approach for describing chemical exchange and spectral diffusion by incorporating external collective bath coordinates is introduced in Section 5. Applications to the hydrogen bonding fluctuation dynamics in water as observed in the OH stretch of HOD in D₂O are given in Section 6. A different method^[48,62,63] more suitable for large biomolecules such as globular proteins or membrane systems is described in Section 7. In this approach the signal is connected to the scattering of single excitations (quasiparticles) rather than transitions between states. The quasiparticle expressions which scale more favorably with size can be derived by using equations of motion, the nonlinear exciton equations (NEE).^[64] In Section 8 we demonstrate how a specific choice of the signal wavevector can reveal double excitations (double quantum coherence) which provide a different window for structure. Chirality-induced signals, 2D analogues of circular dichroism, aimed at improving the resolution of 2DIR signals by exploiting the chirality of peptides, are presented in Section 9. Amyloid fibrils are aggregates formed by misfolded peptides associated with several human diseases, such as Alzheimer disease. Their toxicities strongly depend on their structures. 2DIR simulations described in Section 10 show great promise for retrieving structural information, not available by any other techniques. A summary and future outlook of multidimensional techniques are presented in Section 11.

2. History of Multidimensional Vibrational Spectroscopy

IR absorption, provides a one dimensional (1D) projection of molecular information onto a single frequency axis, through the linear polarization induced in the sample in the field. Higher-order polarizations, and more complex molecular events, can be revealed by nonlinear spectroscopic techniques. Incoherent techniques,^[65,66] such as fluorescence, spontaneous Raman and pump–probe, do not depend on the phases of the laser pulses. Coherent techniques, in contrast, do generally depend on the phase. The modeling of nonlinear spectra is simplified considerably when the relaxation rates of frequency fluctuations (Λ) are either very fast or very slow compared to their magnitude (Δ). They can then be incorporated phenomenologically as homogeneous ($\Delta/\Lambda \ll 1$) or inhomogeneous ($\Delta/\Lambda \gg 1$) broadening, respectively. Picosec-

ond, electronically off-resonant, coherent anti-Stokes Raman spectroscopy (CARS) measurements of vibrational dephasing performed in the 1970s were believed to have the capacity to distinguish between the two broadening mechanisms,^[67,68] similar to the photon-echo technique.^[69] By formulating the problem in terms of multipoint correlation functions of the electric polarizability, Loring and Mukamel^[70] have shown that this is not the case. The key lesson was that optical signals should be classified by their dimensionality, that is, the number of externally controlled time intervals rather than by the nonlinear order in the field. Both photon-echo and electronically off-resonant time resolved CARS signals are third order in the external fields. However, the off-resonant CARS only has one control time variable t_2 (see Figure 1). The other two times t_1 and t_3 are very short, as dictated by the Heisenberg uncertainty relation for an off-resonant transition and carry no molecular information. The technique is thus one-dimensional, (1D) carries identical information to the spontaneous Raman and can not in principle distinguish between homogeneous and inhomogeneous line shapes. Based on this analysis, a 2D Raman analogue of the photon echo will require seven rather than three pulses. Such experiments have been carried out.^[71–73] Closed expressions derived for the multipoint correlation functions of a multi-level system whose frequencies undergo stochastic Gaussian fluctuations^[74,75] paved the way for the multidimensional simulations of such spectra.^[76] Tanimura and Mukamel^[77] subsequently proposed a simpler, five-pulse, impulsive off-resonant Raman technique and showed how it can be interpreted using 2D frequency–frequency correlation plots, in analogy with multidimensional NMR spectroscopy. Experiments performed on low-frequency (ca. 300 cm^{−1}) intermolecular vibrations in liquid CS₂^[78–87] were initially complicated by cascading effects (sequences of third-order processes). These were eventually resolved.^[88] Applications to liquid formamide were reported as well.^[89] The same idea was then proposed^[48,65,90] and carried out for vibrational transitions in the IR^[57,91–93] and for electronic spectroscopy in the visible region.^[94–97] IR techniques require fewer pulses than Raman, since each transition involves a single field, rather than two. The necessary control of the phase of some or all laser pulses, which is straightforward for radiowaves (NMR) is considerably more challenging for higher frequencies.

The first frequency–frequency 2D IR measurement was carried out by Hamm and Hochstrasser,^[98] who employed a pump–probe technique with two IR pulses with a narrow (ca. 10 cm^{−1}) pump and a broad (130 cm^{−1}) probe pulse. The signal field was dispersed in a spectrometer and recorded against the pump and the dispersed signal frequencies. This study demonstrated how the cross-peaks can be used to investigate the structures of small peptides.^[99] The diagonal peaks reveal the energies of the localized carbonyl C=O vibrational mode, while the cross-peaks are directly related to the couplings between the modes which depend on the peptide structure. The cross-peak intensities and anisotropies of a cyclic rigid penta-peptide were connected to the 3D structure with the help of a simple model for the coupling.

A quantitative analysis requires higher level model Hamiltonian operators, which were developed for small

peptides. The central backbone structure of trialanine in aqueous solution was investigated, using polarization sensitive two-dimensional (2D) vibrational spectroscopy on the amide I mode.^[100] The stimulated IR photon echo of *N*-methylacetamide (NMA),^[101] a molecular mimic of a single amide unit, was then measured and used to determine the vibrational frequency correlation function. These results are often used as a benchmark for effective Hamiltonian operators. Experiments performed on polypeptides are widely used for benchmarking the couplings and transition dipoles. 2DIR spectra of a series of doubly isotopically substituted 25-residue α -helices were reported in 2004. ¹³C and ¹⁸O labeling of at known residues on the helix permitted the vibrational couplings between different amide I modes separated by one, two, and three residues to be measured.^[102] Two similar studies of a beta hairpin,^[56] a 3₁₀ helix and another type of α -helical peptide^[103] were reported. Other small molecules including DNA^[104] and a rotaxane (molecular ratchet)^[105] have been studied.

The successful applications of 2DIR to small peptides triggered the investigation of larger systems. Tokmakoff et al. identified a characteristic “Z” shape photon-echo spectrum of the β -sheet motif proteins by comparing several globular proteins with increasing β -sheet content.^[57] α -Helices showed a flattered “figure-8” line shape, and random coils gave rise to unstructured diagonally elongated bands.^[106] Righini and co-workers studied the local structure of lipid molecules in dimyristoylphosphatidylcholine (DMPC) membranes using isotopic labeling of the carbonyl moieties in the membranes.^[107,108] In a 2D line shapes study of the amide-I bands (backbone carbonyl stretch) for 11 residues along the length of a transmembrane peptide bundle, Zanni et al. measured the homogeneous and inhomogeneous widths of vibrational modes that reflect the structural distributions and picosecond dynamics of the peptides and their environment.^[93] 2DIR studies of misfolded peptide aggregates (amyloid fibrils) were reported.^[109–111]

Time-resolved measurements can monitor the pico- to nanosecond dynamics by following the variation of the cross-peaks with time,^[112] Hamm and co-workers had monitored the unfolding of a tetra-peptide triggered by breaking the disulfide bridge between the first and the third residues by a UV pulse.^[22,92] The cross-peaks reveal the hydrogen-bonding dynamics on a timescale of a few picoseconds. Based on 2DIR of the amide I vibrations, Tokmakoff reported the steady-state and transient conformational changes in the thermal unfolding of ubiquitin.^[113] Equilibrium measurements are consistent with a simple two-state unfolding. However, the transient experiments show a complex relaxation pattern that varies with the spectral component and spans six order of magnitudes in time. Using time-resolved IR spectroscopy, Hamm et al. could report strongly temperature-dependent non-exponential spectral kinetics of the folding and unfolding of a photoswitchable 16-residue alanine-based α -helical peptide from a few picoseconds to almost 40 μ s over the temperature range 279–318 K.^[114] Both processes show a complex stretched-exponential response, indicating a broad distribution of rates. Environment effects on the vibrational dynamics of tungsten hexacarbonyl in cryogenic matrices

were investigated using an infrared-free electron laser by measuring the population relaxation time T_1 in pump–probe and the dephasing time T_2 in a two-pulse photon echo.^[115] Fast (less than a few ps) enzyme dynamics at the active site of formate dehydrogenase (FDH) in complex with azide (N_3^- , a nanomolar inhibitor, and a transition state analogue) and nicotinamide (NAD^+) were detected by IR photon-echo measurements. These studies show that the active site of the reactive enzyme complex near the catalytic transition state exhibits the fast dynamics required to explain the kinetics of several enzymes.^[116] Harris and co-authors showed that 2DIR spectroscopy can provide direct information about the transition-state geometry, time scale, and reaction mechanisms by tracking the transformation of vibrational modes as $[Fe(CO)_5]$ crossed a transition state of the fluxional rearrangement.^[117]

Ultrafast IR–Raman spectroscopy (mid-IR pump and Raman probe pulse) were applied to study fast energy-transfer dynamics in liquid water, HOD in D_2O , and methanol.^[118,119] The hydrogen-bonding structure and dynamics in liquid water have been extensively studied by 2DIR. Tokmakoff and co-workers investigated rearrangements of the hydrogen-bond network by measuring fluctuations in the OH-stretching frequency of HOD in liquid D_2O . The frequency fluctuations were related to intermolecular dynamics. The model reveals that OH frequency shifts arise from changes in the electric field acting on the proton. At short times, vibrational dephasing reflects an under-damped oscillation of the hydrogen bond with a period of 170 femtoseconds. At longer times, vibrational correlations decay on a 1.2 picosecond timescale as a result of collective structural reorganizations.^[120] A combined femtosecond 2DIR and molecular dynamics simulations study focused on the stability of non-hydrogen bonded species in an isotopically dilute mixture of HOD in D_2O . Hydrogen-bonded configurations and non-hydrogen-bonded configurations were shown to undergo qualitatively different relaxation dynamics.^[121] Molecular dynamics electronic-structure calculations were used to obtain the time-correlation functions (TCF) for two water force fields, TIP4P and SPC/E.^[122] The TCFs serve as inputs to simulations of 2DIR spectra. Comparison with experiment demonstrates that both force fields overemphasize the fast (300–400 fs) fluctuations and do not account for the slowest fluctuations (1.8 ps). The vibrational echo correlation spectra provide a good test for the TCF. Temperature dependence of the OH stretch photon-echo signal of liquid H_2O showed that the frequency (thus structural) correlations decrease from 50 fs to 200 fs as temperature decreases from 297 to 274 K, which suggests a reduction in dephasing by librational excitations.^[123] Simple anions (CN^- , N_3^-) have been used as probes of the fluctuations of water hydrogen-bonding networks.^[124–126]

Electrostatic interactions are crucial for enzyme activity and drug design. For example, the noncovalent electrostatic couplings of cofactors are sufficiently weak to allow for reversible binding.^[127,128] 2DIR should provide a direct means for monitoring the electrostatic environment and its fluctuations. Artificial chromophores, such as nitriles, could be inserted in specific sites in the active region.^[129] A 2DIR study

of an HIV drug molecule containing two nitrile groups^[130] complexing to the reverse transcriptase of HIV-1 shows spectral splitting attributed to the binding environment. Several bond types, including nitriles, carbonyls, carbon–fluorine, carbon–deuterium, azide, and nitro bonds were used as probes for electric fields in proteins using vibrational Stark spectroscopy. The measured Stark shifts, peak positions, and absorption cross sections may be used to design amino acid analogues or labels to act as probes of local environments in proteins.^[131] 2D techniques^[118,133] can monitor vibrational energy transfer pathways.^[132] Vibrational energy relaxation rates were simulated by employing the semiclassical approximation of quantum mechanical force–force correlation functions.^[134]

2D techniques may also be used to study reaction rates, mechanisms, and yields. Small peptides at thermal equilibrium in solution rapidly (within 10–100 ps) swap among different configurations. The dynamics of these transient species can influence the folding. Hochstrasser and Kim^[135] and Fayer et al.^[136] independently carried out a 2DIR analogue of chemical exchange for the investigation of ultrafast hydrogen-bonding dynamics of solute–solvent complexes. Hamm et al. employed non-equilibrium 2DIR exchange spectroscopy to map light-triggered protein ligand migration.^[137] Bond connectivity in molecules has been measured based on relaxation-assisted 2DIR signals, for this two parameters are decisive, a characteristic intermode energy transport arrival time and a cross-peak amplification coefficient. 2DIR spectra of the coupled carbonyl stretching vibrations of $[Rh(CO)_2(C_3H_7O_2)]$ in hexane detected with spectral interferometry characterizes the structure with a 20 ps time window.^[138]

3. Hamiltonian Operators for the Amide Vibrations of Polypeptides

Vibrational spectra are commonly described by normal modes, which represent the collective motions of the atoms when all anharmonicities are neglected. The normal-mode frequencies and individual atom displacements may be calculated from molecular-mechanics force fields implemented in standard MD codes. These are parameterized to represent slow backbone motions. High-frequency vibrations such as the amide bands of peptides require more accurate ab initio calculations.

A peptide can be viewed as a chain of beads connected by amide bonds ($O=C-N-H$; Figure 3). These have a partial double-bond character and because of steric effects are almost exclusively in the *trans* configuration. The area between two consecutive α -carbon atoms (peptide unit) is thus rigid and planar. The peptide backbone structure is described by two dihedral Ramachandran angles ϕ and ψ per amide bond. The IR spectrum of the backbone peptide bonds consists of four amide vibrational bands, known as the amide I, II, III and A.^[139–41] These amide bands originate from the coupled localized amide vibrations on each peptide unit (local amide modes (LAMs)). The localization may be viewed by expanding the molecular charge density $\rho(\mathbf{r})$ in

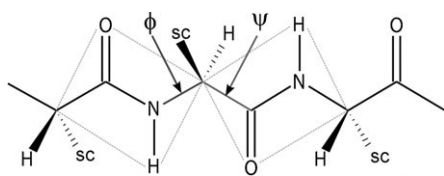


Figure 3. The amide bonds and Ramachandran angles (ϕ and ψ). The planes marked by gray lines are peptide units. "sc" represents side chains.

nuclear displacements [Eq. (1)] where q_{mi} is the i 'th vibrational mode of the m 'th peptide bond.

$$\rho(\mathbf{r}) = \rho^{(0)}(\mathbf{r}) + \sum_{mi} \left(\frac{\partial \rho(\mathbf{r})}{\partial q_{mi}} \right) q_{mi} + \dots \quad (1)$$

The transition charge density (TCD) $\partial \rho / \partial q_{mi}$ ^[142] represents the electronic structure change induced by the q_{mi} vibration. The 0.01 esu/Bohr (TCD) contours of the for amide vibration bands of N-methyl acetamide (NMA), a model system of the amide bond, are shown in Figure 4. The

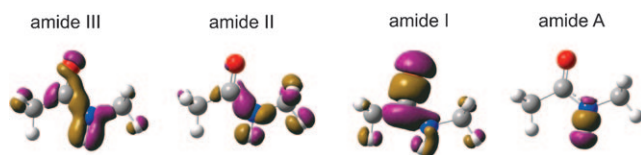


Figure 4. Transition charge densities (TCD) for the four amide modes of N-methylacetamide (NMA). The 0.01 esu/Bohr contour is shown. Violet and brown contours represent positive and negative values, respectively.

amide III (ca. 1200 cm^{-1}), II (ca. 1500 cm^{-1}) modes are attributed to bending motion of the N–H coupled to the C–N stretching. The 1600–1700 cm^{-1} amide I mode originates from the stretching motion of the C=O stretch coupled to in-phase N–H bending and C–H stretching. The amide A (ca. 3500 cm^{-1}) is almost purely the N–H bond stretch.^[139,140,143] All the TCDs are highly localized on the four atoms (O, C, N, and H) forming the amide bond. The overlap of the amide excitations between different amide bonds is small and is limited to nearest-neighbor peptide bonds. By parameterizing the Hamiltonian and transition dipole elements of all the amide bands (I, II, III and A) by the Ramachandran angles, repeated electronic structure normal mode calculations can be avoided for various conformations.

The sensitivity of the amide vibrational transitions to the local structure and the hydrogen-bonding environment makes them ideal candidates for distinguishing between various secondary structural motifs and monitoring effects of the changing environments.^[144] The intense and spectrally isolated amid-I band is particularly suitable for structure determination. Its frequency variation with the secondary structure and conformation is widely used as a marker in polypeptide- and protein-structure determina-

tion.^[56,57,105,143–146] α -Helical peptides have amide-I bands between 1650–1655 cm^{-1} . β -Sheets usually have a strong band between 1612–1640 cm^{-1} and a weaker band at approximately 1685 cm^{-1} . Random structures generally have a 1645 cm^{-1} band, which is close to the frequencies associated with α -helix. The antiparallel β -sheet structure shows a strong amide-II band between 1510 and 1530 cm^{-1} , whereas a parallel β -sheet structure has higher frequency bands (1530–1550 cm^{-1}). Deuterium substitution results in a substantial shift to lower frequency (to ca. 1460 cm^{-1}). The amide III IR band is typically weaker than the amide I and II. Deuteration also shifts the amide-III band to lower frequencies (960–1000 cm^{-1}). This band is usually not correlated with protein secondary structure, but is sensitive to hydrogen bonding and local Ramachandran angles.^[19] The amide-III band is sometimes used in combination with the amide-I band to distinguish the β -sheet and disordered structure which is not generally possible with only the amide-I band. The overlap of the amide A with the intense O–H band of water complicates its observation and interpretations.

A vibrational Hamiltonian operator adequate for 2DIR simulations of peptides has been constructed by expanding the potential to the 6th order in LAMs within each peptide unit, to the 4th order for neighboring couplings, and to the 2nd order for non-neighboring electrostatic couplings [Equation (3) of ref. [148] and Eq. (2)].^[142] Interactions between LAMs with non-overlapping TCD are purely electrostatic and are given by Equation (2).

$$\sum_{m,n} \sum_{i,j} \int_m d\mathbf{r} \int_n d\mathbf{r}' \frac{\partial \rho(\mathbf{r})}{\partial q_{mi}} \frac{\partial \rho(\mathbf{r}')}{\partial q_{nj}} q_{mi} q_{nj} \quad (2)$$

By diagonalizing the local Hamiltonian for each amide bond, 14 local amide eigenstates (four fundamentals, four overtones, and six combinations) are obtained in the energy range 0–7000 cm^{-1} for a single peptide unit, which will be denoted as local amide states (LAS). We define the exciton creation and annihilation operators for a 'th LAS on the m 'th unit $\hat{B}_{ma} \equiv |ma\rangle\langle m0|$ and $\hat{B}_{ma}^\dagger \equiv |m0\rangle\langle ma|$ where $|m0\rangle$ is the ground state. These satisfy the Pauli commutation relations: $[\hat{B}_{ma}, \hat{B}_{nb}^\dagger] = \delta_{n,n} \delta_{a,b} (1 - \sum_c \hat{B}_{mc}^\dagger \hat{B}_{mc}) - \delta_{m,n} \hat{B}_{mb}^\dagger \hat{B}_{ma}$.

The peptide Hamiltonian is then recast in terms of these operators [Eq. (3)].^[148]

The first term represents the local Hamiltonian. The couplings between neighboring peptide units (the second term) were computed as a function of the Ramachandran

$$\begin{aligned} \hat{H} = & \sum_m \sum_a \omega_{ma} \hat{B}_{ma} \hat{B}_{ma}^\dagger \\ & + \sum_{m,n} \left\{ \sum_{a,b} J_{mn,ab}(\phi, \psi) \hat{B}_{ma} \hat{B}_{nb}^\dagger + \sum_{a,b} K_{mn,ab}(\phi, \psi) \hat{B}_{ma} \hat{B}_{nb} \hat{B}_{ma}^\dagger \hat{B}_{nb}^\dagger \right\} \\ & + \sum_{m,n} \left\{ \sum_{a,b} K'_{mn,ab} \left(\hat{B}_{ma}^\dagger \hat{B}_{nb} + \hat{B}_{ma} \hat{B}_{nb}^\dagger + \hat{B}_{ma} \hat{B}_{nb} + \hat{B}_{ma}^\dagger \hat{B}_{nb}^\dagger \right) \right. \\ & \left. + \sum_{a,b,c} K''_{mn,abc} \left(\hat{B}_{na}^\dagger \hat{B}_{nb} \hat{B}_{mc} + \hat{B}_{na}^\dagger \hat{B}_{nb}^\dagger \hat{B}_{mc}^\dagger \right) + \sum_{a,b,c,d} K'''_{mn,abcd} \hat{B}_{ma}^\dagger \hat{B}_{mb} \hat{B}_{nc}^\dagger \hat{B}_{nd} \right\} \end{aligned} \quad (3)$$

angles (ϕ and ψ) at the BPW91/6-31G(d,p) level of DFT using a 4th order anharmonic vibrational potential of various glycine dipeptide (GLDP) configurations. An electrostatic model is used for couplings between non-neighboring units (the last two terms). The transition charge density couplings (TCDC) was expanded in terms of multipoles to the 4th rank. This treatment results in terms for dipole–dipole (ca. R^{-3}), dipole–quadrupole (ca. R^{-4}), and quadrupole–quadrupole and dipole–octupole (ca. R^{-5}) interactions where R is the distance between units.

Torii and Tasumi (TT) constructed such a map^[146] for the amide I neighboring coupling using restricted Hartree–Fock (RHF) electronic structure calculations of glycine dipeptide (GLDP). The amide I through-space coupling between the non-neighboring peptide units was approximated by the transition dipole coupling model (TDC).^[149,150] The magnitude, direction, and location of the transition moment were fitted to reproduce the ab initio coupling constants between the second nearest amide units (the magnitude of the transition dipole was $(\partial\mu/\partial q) = 2.73 \text{ DA}^{-1}$ with 10.0° angle to the C=O bond). Gorbunov, Kosov, and Stock^[151] derived a similar potential map at higher levels (MP2 and B3LYP). Woutersen and Hamm approximated through-space TCDC with Mulliken partial charges of a DFT calculation to include higher multipole contributions for the amide I vibration of methylacetamide (NMA),^[152] which was later improved by using multipole-derived charges.^[153] The accuracy of the amide I local frequencies and IR intensities with respect to reference DFT calculations was improved (0.1 cm^{-1} in frequency and 0.02 in IR intensity correlation) by including higher multipoles (see Table V of Ref. [153]). Transition multipole couplings extend the transition dipole couplings to include higher multipoles of all the amide modes. The higher multipole contributions are more important for amide-II, -III, and -A modes than I since the amide II and III are more delocalized over the peptide bond, and the amide A has a smaller transition dipole (see Figure 8 of Ref. [142]).

The dipole coupling with the radiation field is given by [Eq. (4)].

$$H_{\text{int}} = \sum_m \sum_a (\mu_{ma} B_{ma} + \mu_{ma}^* B_{ma}^\dagger) \quad (4)$$

To account for chirality this approach was extended to include magnetic moments. Derivatives of magnetic moments with respect to the LAM depend on the Ramachandran angles ψ and ϕ . A magnetic moment derivatives map was obtained by DFT calculations of a chiral model peptide unit which has a similar structure to NMA (see Figure 1 of Ref. [148]). These were calculated based on the atomic axial tensor and the normal modes.^[154]

3.1. Electrostatic Fluctuations of the Local Hamiltonian Operators

The local Hamiltonian operator [Eq. (3)] depends on the electrostatic environment induced by the surrounding peptide residues and the solvent. For example, the amide I frequen-

cies are shifted to the red by hydrogen bonding with water. Electrostatic modeling of the fluctuating local Hamiltonian requires repeated ab initio vibrational potential calculations of the peptide bonds surrounded by the partial charges of the surrounding peptide residues and the solvent. Simulation of 2DIR line shapes in NMA require the construction of a Hamiltonian along the MD trajectory for which there are typically around 10^5 snapshots. These repeated ab initio calculations can be avoided by an electrostatic parameterization of the Hamiltonian operator. Linear Stark modeling which uses the electric field at some reference point^[155] works for smaller chromophores.^[120,156,157] This model is not adequate for the amide vibrations of proteins where the non-uniform electric field across the peptide bond should be taken into account.^[142]

Ham and Cho (HC) obtained a map which parameterizes the amide I frequencies as a linear function of the electrostatic potentials at the C, O, N, and H and two methyl sites^[158,159] by a least-square fit of the normal mode frequencies of NMA–water clusters at the RHF level. Schmidt, Corcelli, and Skinner^[160] constructed a similar map (SCS) of the deuterated NMA (NMAD) amide I frequency, where the frequency was parameterized as a linear function of the electric fields at the C, O, N, and H atoms, and the electronic structure calculations were made at the DFT level. Watson and Hirst found that the accuracy of NMA amide I frequencies in water is improved by sampling the electrostatic potential at additional points in the amide bond (mid points of CO, CN, and NH).^[161]

We have parameterized the fundamental, the overtone, the combination frequencies, and transition dipoles of all the amide modes (III, II, I, and A) as a quadratic function of the multipole electric field up to the 2nd derivatives of the electric field at a midpoint of amide oxygen and hydrogen atoms (HM map).^[142] The map was constructed by eigenstate calculations of the 6th order anharmonic DFT (BPW91/6-31G(d,p)) vibrational potential in five relevant normal modes of NMA in the presence of different non-uniform multipole electric fields. The fundamental frequencies as well as anharmonicities are parameterized, and geometry changes and mode mixing induced by the multipole electric field are included. The average of and the correlations between the fundamental and anharmonicity frequency fluctuations determine the relative positions and intensities of two positive (stimulated emission/ground state bleach) and negative (excited state absorption) peaks of the nonlinear IR signals.^[162] Unlike the other map, this map does not involve a fitting to a specific solvent. A similar approach was later adopted for the amide I frequency by Jansen and Knoester^[163] who constructed the amide I single mode anharmonic vibrational potentials for NMA embedded in a set of different solvent charge distributions. The amide I frequencies were parameterized by the electric field and gradients at the C, O, N, and H atoms. The map does not include mode mixing. Frequencies and IR intensities of a pentapeptide in several gas-phase configurations^[161] calculated by this map combined with transition charge couplings and neighboring coupling map were in good agreement with DFT calculations,^[153] similar to the HC map.

The Torii and Tasumi couplings were used with our local Hamiltonian operator in earlier applications.^[164] The full Hamiltonian [Eq. (3)] was employed for two α helical peptides (SPE3^[145]) reported later in this Section.

The segment made of a given amide residue and two neighboring neutral groups of the CHARMM27 force field^[165] was used as the basic chromophores in the electrostatic interaction calculations (Figure 3). The effect of the rest of the protein and the solvent is described by a fluctuating electrostatic field. The electrostatic potential U is expanded to cubic order in local Cartesian coordinates X_α ($\alpha, \beta = x, y, z$) around the midpoint between amide oxygen and hydrogen atoms of the amide bond [Figure 5] and Eq. (5)].

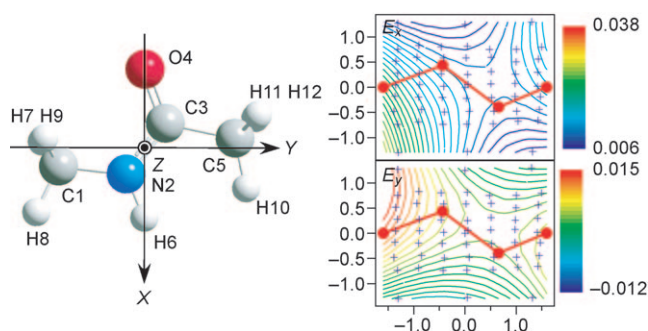


Figure 5. Left: NMA molecular structure and coordinate system used for the anharmonic force field and the electrostatic potential. The four amide atoms (O4, C3, N2, and H6) are in the x,y plane. The origin is the middle point of the oxygen (O4) and hydrogen (H6) atoms. Right: Contour plots of the non-uniform electric field (E_x and E_y) of NMA in H_2O . Red circles represent the four amide atoms (O4, C3, N2, and H6). The sampling points are shown by the blue crosses.

$$U(\mathbf{X}) = U_0 - \sum_{\alpha} E_{\alpha} X_{\alpha} - \frac{1}{2} \sum_{\alpha, \beta} E_{\alpha\beta} X_{\alpha} X_{\beta} - \frac{1}{6} \sum_{\alpha, \beta, \gamma} E_{\alpha\beta\gamma} X_{\alpha} X_{\beta} X_{\gamma} \quad (5)$$

Apart from the reference U_0 , Equation (5) has 19 independent parameters arranged in a vector $\mathbf{C} = (E_x, E_y, E_z, E_{xx}, E_{yy}, E_{zz}, E_{xy}, E_{xz}, E_{yz}, E_{xxx}, E_{yyy}, E_{zzz}, E_{xxy}, E_{xxz}, E_{xzz}, E_{yyz}, E_{yyy}, E_{xyy}, E_{xyx}, E_{xzy}, E_{xzz}, E_{yzz}, E_{yzy}, E_{yzz}, E_{zyx}, E_{zyx})$ (note the symmetry $E_{\alpha\beta} = E_{\beta\alpha}$).

The components of \mathbf{C} are determined at each time step by a least-square fit to the electric field which is sampled at 67 points in space spanning the TCD region of the four amide modes (Figure 5). We expect the electrostatic potential in the region of large TCD to affect the IR activity of that vibration. Four sampling points at C, O, N, and H atom positions were not sufficient to predict the solvent frequency shifts (especially for the amide-II and -III bands).^[142] This finding is consistent with the result of Watson and Hirst who found that increasing the number of sampling points improved the accuracy of the amide I frequency.^[161] The parametric dependence of the anharmonic force field on the electrostatic multipole coefficients \mathbf{C} was obtained for NMA^[142] at the BPW91/6-31G(d,p) level.^[166] This functional is known to give accurate amide vibrational normal mode frequencies $\omega_{ma}(\mathbf{0})$ of peptides.^[167] Analytic energy gradient in the presence of multi-

pole field was implemented in the Gaussian 03 code^[168] to compute the higher derivatives.^[169,170]

The LAS were calculated for a grid of electrostatic multipole coefficients \mathbf{C} by diagonalizing the local Hamiltonian operator expanded in a harmonic basis set. The ARNOLDI matrix diagonalization algorithm was employed in these vibrational configuration interactions (vibrational CI) calculations. The vibrational transition frequency from the ground state to LAS a and the transition dipole moments between LAS a and b at the m 'th peptide unit were expanded to quadratic order in \mathbf{C} [Eq. (6) and (7)]. The gas-phase frequencies were taken from experiment^[171] and $\mathbf{O}_a^{(1)}$ and $\mathbf{M}_{ab}^{(1)}$ are 19-component vectors representing the first derivative of the frequency and the transition dipole with respect to the \mathbf{C} . $\mathbf{O}_a^{(2)}$ and $\mathbf{M}_{ab}^{(2)}$ are the second derivative 19×19 matrices.

$$\omega_{ma} = \omega_{ma}(\mathbf{0}) + \mathbf{O}_a^{(1)\dagger} \mathbf{C}_m + \frac{1}{2} \mathbf{C}_m^{\dagger} \mathbf{O}_a^{(2)} \mathbf{C}_m \quad (6)$$

$$\mu_{mab}^{\alpha} = \mu_{mab}^{\alpha}(\mathbf{0}) + \mathbf{M}_{ab}^{\alpha(1)\dagger} \mathbf{C}_m + \frac{1}{2} \mathbf{C}_m^{\dagger} \mathbf{M}_{ab}^{\alpha(2)} \mathbf{C}_m \quad (\alpha = x, y, z) \quad (7)$$

To trace the origin of the electrostatic effects on the amide frequency shifts, the C=O and N–H bond lengths obtained by energy minimization for the various field values were parameterized in terms of \mathbf{C} .^[142] Strong correlations are seen in the scatter plots of the four amide fundamental frequencies with C=O and N–H bond length (Figure 6). These suggest that structural changes of NMA caused by the electric field^[142,146,155,172,173] are responsible for the frequency shifts. The positive correlations of the two bending frequencies with the N–H bond length are ascribed to the fact that the hydrogen bonding to H6 causes a longer N–H bond length

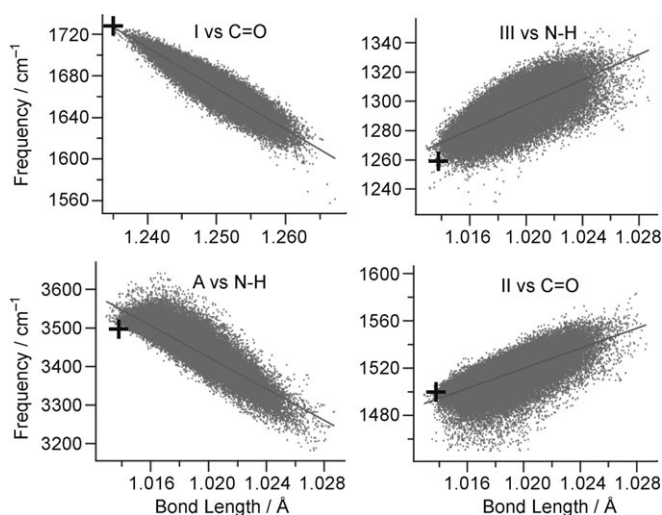


Figure 6. Scatter plots of amide frequencies versus bond lengths. Linear fits are $\omega = 6549.2 - 3905 R_{CO}$ (amide-I versus C=O bond length), $\omega = 24259 - 20426 R_{NH}$ (amide-A versus N–H bond length), $\omega = -3066 + 4278 R_{NH}$ (amide-III versus N–H bond length) and $\omega = 2768 + 4204 R_{NH}$ (amide-II versus N–H bond length). The gas-phase values are marked by crosses.

and stiffens the potential more along the amide II and III bending modes by stabilizing the parallel N2–H6···OH₂ structure.

The simulated amide I solvent peak shifts (-59 cm^{-1}) and line widths (29 cm^{-1}) of NMA in water are in good agreement with experiment (-80 cm^{-1} and 29 cm^{-1} respectively). This effective Hamiltonian operator was applied to SPE3, a 16-residue α -helical peptide (YGSPEAAA(KAAAA)₃r, r represent D-Arg).^[145] The fluctuating Hamiltonian operator was constructed for 100 snapshots obtained from a 2 ns MD trajectory.^[164] The vibrational eigenstates were calculated by diagonalizing the HM Hamiltonian operator. A good measure of the coherence length L_ν of the ν 'th vibrational eigenstate is provided by the participation ratio [Eq. (8)]^[54,65,174] where $C_{\nu,ma}$ is the expansion coefficient of the ν 'th eigenvector on LAS a at the n 'th peptide unit.

$$L_\nu = \left(\sum_m \left(\sum_a C_{\nu,ma}^2 \right)^2 \right)^{-1} \quad (8)$$

The distributions of L_ν over the frequencies of the eigenstates in four amide fundamental regions are shown in Figure 7. In the amide I region, the lower frequency eigen-

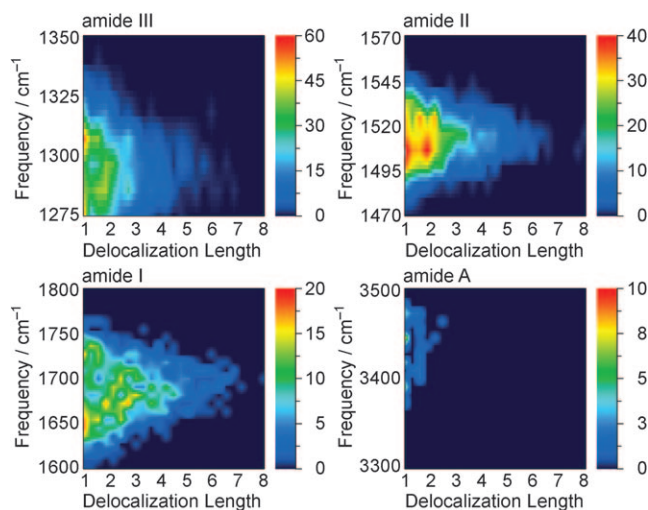


Figure 7. Distribution of the participation ratio (PR) versus frequency in the amide-III, -II, -I, and -A regions. Average PRs are 1.6 (amide III), 2.3 (amide II), 1.8 (amide I), and 1.0 (amide A).

states (ca. 1600 cm^{-1}) are mostly localized on one amide bond ($\langle L_\nu \rangle \approx 1$), the higher frequency eigenstates are delocalized. The higher frequency amide III eigenstates (ca. 1300 cm^{-1}) are localized. In the amide II region, there are two or three peaks in participation ratio distribution. The amide II fundamentals are the most delocalized with $\langle L_\nu \rangle = 2.3$, owing to the larger neighboring couplings and transition moments, and smaller diagonal frequency fluctuations. The amide-III and -I fundamentals are delocalized over 1.6 and 1.8 amide bonds. The amide A modes are highly localized ($\langle L_\nu \rangle = 1.0$) owing to the small transition moment and large frequency fluctuations.

This localization is good news for the interpretation of 2DIR signals in terms of local structure.

4. Liouville-Space Pathways for Coupled Localized Vibrations

Coherent optical signals can be classified according to their power-law dependence on the driving field intensities.^[66] The signals are related to the polarization, $P(t)$, induced by the external electric fields. The induced-polarization can be obtained perturbatively by expanding the density matrix $\rho(t)$ in powers of the external fields.^[66] The third-order response function, $R_{\nu_4\nu_3\nu_2\nu_1}^{(3)}(t_3, t_2, t_1)$ represents the lowest order contribution to the induced polarization in isotropic systems [Eq. (9)] where t_1, t_2, t_3 represent the interaction time intervals between successive interactions with the optical pulses, $E(\mathbf{r}, t; \nu_j)$ are the Cartesian components of the fields and polarizations. The response functions are system property tensors that contain all relevant molecular information. $R^{(1)}$ is a second-rank tensor connecting two vectors (\mathbf{E} and \mathbf{P}). Similarly, $R^{(3)}$ is a fourth-rank tensor.

$$P_{\nu_4}^{(3)}(\mathbf{r}, t) = \sum_{\nu_3\nu_2\nu_1} \int_0^\infty dt_3 \int_0^\infty dt_2 \int_0^\infty dt_1 R_{\nu_4\nu_3\nu_2\nu_1}^{(3)}(t_3, t_2, t_1) E_{\nu_3}(\mathbf{r}, t-t_3) E_{\nu_2}(\mathbf{r}, t-t_2-t_3) E_{\nu_1}(\mathbf{r}, t-t_1-t_2-t_1) \quad (9)$$

A heterodyne-detected four-wave mixing experiment (Figure 1)^[175] involves four pulses. In ideal impulsive measurements the pulses are temporally ordered, well separated, and much shorter than the relevant molecular timescales. Under these conditions, all integrations in Equation (9) can be eliminated and the optical signal is simply proportional to the response function itself. The third-order response is illustrated in Figure 8. The system is initially in thermal

$$R^{(3)}(t_3, t_2, t_1) = \left(\frac{i}{\hbar} \right)^3 \langle V | \mathcal{G}(t_3) \mathcal{V}_{\nu_4} \mathcal{G}(t_2) \mathcal{V}_{\nu_3} \mathcal{G}(t_1) \mathcal{V}_{\nu_1} \rangle$$

Figure 8. The schematic representation of third-order response function.

equilibrium, and the Green's function $\mathcal{G}(t_n)$ describes the free molecular time evolution (without the fields). At time 0 it interacts with the first pulse (\mathcal{V}_{ν_1}), propagates freely during t_1 ($\mathcal{G}(t_1)$), interacts with second pulse (\mathcal{V}_{ν_2}) at t_1 , propagates during time t_2 ($\mathcal{G}(t_2)$), interacts with third pulse (\mathcal{V}_{ν_3}) at $t_1 + t_2$, propagates during t_3 ($\mathcal{G}(t_3)$), and finally interacts with the signal mode (\mathcal{V}_{ν_4}) at $t_1 + t_2 + t_3$ to create the response. The dipole operator can act three times either on the ket or the bra vector.

The third-order response function is thus given by a sum of $2^3 = 8$ four-point correlation functions^[66] which constitute the eight basic Liouville space pathways [Eq. (10)].

$$R_{\nu_2\nu_3\nu_2\nu_1}^{(3)}(t_3, t_2, t_1) = \left(\frac{i}{\eta}\right)^3 \sum_{\alpha=1}^{\infty} R_{\alpha}(t_3, t_2, t_1) \quad (10)$$

Different techniques can select some of the possible terms in Figure 8, depending on the pulse configuration and the detection mode. To compute the signals, the electric field \mathbf{E} must be expanded in modes [Eq. (11)].

$$E_{\nu}(\mathbf{r}, t) = \sum_j [\mathcal{E}_{\nu_j}(t - \tau_j) \exp(i\mathbf{k}_j \cdot \mathbf{r} - i\omega_j(t - \tau_j) + i\phi_j) + \mathcal{E}_{\nu_j}^*(t - \tau_j) \exp(i\mathbf{k}_j \cdot \mathbf{r} + i\omega_j(t - \tau_j) - i\phi_j)] \quad (11)$$

The pulse $j = 1, 2, 3$ and s is centered at τ_j , with wavevector \mathbf{k}_j , carrier frequency ω_j , phase ϕ_j and complex envelope $\mathcal{E}_{\nu_j}(t - \tau_j)$. The three incoming pulses are labeled 1, 2, 3 and the signal as s . The \mathbf{k}_1 pulse comes first, followed sequentially by \mathbf{k}_2 , \mathbf{k}_3 , and \mathbf{k}_s . The heterodyne signal $S(t)$, defined as the change in the transmitted intensity of mode s induced by the other three beams (1–3), is related to $\mathbf{P}^{(3)}$, the third order polarization, and the external fields [Eq. (12)] where the \mathbf{r} is integrated over the interaction volume in the sample.

$$P_{k_s, \nu_s}^{(3)}(t) = \int d\mathbf{r} P_{\nu_s}^{(3)}(\mathbf{r}, t) \exp(-i\mathbf{k}_s \cdot \mathbf{r}) \quad (12)$$

Coherent nonlinear signals are highly directional and are only generated when \mathbf{k}_s lies along one of the *phase-matching* directions: $\mathbf{k}_s = \pm \mathbf{k}_3 \pm \mathbf{k}_2 \pm \mathbf{k}_1$ (with the corresponding frequencies $\omega_s = \pm \omega_3 \pm \omega_2 \pm \omega_1$). This important feature of coherent spectroscopy stems from the fact that we add the field *amplitudes* generated by different molecules, when the sample is much larger than the optical wavelength.^[297] Random phases then cancel the signals in other directions. Incoherent signals, such as fluorescence are obtained by adding the *intensities* (amplitude squares), and the signals are essentially isotropic. A whole host of names and acronyms have been used for various combinations of vectors and time intervals (e.g. photon echo, transient grating, CARS, HORSES, etc). NMR spectroscopy has its own set of acronyms. We shall avoid this nomenclature and simply classify the signals into four basic techniques: $\mathbf{k}_I = -\mathbf{k}_1 + \mathbf{k}_2 + \mathbf{k}_3$, $\mathbf{k}_{II} = \mathbf{k}_1 - \mathbf{k}_2 + \mathbf{k}_3$, $\mathbf{k}_{III} = \mathbf{k}_1 + \mathbf{k}_2 - \mathbf{k}_3$, and $\mathbf{k}_{IV} = \mathbf{k}_1 + \mathbf{k}_2 + \mathbf{k}_3$.

The dominant contributions to resonant signals only come from terms obtained when the field and molecular frequencies in Equation (9) have an opposite sign. Other (same-sign) highly oscillatory terms may be safely neglected. Using this rotating wave approximation (RWA), each phase-matching signal is described by a specific combination of Liouville-

$$P_{\mathbf{k}_I, \nu_I}(t) = \exp[-i\omega_I(t - \tau_3) - i(\omega_2 - \omega_1)(\tau_3 - \tau_2) + i\omega_1(\tau_2 - \tau_1)] \times \sum_{\nu_3, \nu_2, \nu_1} \int_0^\infty dt_3 \int_0^\infty dt_2 \int_0^\infty dt_1 R_{\mathbf{k}_I, \nu_I, \nu_3, \nu_2, \nu_1}^{(3)}(t_3, t_2, t_1) \mathcal{E}_{\nu_3}(t - t_3 - \tau_3) \mathcal{E}_{\nu_2}(t - t_3 - t_2 - \tau_2) \times \mathcal{E}_{\nu_1}^*(t - t_3 - t_2 - t_1 - \tau_1) \exp[i\omega_I t_3 + i(\omega_2 - \omega_1)t_2 - i\omega_1 t_1] \quad (13)$$

space pathways. As an example, for the \mathbf{k}_I technique we get Equation (13).

The dependence of $R_{\mathbf{k}_I, \nu_I, \nu_3, \nu_2, \nu_1}^{(3)}(t_3, t_2, t_1)$ on the wavevector comes by selecting the RWA pathways.

To invoke the RWA the molecular model must be specified. The amide band energy level scheme consists of three well-separated bands (Figure 9). Only transitions between the ground state, g , and the first excited states manifold, e , and between the first and second excited state manifold, f , are allowed. The response functions may be calculated by summing over all possible transitions among vibrational eigenstates. The nonlinear response vanishes for harmonic vibrations and may thus be attributed to the anharmonicities. The terms that contribute to the signal can be represented using Feynman diagrams which show the evolution of the density matrix. These are constructed using the following rules:

1. The density matrix is represented by two vertical-lines which represent the ket (left line) and the bra (right line) vectors.
2. Time runs vertically from bottom to top.
3. Each interaction with the radiation field is represented by a wavy line. An arrow pointing to the right and labeled \mathbf{k}_j represents a contribution of $\mathcal{E}_j \exp(-i\omega_j t + i\mathbf{k}_j \cdot \mathbf{r})$ to the polarization. An arrow pointing to the left represents a contribution of the term $\mathcal{E}_j^* \exp(i\omega_j t - i\mathbf{k}_j \cdot \mathbf{r})$ ($\omega_j > 0$).
4. Each diagram has an overall sign of $(-1)^n$ where n is the number of interactions from the right side (bra) (an interaction \hat{v} that acts from the right in a commutator in the Liouville equation carries a minus sign).

The Feynman diagrams for the \mathbf{k}_I technique depicted in Figure 10 show the state of the density matrix during each time interval. Computing the signals generally involves multiple integrations over the pulse envelopes [Eq. (9)].

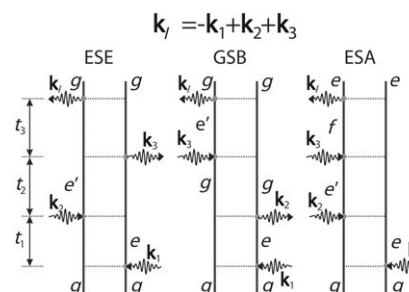


Figure 10. Double-sided Feynman diagrams representing the Liouville space pathways contributing to the \mathbf{k}_I signal in the rotating-wave approximation. The three pathways are known as excited-state emission (ESE), the ground-state bleaching (GSB), and excited-state absorption (ESA).

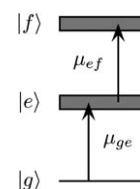


Figure 9. Energy-level scheme for the systems considered. g is the ground state, e is the first excited-state manifold, and f is the second excited-state manifold. The transitions that can be induced by the pulses are shown as μ_{ge} and μ_{ef} .

Clearly, the shape and relative phases of the pulses are important factors which affect the signal. Coherent control and pulse shaping algorithms may be used to design signals that meet desired targets.^[64] Herein we focus on ideal time-domain techniques where the pulses are well separated temporally. Multidimensional signals are displayed in the frequency domain by performing the multiple Fourier transform of $S_{\mathbf{k}}^{(3)}(t_3, t_2, t_1)$ with respect to the time intervals between

$$S_{\mathbf{k}_i}^{(3)}(\Omega_3, t_2, \Omega_1) = \int_0^\infty dt_3 \int_0^\infty dt_1 e^{i\Omega_3 t_3 + i\Omega_1 t_1} S_{\mathbf{k}_i}^{(3)}(t_3, t_2, t_1) \quad (14)$$

the pulses. We shall consider the signal given in Equation (14).

$$S_{\mathbf{k}_i, GSB}(\Omega_3, t_2, \Omega_1) = -\left(\frac{1}{\hbar}\right)^3 \sum_{e'e} \frac{(\mu_{ge'} \cdot \hat{\mathcal{E}}_s^*(\omega_s - \omega_{e'g}))(\mu_{e'g} \cdot \hat{\mathcal{E}}_3(\omega_{e'g} - \omega_2))(\mu_{eg} \cdot \hat{\mathcal{E}}_2(\omega_{eg} - \omega_2))(\mu_{ge} \cdot \hat{\mathcal{E}}_1^*(\omega_{ge} - \omega_1))}{(\Omega_3 - \xi_{e'g})(\Omega_1 - \xi_{ge})} \quad (15)$$

$$S_{\mathbf{k}_i, ESE}(\Omega_3, t_2, \Omega_1) = -\left(\frac{1}{\hbar}\right)^3 \sum_{e'e} \exp(-i\xi_{e'e} t_2) \times \frac{(\mu_{ge'} \cdot \hat{\mathcal{E}}_s^*(\omega_s - \omega_{e'g}))(\mu_{e'g} \cdot \hat{\mathcal{E}}_3(\omega_{e'g} - \omega_2))(\mu_{e'g} \cdot \hat{\mathcal{E}}_2(\omega_{e'g} - \omega_2))(\mu_{ge} \cdot \hat{\mathcal{E}}_1^*(\omega_{ge} - \omega_1))}{(\Omega_3 - \xi_{e'g})(\Omega_1 - \xi_{ge})} \quad (16)$$

$$S_{\mathbf{k}_i, ESA}(\Omega_3, t_2, \Omega_1) = -\left(\frac{1}{\hbar}\right)^3 \sum_{f'e} \exp(-i\xi_{f'e} t_2) \times \frac{(\mu_{gf} \cdot \hat{\mathcal{E}}_s^*(\omega_s - \omega_{fe}))(\mu_{fe} \cdot \hat{\mathcal{E}}_3(\omega_{fe} - \omega_3))(\mu_{e'g} \cdot \hat{\mathcal{E}}_2(\omega_{e'g} - \omega_2))(\mu_{ge} \cdot \hat{\mathcal{E}}_1^*(\omega_{ge} - \omega_1))}{(\Omega_3 - \xi_{fe})(\Omega_1 - \xi_{ge})} \quad (17)$$

This signal is given by ref. [176] in the form of Equations (15)–(17).

These expressions show how the pulse envelopes select the transitions lying within the pulse bandwidths. The terms e and e' run over the first excited state manifold and f includes the second excited states manifold (Figure 9). The terms ω_1 , ω_2 , and ω_3 are the carrier frequencies of the first three pulses. $\omega_{ab} = (\varepsilon_a - \varepsilon_b)/\hbar$ are the transition frequencies where the ε s are the state energies and $\xi_{ab} = \omega_{ab} - i\gamma_{ab}$ are complex transition frequencies which include the dephasing rates γ . In the impulsive (broad bandwidth) limit we simply set $\mathcal{E}(\omega) = 1$.

4.1. Simulating 2DIR Spectra of Small Peptides with Gaussian Frequency Fluctuations

We now turn to a special class of fluctuation models^[55,62] which may be solved exactly, yielding compact, closed expressions for the response functions. These have been applied for modeling 2DIR signals of small peptides with less than 30 residues.

We assume purely diagonal (energy) fluctuations that conform to Gaussian statistics. The fluctuations are small compared to energy-level spacings. This is the case when the

energies are modulated by collective coordinates expressed as sums of harmonic coordinates. However, the model holds more broadly, thanks to the central limit theorem, when the collective coordinates are given by sums of many bath coordinates, each making a small contribution. One notable example is the Marcus theory of electron transfer^[177] where the collective coordinate is the electric field at a given site, given by the sum of contributions from all surrounding charges in the solvent. Using the Condon approximation we can neglect fluctuations of the magnitude of the transition dipole.

The response functions can be calculated exactly using the second-order Cumulant expansion. To that end, we define $U_{ma}(t) \equiv \omega_{ma}(t) - \bar{\omega}_{ma}$ representing the fluctuations of the transition frequencies, where $\bar{\omega}_{ma}$ is the average transition

frequency. The two-time correlation function of U is given by Equation (18) where $C'(t)$ and $C''(t)$ are the real and imaginary parts of C and $\tau_{12} = \tau_1 - \tau_2$. We further define the line-broadening functions as Equation (19): Using the fluctuation-dissipation relation between C' and C'' , $g_{mn}(t)$ can be expressed as Equation (20) where the $C''_{nm}(\omega)$ known as the spectral density given by Equation (21). The real and the imaginary parts of $g_{mn}(t)$ are responsible for line-broadening and spectral shift, respectively. The third-order nonlinear response functions can be expressed in terms of $g(t)$.^[66] We denote this model as the Cumulant expansion of Gaussian fluctuations (CGF).

$$C_{mn}(\tau_1, \tau_2) = \frac{1}{\hbar^2} \langle U_{ma}(\tau_1) U_{na}(\tau_2) \rangle \equiv C'(\tau_{12}) + iC''(\tau_{12}) \quad (18)$$

$$g_{mn}(t) = \int_0^t d\tau_1 \int_0^{\tau_1} d\tau_2 C_{mn}(\tau_1) \quad (19)$$

$$g_{mn}(t) = \int_{-\infty}^{\infty} \frac{d\omega}{2\pi} \frac{1 - \cos(\omega t)}{\omega^2} \coth\left(\frac{\hbar\omega}{2k_B T}\right) C''_{mn}(\omega) + i \int_{-\infty}^{\infty} \frac{d\omega}{2\pi} \frac{\sin(\omega t) - \omega t}{\omega^2} C''_{mn}(\omega) \quad (20)$$

$$C''_{mn}(\omega) = 2 \int_0^\infty dt \sin(\omega t) C''_{mn}(t) \quad (21)$$

Simulated \mathbf{k}_I and \mathbf{k}_{III} signals of all the amide modes of *N*-methyl acetamide (NMA) in water in the cross-peaks regions are shown in Figure 11. The simulations reproduce the amide I and II anharmonicities obtained by the recent cross-peak experiment (calcd: 14 cm⁻¹ and 13 cm⁻¹; exp: 12 cm⁻¹ and 10 cm⁻¹, respectively).

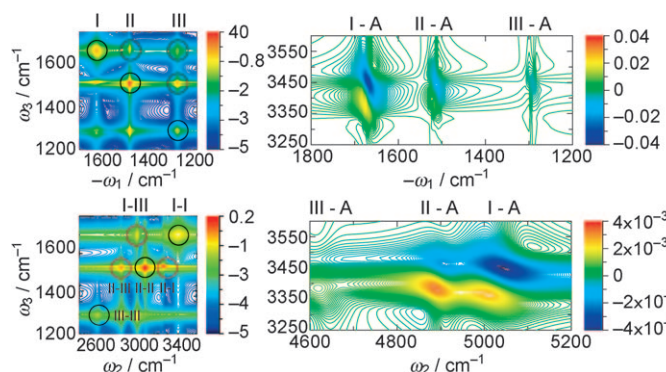


Figure 11. 2D signals of a model system for the peptide bond (NMA) in the cross-peak region of amide-I, -II, -III, and -A modes. Top panel, left: $\text{Im}[S_k(-\Omega_1, t_2=0, \Omega_3)]$ in the cross-peak region of amide-I, -II, and -III modes; bottom panel, left: $\text{Im}[S_k(t_1=0, \Omega_2, \Omega_3)]$ in the cross-peak region of amide I, II, and III modes. Right panels show the same signals in the cross-peak regions of the amide-A and amide-I, -II, and -III modes.

The frequency–frequency correlation function of two vibrational transitions [Eq. (18)] can be represented as Equation (22) where $\Delta_{mn} \equiv \sqrt{\langle U_{ma}^2 \rangle}$ is a fluctuation amplitude, \bar{C}_{mn} is a normalized correlation function ($\bar{C}_{mn}(0) = 1$), and $\eta_{mn} \equiv \langle U_{ma} U_{na} \rangle / \sqrt{\langle U_{ma}^2 \rangle \langle U_{na}^2 \rangle}$ is the correlation coefficient which varies between 1 (full correlation) through 0 (no correlation) to -1 (anti-correlation).

$$C_{mn}(t) = \eta_{mn} \Delta_{mn} \Delta_{nn} \bar{C}_{mn}(t) \quad (22)$$

To investigate the sensitivity of coherent IR signals to correlated frequency fluctuations, the amide I–III photon-echo cross-peak of NMA, $\text{Im}[S_k(\Omega_1, t_2=0, \Omega_3)]$ are shown in Figure 12 for various combinations of the correlations coefficients η_{mn} . Negative and positive peaks of the signal correspond to the ESA and ESE/GSB pathways of Figure 10 respectively. Correlations between the amide I and III (η_{13}) contribute to the negative components, and correlation between the amide III and the combination state I + III (η_{19}) contributes to the positive component. The negative peak becomes weaker and broader as η_{13} is varied from $+1$ to -1 , but does not depend significantly on η_{19} . The positive

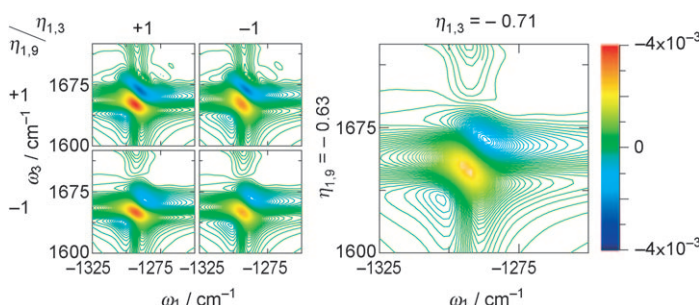


Figure 12. The amide-I–III k , cross-peak signals of NMA for different correlation coefficients. Left panels: $\text{Im}[S_k(\Omega_1, t_2=0, \Omega_3)]$ signal for different η_{13} and η_{19} ; right panels: the actual simulated signals.

peak becomes smaller and broader elongated more in Ω_3 direction as η_{19} goes from full correlation ($+1$) to anti-correlation (-1). The actual simulated values (anti-correlated $\eta_{13} = -0.71$ and correlated $\eta_{19} = 0.63$) gives weaker signals than in the fully correlated case.

For systems with several local minima whose dynamics can be divided into well-separated time regimes, the inhomogeneous CGF method can be adopted.^[76] The spectrum is obtained by summing over contributions of the slowly interconverting configurations, each represented by the CGF. This method is illustrated for the simulation of the amide I region of a specific tryptophan zipper peptide, trpzip2 in a β -hairpin conformation and its ^{13}C isotopomers. β -Hairpins are common protein structural elements which provide an important model system for the folding kinetics of larger proteins. Their structure and folding dynamics have been studied extensively. One structural motif, the tryptophan zipper (trpzip), greatly stabilizes the β -hairpin conformation in short peptides (12 or 16 Å in length). Trpzips are the smallest peptides to adopt a unique tertiary fold without requiring metal binding, unusual amino acids, or disulfide crosslinks. 500 snapshots with 2 ps time intervals were selected from the 1 ns trajectory and used for the inhomogeneous averaging. A 5.5 cm^{-1} homogeneous dephasing rate^[178] γ was added. Two electrostatic maps (HC^[158] and HM^[142] as described in Section 3) were used to compute the local mode frequencies in solution. Spectra of unlabeled samples (UL) and those with ^{13}C isotope labeling at specific residues are calculated. The sample with a β strand residue (the second residue) labeled is denoted L2, while the sample with a turn residue (the seventh) labeled is denoted L7. The simulated signals are compared with experiment in Figure 13 and Figure 14.

The experimental absorption spectra of trpzip2 ^{13}C isotopomers in the amide-I region are displayed in Figure 13. They show two main transitions: the stronger low frequency transition, around 1640 cm^{-1} , is due to inter-chain in-phase C=O motions and intra-chain out-of-phase C=O motions, whereas the weaker high-frequency transition, around 1675 cm^{-1} , is mainly due to the inter-chain out-of-phase C=O motions and intra-chain in-phase C=O motions. The two isotopomers show different ^{13}C effects: the ^{13}C band is shifted 10 cm^{-1} to the red in L7 than in L2 (1590 vs. 1600 cm^{-1}). Simulated spectra are shown in Figure 13 panel B (HC Hamiltonian operator) and Figure 13 panel C (HM Hamiltonian operator). The high-frequency component is slightly stronger for the HM, but overall both models reproduce the main spectral feature of the unlabeled β -hairpin. In addition, both predict a small difference in the observed ^{13}C -shifts between L2 and L7. The difference is slightly larger in the HM simulation.

The top row in Figure 14 shows the experimental $k_I + k_{II}$ spectra of the trpzip2 ^{13}C isotopomers. In Figure 14 panel A, the diagonal signals are due to 0-1 (red) and 1-2 transitions (blue). The two fundamental 0-1 frequencies agree with the experimental absorption, as can be seen by projecting the 2D spectrum onto the Ω -axis. The cross-peaks are induced by pairwise vibrational couplings among local amide-I modes. The

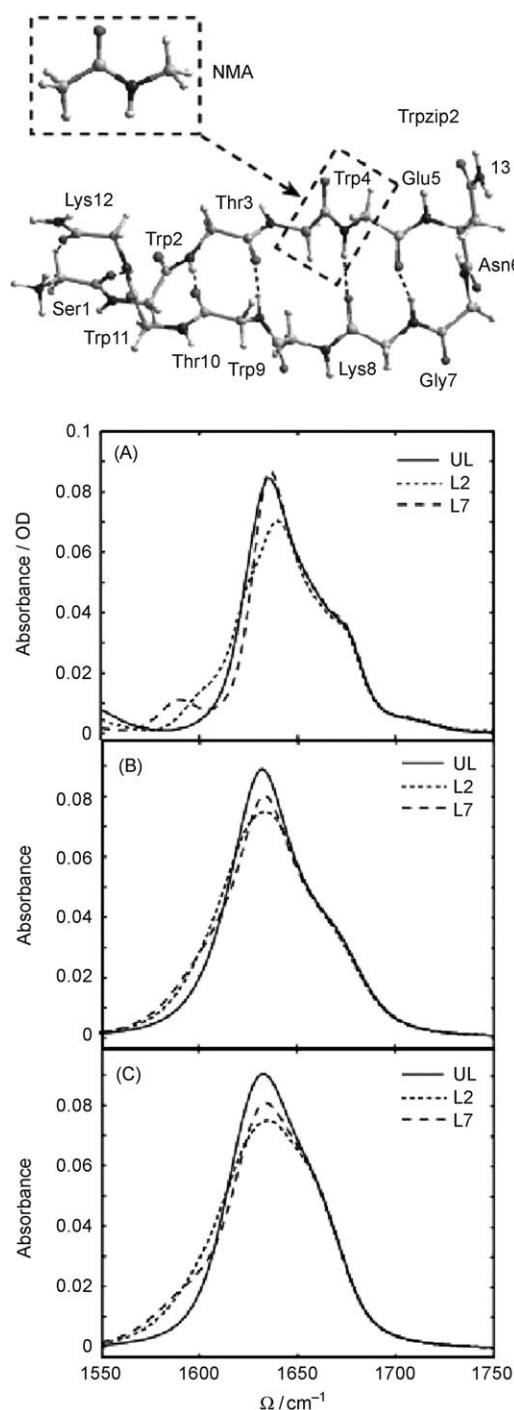


Figure 13. IR spectra of trpzip2 ^{13}C isotopomers; solid lines: UL; dashed lines: L2; dotted lines: L7. A) Experimental, B) simulated using HC electrostatic potential model,^[158] C) simulated using the HM multipole field model.^[142]

diagonal and off-diagonal peaks, change upon ^{13}C -labeling as shown in Figure 14 panels B and C. The spectra simulated using the HC model are shown in the middle row of Figure 14 and the HM simulations in the bottom row. The main 2DIR characteristics of the UL, L2, and L7 are reasonably reproduced by both models.

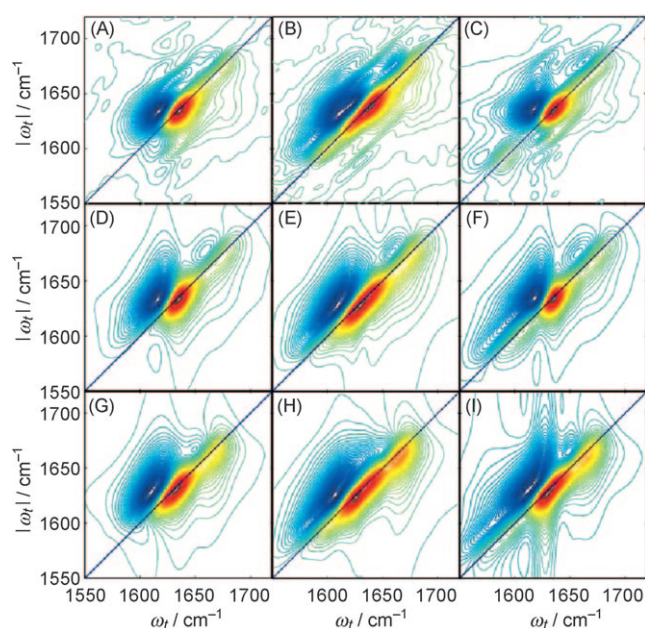


Figure 14. A–C) Experimental $k_{\parallel} + k_{\perp}$ spectra of trpzip2 ^{13}C isotopomers. D–F) simulations using the HC Hamiltonian operator,^[158] G–I) simulations results using the HM Hamiltonian operator.^[142] Left: UL, middle: L2; right: L7. ω_{τ} is Ω_1 in the notation of this Review, while ω_{τ} is Ω_3 .

The effect of the multiple state non-adiabatic crossing between amide-I vibrational energy surfaces which is neglected in these simulations was investigated recently.^[179]

5. Spectral Diffusion and Chemical Exchange: The Stochastic Liouville Equations

The Cumulant expressions used in Section 4 provide a simple compact description of bath fluctuations with Gaussian statistics coupled linearly to the frequencies. More general types of fluctuations require an expanded phase-space that includes relevant collective bath modes and to compute the evolution of distributions in this extended space. This requirement can be accomplished using the stochastic Liouville equations (SLE) proposed by Kubo^[180–183] to represent the dynamics of the distribution of a quantum system perturbed by a stochastic process described by a Markovian master equation. The SLE is widely used in the simulations of electron spin resonance (ESR),^[184,185] NMR,^[183] and IR^[186,187] line shapes.

Below we apply this method to simulate 2DIR spectra and the chemical exchange processes of a small peptide, trialanine.^[188] Trialanine has two amide bonds which contribute to its amide-I band. The Hamiltonian operator depends on the frequencies ω_a and ω_b , anharmonicities K_a and K_b , and the coupling constant J of the two local modes. The simulations presented below include six vibrational energy levels: the ground state (g), two single excited levels (e_1 and e_2) and three doubly excited levels (f_1 , f_2 , and f_3 ; see Figure 9 in Section 4). The time evolution of the density matrix describing the state

of the two mode system is described by the Liouville Equation (23).

$$\frac{\partial}{\partial t} \rho(t) = -\frac{i}{\hbar} \mathbf{L}(t) \rho(t) - \frac{i}{\hbar} \mathbf{L}_{\text{int}}(t) \rho(t) \quad (23)$$

$\mathbf{L}(t) \rho(t) = -\frac{i}{\hbar} [H_0(t), \rho(t)]$ represents the isolated system, while $\mathbf{L}_{\text{int}}(t) \rho(t) = -\frac{i}{\hbar} [H_{\text{int}}(t), \rho(t)]$ represents the coupling with the radiation field.

Analysis of the amide-I absorption band of trialanine^[100,189–191] suggests that it primarily exists in the polyglycine II (P_{II}) structure (a conformation characterized by Ramachandran angles of $(\psi, \phi) = (-60^\circ, +140^\circ)$ and a right hand α -helix (α_R) $(\psi, \phi) = (-60^\circ, +45^\circ)$.^[192] We found 70 % P_{II} configuration and 30 % α_R in the joint distribution of the Ramachandran angles derived by the MD trajectory. The Ramachandran-angle distribution functions for each configuration were fitted to a Gaussian form. The two configurations are stable and only 38 transitions between them occurred during the 10 ns simulation, suggesting an exchange time of a few hundred picoseconds for the two species, which is too slow to affect the line shapes. The response was thus calculated as an inhomogeneous average over the two species. The non-adiabatic effect of the two-state curve crossings has been also investigated.^[179]

The frequency fluctuations of the two modes ($\delta\omega_a$) and ($\delta\omega_b$) are treated as independent stochastic variables. These are dominated by the interaction with the solvent water molecules in the vicinity of each amide unit. The Brownian oscillator parameters (relaxation times $\gamma_a^{-1} = \gamma_b^{-1} = 220$ fs and magnitudes $\Delta_a = \Delta_b = 16.1$ cm⁻¹) reproduce the experimental line shape for the isolated amide-I mode in NMA.^[159] The fundamental frequencies are given by $\omega_a = \langle\omega_a\rangle + \delta\omega_a$ and $\omega_b = \langle\omega_b\rangle + \delta\omega_b$ with average frequencies $\langle\omega_a\rangle = 1652$ and $\langle\omega_b\rangle = 1668$ cm⁻¹.^[189,190] The difference stems from the charge on the terminal amino group; the amide unit closest to the acid group has the lower frequency.

Ramachandran-angle fluctuations ($\delta\phi$ and $\delta\psi$) constitute another set of relevant stochastic variables that primarily affect the intermode coupling J . J was expanded to quadratic order to give Equation (24).

$$J(\delta\phi, \delta\psi) = \sum_{i=0}^2 \sum_{j=0}^2 C_{ij} \delta\phi^i \delta\psi^j \quad (24)$$

C_{ij} were obtained by a fit to the TT map which connects the coupling constant and the Ramachandran angles.^[146] C_{00} represents the coupling at the average Ramachandran angles which is the reference point for the Taylor expansion. We found $C_{00} = 4$ cm⁻¹ in the P_{II} configuration and 10.5 cm⁻¹ for α_R .

All four stochastic variables ($\delta\omega_a, \delta\omega_b, \delta\phi$, and $\delta\psi$) are treated as Brownian-oscillators, each characterized by two parameters Δ (variance of fluctuations) and γ (relaxation rate). The local anharmonicities defined as the differences between the double of the fundamentals and the overtone

frequencies were fixed to 16 cm⁻¹, their fluctuations were neglected.^[53,98,193] Transition dipole fluctuations of the local modes were neglected as well and their magnitudes were set to unity.

The probability distributions $P(\mathbf{Q}, t)$ of our stochastic variables $Q_1 = \delta\omega_a$, $Q_2 = \delta\omega_b$, $Q_3 = \delta\phi$, and $Q_4 = \delta\psi$, is modeled by the Markovian master Equation (25) where $\Gamma(\mathbf{Q})$ has the Smoluchowski (overdamped Brownian Oscillator) form [Eq. (26)].

$$\frac{\partial P(\mathbf{Q}, t)}{\partial t} = -\Gamma(\mathbf{Q}) P(\mathbf{Q}, t) \quad (25)$$

$$\frac{\partial P(\mathbf{Q}, t)}{\partial t} = -\sum_{j=1}^4 \gamma_j \frac{\partial}{\partial Q_j} \left(Q_j + \Delta_j^2 \frac{\partial}{\partial Q_j} \right) P(\mathbf{Q}, t) \quad (26)$$

The SLE is finally constructed by combining the Liouville equation for the exciton system [Eq. (23)] and the Markovian master equation [Eq. (25)] for the four collective Brownian oscillator coordinates [Eq. (27)].

$$\dot{\rho}(\mathbf{Q}, t) = -\frac{i}{\hbar} \mathbf{L}(\mathbf{Q}) \rho(\mathbf{Q}, t) - \Gamma(\mathbf{Q}) \rho(\mathbf{Q}, t) \quad (27)$$

The SLE may be solved using a matrix continued-fraction representation of the Green functions,^[188] in the frequency domain. The 2DIR photon-echo signal $S_k(\Omega_1, t_2, \Omega_3)$, was computed by transforming the frequency Ω_2 back to the time domain [Eq. (28)].

$$S_k(\Omega_1, t_2, \Omega_3) = \text{Im} \int_{-\infty}^{\infty} d\Omega_2 R_k(\Omega_1, \Omega_2, \Omega_3) \exp(-i(\Omega_2 t_2)) \quad (28)$$

The Green function for the t_2 interval may also be computed in the time domain by a direct time integration of the SLE. Different levels of simulation of all parallel $zzzz$ signals were compared in Ref. [194]. The highest level includes fluctuations of all four collective bath coordinates. The Liouville operator is constructed in the local basis and the coupling between the two local modes fluctuates with the Ramachandran angles. The local-mode frequencies fluctuate as well. Satisfactory agreement with experiment is obtained as shown in Figure 15. Some differences arise since the α_R population is overestimated by the MD simulation. Stock et al.^[195] demonstrated that different MD force fields predict very different populations of the various conformations of trialanine. However, the SLE need not necessarily rely on MD simulations and can use for example, parameters obtained from NMR spectroscopy.

In summary, four collective coordinates can account for the effect of fluctuations on the two amide-I modes for trialanine. Ramachandran angle fluctuations have significant signatures on 2DIR line shapes in non-rigid peptides.

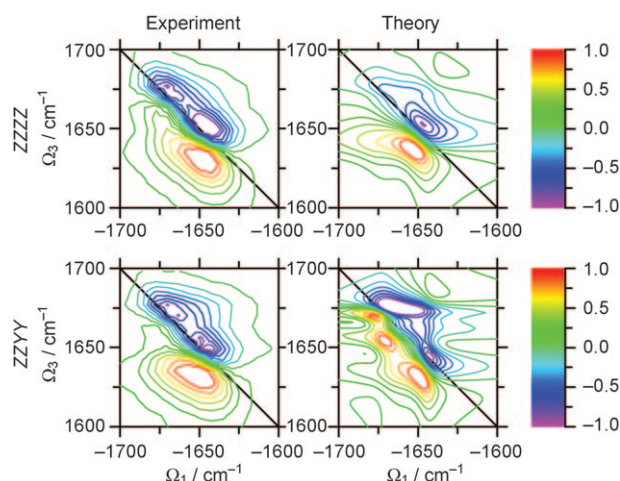


Figure 15. Top: The experimental k_i photon-echo spectrum of trialanine^[194] (left) and the simulated spectrum (right) for parallel polarized pulses. Bottom: Same comparison but for perpendicular polarized pulses. The spectra are normalized to the most intense peak.

The exchange between conformers in trialanine is slow and the signal is given by a sum of the contributions of the various conformers. Fast-exchange shows interesting signatures in 2D signals as demonstrated in hydrogen-bonding and isomerization dynamics.^[196] These can be described by including a multistate jump model in the SLE. The Brownian-oscillator motion and the exchange process show different 2DIR signatures. In the following simulations we allowed a different width for the u and d peaks. The splitting $2\Delta_0 = 34 \text{ cm}^{-1}$ (i.e. ca. 1.01 ps^{-1}) and the exchange rates $k_u = 0.1 \text{ ps}^{-1}$, $k_d = 0.125 \text{ ps}^{-1}$ were taken from the cross-peaks growth reported in Ref. [136]. All three regimes were observed experimentally in the formation and dissociation of phenol-benzene complexes in CCl_4 solution.^[136] In the intermediate timescale regime (2 ps), memory of the Brownian oscillator coordinate is lost as evident by the circular line shape but the cross-peaks are weak. We thus assumed a $\Lambda \approx 0.4 \text{ ps}^{-1}$ relaxation rate. Λ, Ω_1 , and Ω_3 can be estimated from the absorption linewidth using the Pade approximate of a two-level system.^[66] Using $\Omega_1 = 0.33 \text{ ps}^{-1}$, $\Omega_3 = -0.07 \text{ ps}^{-1}$ simulations reproduced the experimental absorption spectra. The 2DIR-photon-echo signals shown in Figure 16 recover all experimental features; all three regimes are clearly seen a) rephasing elliptic shapes, b) the relaxed Brownian oscillator with circular shape, and c) chemical-exchange cross-peaks as found experimentally (the lower frequency peak is weaker but broader^[136]).

The SLE can be used to describe many types of fluctuations of all the elements of the Hamiltonian operator. The only requirement is that they can be represented by a few (discrete or continuous) collective coordinates that satisfy a Markovian equation of motion. These equations account for the effect of the fluctuations of collective bath coordinates on the nonlinear IR spectra by describing the evolution in the joint system-and-bath space.

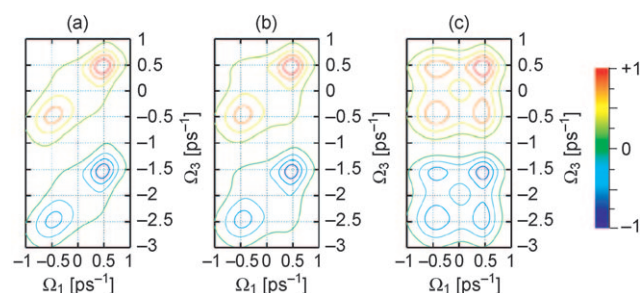


Figure 16. Simulated 2DIR signals $S_A = k_i + k_{jj}$ for exchange $\Omega_1 = 0.5 \text{ fs}^{-1}$, $\Lambda = 0.4 \text{ ps}^{-1}$; $\Omega_2 = 0.33 \text{ ps}^{-1}$, $\Omega_3 = -0.07 \text{ ps}^{-1}$; $k_d = 0.125 \text{ ps}^{-1}$, $k_u = 0.1 \text{ ps}^{-1}$; $\Delta_0 = -2.0 \text{ ps}^{-1}$; $\Delta_3 = \Delta_1 = 0$. Time delays: a) $t_2 = 0$; b) $t_2 = 2 \text{ ps}$; c) $t_2 = 10 \text{ ps}$. These spectra closely resemble the experimental results of Ref. [136].

6. The OH Stretch Band of Liquid Water

Liquid water has many unique properties stemming from its unusual capacity to form multiple hydrogen bonds, making it the most important solvent in biology. These bonds and their fluctuations have been extensively studied.^[92,121,175,197–206]

The vibrational OH stretch band is complicated by resonant exciton transfer to neighboring molecules.^[175,204,207–210] The spectrum of HOD in D_2O has received considerable attention since it is a simpler model system where such transfer is not possible (OH frequency is 3400 cm^{-1} , OD frequency is 2500 cm^{-1}).^[211] The absorption bandwidth of the OH stretch of the HOD/ D_2O ^[120,212,213] is 255 cm^{-1} (full width at half maximum height (FWHM))^[212] and shows a 307 cm^{-1} ^[212] solvent red shift from the gas phase frequency 3707.47 cm^{-1} .^[214] A 70 cm^{-1} vibrational Stokes shift in IR fluorescence was reported by Woutersen and Bakker^[215–219] Vibrational relaxation and hydrogen-bond dynamics were also probed by spectral hole burning, two-pulse photon-echo experiments, and photon-echo peak shift.^[120,213,220,221] An observed oscillation was attributed to a coherent hydrogen-bond motion, as verified by simulations.^[120,222] Similar photon-echo experiments and simulations were carried out on a complementary system (OD stretch of HOD in H_2O).^[122,223] It was recently proposed that the fifth-order nonlinear IR experiment (3D-IR)^[224] can monitor the three-point frequency fluctuation correlation function, revealing the relation between the spectroscopic coordinates and dynamic coordinates of hydrogen-bond rearrangements.^[225]

The electrostatic ab initio map approach described in Section 3 was employed to simulate the O–H stretch fundamental and its overtone.^[226] The anharmonic vibrational potential of HOD expanded to the 6th order in the three normal coordinates (H–O–D bending, O–D stretch and O–H stretch) in the multipole electric field were calculated at the MP2/6-31 + G(d,p) level. Simulated CGF solvent-induced peak shift and bandwidth (Figure 17; 287 cm^{-1} and 309 cm^{-1}) are in good agreement with experiment (306 cm^{-1} and 250 cm^{-1} ; Figure 17)

A collective electrostatic coordinate (CEC) Ω was introduced for the O–H stretch; a linear combination of the multipole electric-field coefficients which is defined as a

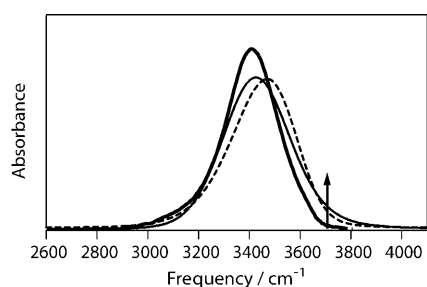


Figure 17. Simulated linear IR O–H stretch line shape calculated with the CGF (thin solid line) and the SLE (thin dashed line) as well as the experimental data (thick solid line).^[120] The black vertical arrow represents the gas-phase frequency.^[214]

linear part of the electrostatic frequency map [Eq. (6) in Section 3.1] in **C** around the average $\langle \mathbf{C} \rangle$ [Eq. (29)].

$$\Omega \approx 189.7 \frac{\text{cm}^{-1} \text{\AA}}{\text{V}} \delta E_z + 77.7 \frac{\text{cm}^{-1} \text{\AA}^2}{\text{V}} \delta E_{xx} - 39.5 \frac{\text{cm}^{-1} \text{\AA}^2}{\text{V}} \delta E_{zz} \quad (29)$$

We use the coordinate system shown in Figure 17. The frequency fluctuations are well described by a quadratic polynomial in Ω [Eq. (30)].

$$\omega \approx \omega_{\text{eq}} + \Omega + \frac{\kappa}{\omega_{\text{eq}}} \Omega^2 \quad (30)$$

The scatter plot of the frequencies calculated with selected electrostatic components versus the full component calculation given in Figure 18 shows that three (E_z , E_{zz} , and

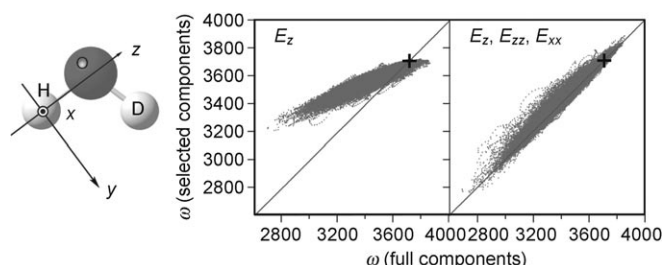


Figure 18. Scatter plots of the frequencies calculated with various electrostatic components versus the full calculation. Crosses represent the gas-phase frequency,^[214] and diagonal lines represent the perfect agreement. Left: E_z ; right: E_z , E_{zz} , E_{xx} . All axes are in cm^{-1} .

E_{xx}) components dominate the overall frequency shift from the gas phase. The frequencies calculated with only E_z (Figure 18 left panel) are systematically too high, indicating the significant contribution of E_{zz} and E_{xx} to the O–H stretch frequency. E_{xx} is dominated by the hydrogen bonding of oxygen of HOD to the deuterium of D_2O solvent. The partial charge of deuterium in D_2O creates the diagonal negative gradient of the out-of-plane electric field, and the simulated ensemble average values of $\langle E_{xx} \rangle$ (-0.0094) verifies this point.

The CEC correlation function shows biexponential decay. The CEC was therefore decomposed into a sum of a fast (Ω_1) Brownian oscillator coordinate representing hydrogen-bonding fluctuations and a slow (Ω_2) coordinate representing the solvent fluctuations outside of the first solvation shell ($\Omega = \Omega_1 + \Omega_2$). The relaxation times for Ω_1 and Ω_2 are $\tau_1 = 34.4$ fs and $\tau_2 = 0.501$ ps. Two stochastic models, the collective electric coordinate (CEC) and four state jump (FSJ) were employed for simulating the effects of hydrogen-bonding fluctuations Ω_1 on the line shapes.^[226,227] The CEC model assumes two CEC (Ω_1 and Ω_2) which describe fast and slow fluctuations assuming the continuous Gaussian processes. The FSJ model uses a master equation to describe the jumps between four hydrogen-bonding configurations in addition to the slow CEC fluctuation (Ω_2). Twelve hydrogen-bonding configurations were obtained by employing the geometric hydrogen-bonding criteria.^[203,228,229] These were clustered into four groups, configuration I (one hydrogen bond to each hydrogen and two to oxygen), II (one hydrogen bond to each hydrogen and less than two to oxygen), III (no hydrogen bond to hydrogen, but two hydrogen bonds to oxygen), and IV (no hydrogen bonds to hydrogen and less than two hydrogen bonds to oxygen).

While the CGF band shape is symmetric, the CEC model predicts an asymmetric band with a long red tail, consistent with experiment (Figure 17).^[120] The anti-diagonal linewidths of photon-echo signal in CGF and CEC are about the same at low and the high frequency (Figure 19). However the four state jump linewidth is 23 cm^{-1} larger for higher frequencies, despite the fact that the frequency distribution is broader for the low-frequency configuration I. The blue section in the experiment as marked in Figure 19 is 19 cm^{-1} broader than the red section. We define the symmetry parameter η in terms of the FWHM line widths of the red (Γ_R) and the blue (Γ_B) anti-diagonal slices (Figure 19): $\eta = (\Gamma_B - \Gamma_R)/(\Gamma_B + \Gamma_R)$. The FSJ asymmetry parameter η (0.125; Figure 19 top row, middle panel) is in better agreement with experiment (0.0848)^[230] than CEC (0.0138; Figure 19 top row, left). The CGF simulation gives a symmetric band shape along the diagonal black line (Figure 19, bottom) and misses the observed asymmetry.

The experimental η suggests that the shorter lifetime of the high-frequency hydrogen-bond species gives rise to a considerable line broadening. Hydrogen-bond kinetics are much faster than the slow dynamics responsible for the frequency distribution of the individual species. The triangular shape of the diagonal photon-echo peak can be attributed to fast femtosecond hydrogen-bonding kinetics. In the FSJ model, breaking a hydrogen bond on oxygen affects both the fundamental OH frequency and the anharmonicity more than breaking the hydrogen bond on the hydrogen atom. Hydrogen bonding to deuterium causes a blue shift.

We define the anharmonic shift as the frequency difference along the ω_3 axis between the peak positions of the stimulated emission and the ground state bleach peak. Anharmonic fluctuations add 10 cm^{-1} to the anharmonic shift. Hydrogen bonding to the H atom of HOD lowers the OH stretch vibrational potential of HOD more at longer O–H bond lengths, making the anharmonicity larger. Water in

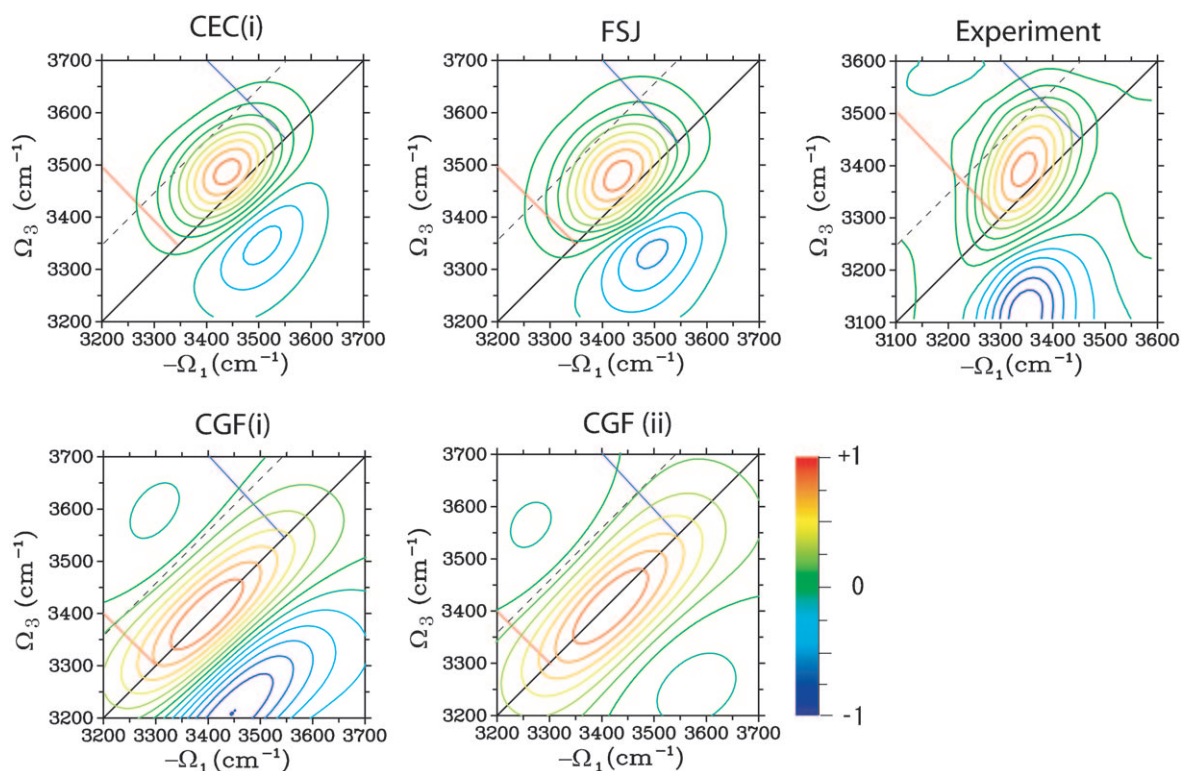


Figure 19. Comparison of the 2DIR photon-echo spectra, calculated using the two SLE and two CGF models, with the experimental data. The full black line is the diagonal, the dashed line is displaced 100 cm^{-1} above the diagonal. The red and blue lines show where the anti-diagonal slices are taken on the red and blue side, respectively, to calculate the asymmetry parameter η . CEC(i): SLE simulation using the CEC; FSJ: SLE simulation using the FSJ; CGF(i): CGF simulation; CGF(ii): CGF simulation with an infinite negative anharmonicity.

confined environments (membranes, interfaces, reverse micelles) can be effectively studied using 2DIR.^[231–233] Even-order signals $R^{(2)}$ and $R^{(4)}$ vanish in isotropic systems and thus provide very sensitive probes for interfaces.^[234–236] Sum frequency generation is a 1D technique. Multidimensional extensions are on the horizon.^[237]

Simulations of 2DIR spectra of neat liquid water (H_2O) must account for highly disordered coupled-resonant O-H stretch vibrations. In addition to the modulations of the transition frequencies, which also exist in the HOD/ D_2O system, dipole moments, and anharmonicities fluctuations of the intermolecular coupling in the extended hydrogen-bond network now become relevant. The first photon-echo studies^[123,175] on neat H_2O have revealed significantly faster structural dynamics than HOD in D_2O . This result was attributed to a stronger coupling to librational motions, with possible contributions from resonant energy transfer and delocalization of the vibrational excitations.

Simulations of the 2DIR photon-echo and pump-probe response of the O-H stretch vibrations of liquid water^[238] were performed by a direct numerical integration of the Schrödinger equation, including both symmetric and antisymmetric stretches, intermolecular couplings, as well as fluctuations and anharmonicities of transition frequencies and dipole moments. This simulation allows for multiple-state non-adiabatic crossings between vibrational energy surfaces on any time scale.

The dielectric constant was used to scale the resonant dipole-dipole coupling and reproduce the observed polarization anisotropy decay (80 fs). The next-neighbor coupling strength (12 cm^{-1}) gives the best agreement. A lifetime of 200 fs is assumed. Figure 20 shows that the simulated peak shapes, amplitudes, and dynamics are in close agreement with experiment. The negative and positive peaks correspond to the fundamental transition and the excited-state absorption,

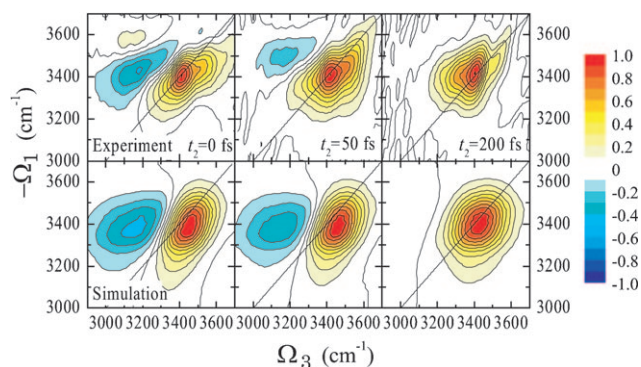


Figure 20. 2DIR photon-echo spectra ($\mathbf{k}_i = -\mathbf{k}_1 + \mathbf{k}_2 + \mathbf{k}_3$) of the O-H stretch vibration in H_2O for population times $t_2 = 0, 50, 200\text{ fs}$. Top: experimental data,^[123] bottom: simulations using a direct numerical propagation. Each spectrum is normalized to its maximum. (adapted from Ref. [238]).

respectively. In both experiment and simulation, the fundamental peak is stretched along the diagonal, indicating some initial inhomogeneity at $t_2 = 0$ fs. As t_2 is increased, the peak orientation becomes more vertical. The bending of the fundamental peak and the nodal lines between the two peaks indicates faster fluctuations and loss of inhomogeneity on the red side of the spectrum. Initial correlations on the red side of the spectrum decay in 100 fs, but persist beyond 200 fs in the blue side.

The large number of acceptor modes, as well as anharmonicities and fluctuations in water open up many intermolecular transfer pathways, which lead to a full decay of the polarization anisotropy on observed time scales (80 fs) even though the average coupling (12 cm^{-1}) is weak. The effect of resonant energy transfer on the 2DIR photon-echo spectra is found to be rather small for short t_2 time (< 200 fs). Most of the fast dynamics in the 2DIR photon-echo spectrum are caused by the local O-H stretch frequency fluctuations owing to the sensitivity of the local anharmonic potential to the fluctuating hydrogen-bonding environment. The O-H stretch vibration is an excellent probe of the hydrogen-bond network in H_2O . 2DIR of other liquids, such as formamide, may be simulated using the same approach.^[239–241]

The study of water dynamics in confined biological,^[249,250] chemical,^[251] and geological^[252] environments is of considerable theoretical and experimental interest.^[231–233,242–248]

Considerable 2DIR activities had focused on reverse micelles, in particular aerosol OT (AOT). Studies of the OH stretch absorption of diluted HOD in a droplet of D_2O or H_2O ^[242–245] have shown that the dynamics of the confined water is slower than in the bulk. Using stimulated vibrational echo and spectrally resolved vibrational echo peak shift, Fayer and co-workers have shown that the fastest dynamics resulting from hydrogen-bond-length fluctuations (50 fs) in confined water is similar to the bulk, but the timescale of the slower global structural evolution (> 1 ps) could increase by an order of magnitude in strongly confined systems.^[244,245] The dynamics of neat water in reverse micelles has been reported as well.^[231,233,246] IR pump-probe and vibrational-echo spectroscopy support the existence of two independent relaxing water sub-ensembles.^[231,233] The dynamics of the core of the droplet is similar to the bulk, but the shell is slower. A 0.4 nm shell thickness has been measured.^[231] The confinement of water in phospholipids membranes has been studied as well.^[232,247,248] In contrast to reverse micelles where the confinement induces a core-shell separation, water dynamics in membranes is dominated by strong hydrogen bonds with the phospholipid polar groups.

7. Application to Phospholipids: Quasiparticle Representation of 2DIR Signals

As a constituent organelle in the cell,^[253] the membrane sets the information and energy gradients and controls their flow, which is essential for life. The common structural moieties in the polar surface of cellular membranes, carbonyl, phosphate, and chlorine mediate molecular recognition and signal transduction.^[253,254] Owing to experimental limitations,

our knowledge of their arrangement and dynamics is not very detailed. In a lipid bilayer, lateral irregularities smear the neutron scattering diffraction pattern, and NMR resonances are broad because of the restricted motions which result in incomplete motional narrowing, as found in solid-state NMR spectroscopy. IR spectra of the carbonyl moieties in phospholipid membranes has attracted considerable attention.^[255–259] The absorption-band shows a clear inhomogeneous character and can be described as a superposition of several sub-states.^[255,256] Carbonyl stretching line-shapes in phospholipids could yield direct information about molecular architecture and fluctuations in the membrane interface.^[260,261] There are many sources for the high spectral inhomogeneity differences found in the local environment of the sn-1 and sn-2 carbonyl moieties, these stem from the packing arrangements,^[256,258] local chain conformations,^[258,259,262–264] the relative positions of the two carbonyls with respect to the interface,^[132,259,265] and the degree of hydration.^[266,267] In an elegant study, Blume et al.^[266] ruled out all scenarios involving local structural differences except hydrogen bonding. Another study^[268] similarly eliminated the variance in hydration as a possible source of inhomogeneity.

Figure 21 shows a bilayer of the phospholipid dimyristoylphosphatidylcholine (DMPC)^[107] The 2DIR of the C=O stretch band of this bilayer is shown in Figure 22. The sn-1 and sn-2 carbonyl degeneracy is lifted by a ^{13}C labeled carbon in the sn-2 chain, giving two broad vibrational bands at 1740 and 1697 cm^{-1} .

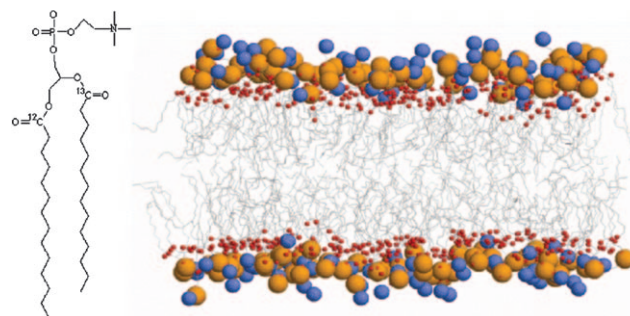


Figure 21. Chemical structure of the DMPC phospholipid and a snapshot of the DMPC bilayer taken from the MD simulation (for clarity the water molecules are not shown). Orange P, blue N, and red O. The hydrophobic tails are shown with sticks.

The SOS method described in Section 3 requires the diagonalization of the two-exciton block of the Hamiltonian matrix. The N^4 scaling of time makes computation prohibitively demanding for large N . An alternative, quasiparticle scattering, approach greatly reduces the computational demand. This method assumes a molecular Hamiltonian operator that conserves the number of excitations, and a dipole moment that can only create or annihilate one excitation. The optical transitions are viewed as quasiparticles (“excitons”), and the nonlinearity now originates from their collisions.

The amide-I Hamiltonian [Eq. (3)] can be approximately recast in terms of Bosonic creation and annihilation operators

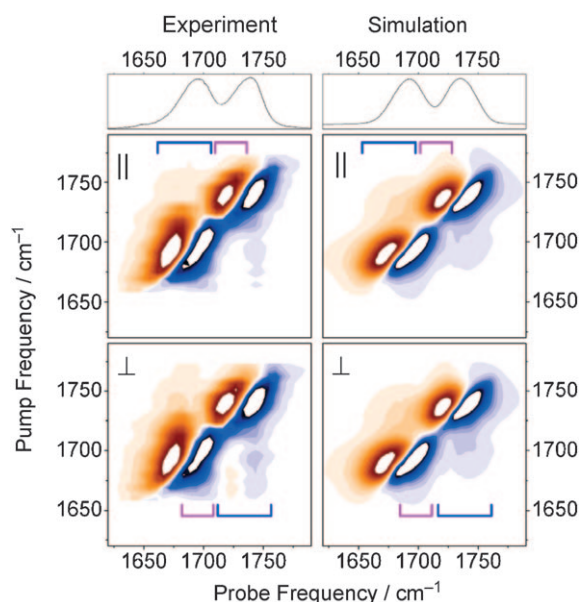


Figure 22. Left column: experimental pump–probe spectra of the carbonyl groups in phospholipid membrane fragments. From the top: absorption, and pump–probe spectra recorded under parallel and perpendicular polarization conditions of the pump and probe pulses. Right Column: The corresponding simulated spectra. Blue and magenta brackets show the inter- and the intra-band cross-peak regions, respectively.^[107]

[Eq. (31)], where B^\dagger and B are creation and annihilation Boson operators, respectively, satisfying $[B_m^\dagger, B_n] = \delta_{nm}$. The

$$\hat{H} = \sum_m \omega_m \hat{B}_m^\dagger \hat{B}_m + \sum_{m,n}^{m \neq n} J_{mn} \hat{B}_m^\dagger \hat{B}_n - \frac{1}{2} \sum_m \Delta_m \hat{B}_m^\dagger \hat{B}_m^\dagger \hat{B}_m + \sum_{m,n}^{m \neq n} K_{mn} \hat{B}_m^\dagger \hat{B}_n^\dagger \hat{B}_m \hat{B}_n \quad (31)$$

first two terms describe the free excitons where ω_m is the local amide-I frequency and the J_{mn} represents the inter-site coupling which induces exciton hopping. Δ_m and K_{mn} represent the intra- and inter-site anharmonicity, respectively.

The quasiparticle picture appears naturally by solving equations of motion, the nonlinear exciton equations (NEE).^[62,64] A key ingredient is the Green function, \mathcal{G} , which describes the time evolution of two excitons and satisfies the Bethe–Salpeter Equation (32).

$$\mathcal{G}(\Omega) = \mathcal{G}^{(0)}(\Omega) + \mathcal{G}^{(0)}(\Omega) \Gamma(\Omega) \mathcal{G}^{(0)}(\Omega) \quad (32)$$

$\mathcal{G}^{(0)}$ represents the dynamics of two non-interacting excitons. Γ is the two-exciton scattering matrix. Its matrix element $\bar{\Gamma}_{e_4 e_3, e_2 e_1} \Omega^{[61]}$ represents a process where two incoming excitons e_1 and e_2 are scattered to produce e_3 and e_4 .

Formally the computational effort of both the quasiparticle expression and the SOS scale as N^4 with system size. However, a much more favorable scaling is obtained in

practice thanks to the localized nature of excitons and their interactions (anharmonicities).^[55] To see how this works, the overlap factor of two excitons needs to be considered [Eq. (33)].

$$\eta_{ee'}^{(1)} = \sum_m |\psi_{e,m} \psi_{e',m}| \quad (33)$$

This parameter characterizes the two-exciton configuration in real space: for $e = e'$ we have $\eta_{ee}^{(1)} \equiv 1$. For uncoupled vibrations $J_{mn} = 0$ and $\eta_{ee}^{(1)} = \delta_{ee}$ indicating that the excitons do not interact. Since exciton interactions are short-range (the anharmonicity is local) we can estimate the probability of the scattering event by assuming that exciton pairs ($e_1 e_2$) can only scatter when their overlap is larger than a certain cut-off $\eta_c: \eta_{e_1 e_2}^{(1)} > \eta_c$. The same criterion may also be used for the pairs of outgoing states ($e_4 e_3$). By applying this cut-off which restricts the distance between two initial and between two final excitons in the scattering matrix the number of relevant scattering matrix elements should scale as $N^2 N_c^2$ rather than N^4 , where N_c is a finite correlation length; the scattering matrix is sparse.

A second helpful constraint is provided by the exciton–exciton scattering radius which determines how far two excitons can move during their interaction, and sets bounds on the distance between the initial and final pairs of excitons. We introduce this cut-off by defining a second overlap parameter [Eq. (34)].

$$\eta_{ee'}^{(2)} = \sum_{e_1, m, n} |\psi_{e_1, m} \psi_{e_1, n} \psi_{e, m} \psi_{e', n}| \quad (34)$$

$\eta^{(2)}$ is the amplitude of a path going from e to e' through all possible intermediate states e_1 . A cut-off of $\eta_{ee'}^{(2)}$ may be used to select the dominant $e_3 e_2$ pairs in the scattering matrix $\Gamma_{e_4 e_3, e_2 e_1}$.

Using both cut-off parameters $\eta_c^{(1)}$ and $\eta_c^{(2)}$, we can retain only those scattering matrix elements which satisfy $\eta_{e_2 e_1}^{(1)} > \eta_c^{(1)}$, $\eta_{e_4 e_3}^{(1)} > \eta_c^{(1)}$, $\eta_{e_3 e_2}^{(1)} > \eta_c^{(2)}$, $\eta_{e_1 e_4}^{(1)} > \eta_c^{(2)}$, and $\eta_{e_4 e_1}^{(1)} > \eta_c^{(2)}$. The scaling of the NEE effort with system size thus reduces to N . The reduction in computational effort, which becomes more pronounced as the system size is increased, stem from two factors: 1) The relevant exciton states may be identified before calculating the scattering matrix. Their number is typically much smaller than N^4 . The scattering matrix should be calculated only for the selected set of scattering configurations. 2) The required numerical effort for computing the signal using multiple summations is reduced considerably by the sparse nature the scattering matrix.

Figure 22 shows the experimental and simulated pump–probe spectra of carbonyl moieties in a phospholipid bilayer for parallel and perpendicular polarization configuration of the pump and the probe pulses. The local amide-I frequencies are 1708 cm^{-1} (^{13}C labeled) 1755 cm^{-1} (unlabeled) corrected by a Stark effect frequency shift: $\Delta\omega = kE_{\text{proj}}$, where E_{proj} is the projection of the electric field along the C=O bond. Off-diagonal elements were obtained by using the transition dipole coupling model.^[149] The experiment uses a spectrally

narrow (16 cm^{-1}) pump and a short (100 fs) impulsive probe. The signal field is spectrally dispersed. The experimental bandwidths resulting from the fluctuating electrostatic environment as well as their (diagonally-elongated) shape characteristic to inhomogeneous broadening are reproduced by the simulations. The two strong diagonal resonances correspond to absorption by the two carbonyl groups.

The cross-peak regions in the 2D signal are weak. The two horizontal sections of the calculated and experimental signals are compared in Figure 23. The intensities and line shapes of

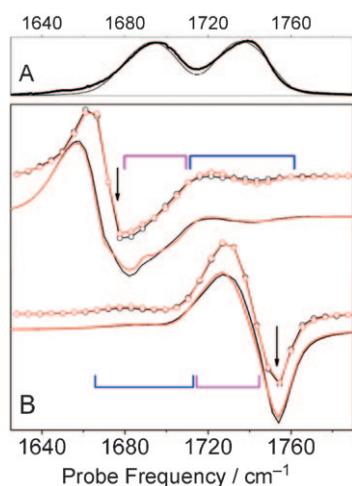


Figure 23. A) experimental absorption (thick line) and calculated linear optical absorption (thin line) of DMPC in water. B) Experimental (open circles) and calculated (solid lines) hole-burning spectra under pump excitation at 1675 and 1752 cm^{-1} (see arrows). Black (parallel) and red (perpendicular) colors indicate the polarization conditions. The perpendicular spectra are magnified by a factor three. Blue and magenta brackets mark the inter- and intra-band cross-peak regions, respectively (see also Figure 22).

both intra- and inter-band cross-peaks are fairly well reproduced. Each resonance has a negative (blue) contribution owing to GSB and ESE, and a positive (red) ESA contribution (see Figure 10). The red shift of the ESA band reflects the anharmonicity of the carbonyl stretching mode. The cross-peaks are more pronounced when the pump and the probe have perpendicular polarization (Figure 22, \perp). Figure 23 B depicts horizontal (\parallel) and perpendicular \perp sections of Figure 22 at the pump frequencies 1675 and 1752 cm^{-1} (marked by arrows). The cross-peaks provide a direct measure of vibrational coupling between carbonyl moieties. Structural information, such as the distribution of angles between intramolecular carbonyl pairing, may be obtained from quantitatively comparing the simulated and experimental results. The pairing geometry is expressed in terms of the angle between the transition dipole moments and their separation. The vibrational frequencies of the two coupled carbonyl groups ω_n and ω_m are obtained by diagonalizing the exciton Hamiltonian operator [Eq. (35)].

$$\mathbf{H}_{\text{red}} = \begin{pmatrix} \omega_n^0 & J_{mn} \\ J_{mn} & \omega_m^0 \end{pmatrix} \quad (35)$$

These depend on the coupling parameter J_{mn} and on the difference of the diagonal frequencies, $\omega_n^0 - \omega_m^0$. We further define the pair coupling parameters β'_{mn} [Eq. (36)] and the weighted radial angular pair distribution function [Eq. (37)], where the m and n sums run over the ^{12}CO and ^{13}CO carbonyl groups, respectively.

$$\beta'_{mn} = |\omega_m - \omega_n| - |\omega_m^0 - \omega_n^0| \quad (36)$$

$$h(R, \theta) = \left\langle \sum_{m \in {}^{12}\text{CO}} \sum_{n \in {}^{13}\text{CO}} \beta'_{mn} \delta(R - R_{mn}) \delta(\theta - \theta_{mn}) \right\rangle \quad (37)$$

Figure 24 shows $h(R, \theta)$ calculated by considering all $^{12}\text{CO}:$ ^{13}CO pairs (A), only the intermolecular pairs (B), and only the intramolecular pairs (C). Panel A in Figure 24 shows that $h(R, \theta)$ vanishes for distances of $> 6.5\text{ \AA}$ implying

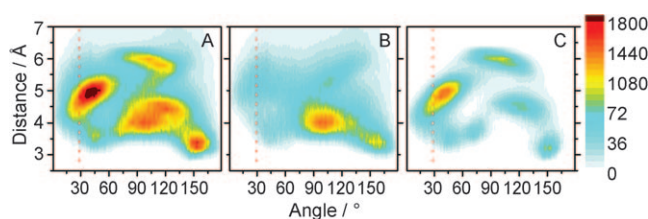


Figure 24. β' -weighted radial-angular distribution functions [Eq. (37)] of the simulated DMPC bilayer, calculated considering A) all $^{12}\text{CO}-^{13}\text{CO}$ pairs, B) $^{12}\text{CO}-^{13}\text{CO}$ intermolecular pairs, and C) $^{12}\text{CO}-^{13}\text{CO}$ intramolecular pairs. The red dotted lines indicate the angular values obtained from experimental spectral anisotropy. The chromatic bar shows the range of the statistical distribution according to Equation (37).

that the cross-peaks are dominated by neighboring carbonyl groups. The distribution function $h(R, \theta)$ (Figure 24 A), consists of several structural families whose intermolecular or intramolecular origin can be easily traced by comparison with Figure 24 B and C. The intermolecular $h(R, \theta)$ does not show random orientations even when it is broader than its intramolecular counterpart. The sharp peak at $\theta = 40^\circ$ and $R = 5\text{ \AA}$ in Figure 24 C is in agreement with the angle between the transition dipole moments obtained from the experimental anisotropy, suggesting that it is mainly due to intramolecular pairs. We note that for this angle, intermolecular carbonyl pairs also contribute significantly (up to $26 \pm 5\%$ to the total $h(R, \theta)$ function (see Figure 24).

These simulations reveal the important role of electrostatic interactions at the polar interface. Both the transition dipole moment coupling and the electric-field fluctuations affect the absorption band line shape. The two contributions, which are convoluted and indistinguishable by the linear response, can be clearly separated in the diagonal and in the off-diagonal parts of the 2D correlation plots. The cross-peak intensity provides a direct measure of the contribution of coupling to the overall line shape. The diagonal elongation results from both the frequency dispersion of the excitonic states and the local electric field fluctuations. The 2D line

shapes provide a unique window into the vibrational excitations. The increased degree of localization of the excitonic states in the absorption tails reflects local structural properties of the nearest chromophores.

2DIR combined with quasiparticle simulations provide a promising structural tool for studying composite phospholipid bilayers, host–guest lipid–protein complexes, lipid systems of reduced dimensionality, and polymers.

8. Double-Quantum-Coherence Spectroscopy

Elaborate pulse sequences are routinely designed in NMR spectroscopy to extract desired information. Similarly interferences between quantum pathways underlying multidimensional signals may be manipulated to design new 2DIR techniques. Herein we demonstrate a signal designed to vanish for non-interacting excitons thereby providing an excellent probe for such interactions.

The applications presented so far focused on the $\mathbf{k}_I = -\mathbf{k}_1 + \mathbf{k}_2 + \mathbf{k}_3$ and $\mathbf{k}_{II} = \mathbf{k}_1 - \mathbf{k}_2 + \mathbf{k}_3$ signals. The $\mathbf{k}_{III} = \mathbf{k}_1 + \mathbf{k}_2 - \mathbf{k}_3$ signal carries different types of information. It is given by the two quantum pathways ESA1 and ESA2 (Figure 25), analogous to the double quantum coherence

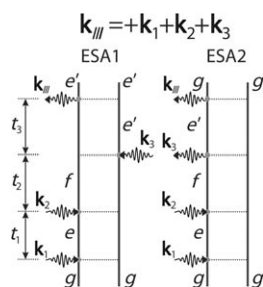


Figure 25. Double-sided Feynman diagrams representing the Liouville space pathways contributing to the signal in the rotating-wave approximation. The first excited-state absorption (ESA1) diagram corresponds to R_7 and the second excited-state absorption (ESA2) diagram to R'_4 .

technique in NMR spectroscopy.^[269] In both diagrams the system is in a coherent superposition of the doubly excited state f and the ground state g during t_2 . This time-interval thus provides a clean view of two-exciton states. We shall consider (Ω_2, Ω_3) 2D spectra obtained by varying the t_2 and t_3 delays. (Ω_1, Ω_2) signals are also possible.

As Ω_2 is scanned, the signal shows resonances corresponding to the different doubly excited states f . However, the projection along the other axis (Ω_3) is different in the two diagrams. In ESA2 the system is in a coherence between e' and g during t_3 . As Ω_3 is scanned, it reveals single exciton resonances when $\Omega_3 = \omega_{e'g}$. For ESA1 the system is in a coherence between f and e' during t_3 . This situation gives rise to many new resonances at $\Omega_3 = \omega_{fe}$ corresponding to all the possible transitions between doubly and singly excited states. The remarkable point is that for non-interacting excitons the state f is simply given by a direct product of the single pair states e and e' , the double-excitation energy is the sum of the

single-excitation energies, and the two diagrams exactly cancel. The resonance pattern of these 2D correlation plots provides a characteristic fingerprint for the correlated nature of two excitons.

The enhanced resolution of \mathbf{k}_{III} signals stems from the absence of diagonal peaks which dominate the \mathbf{k}_I spectra and cover the off-diagonal (cross) peaks, and from the doubled frequency bandwidth of two quantum coherences.

We demonstrate that (Ω_2, Ω_3) correlation plots of \mathbf{k}_{III} for the 74-residue TB6 protein domain (Figure 26)^[270] are more

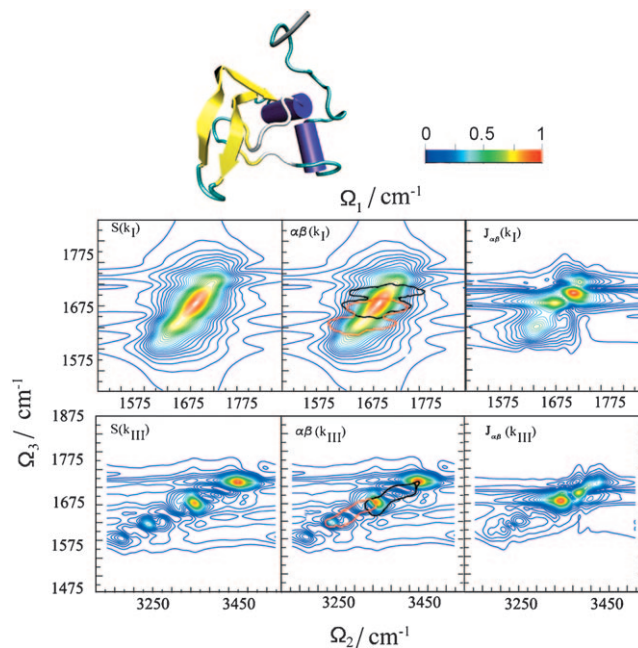


Figure 26. Top row: Simulated signal and sensitivity analysis for the \mathbf{k}_I signal of TB6 protein domain. $S_{\mathbf{k}_I}$ is the signal. $\alpha\beta(\mathbf{k}_I)$ gives the regions related to α helix (red contour) and β sheet (black contour). $J_{\alpha\beta}(\mathbf{k}_I)$ gives the region related to the coupling between α helix (red contour) and β sheet. Bottom row: same quantities for the \mathbf{k}_{III} signal.

sensitive to the couplings between vibrational modes, compared with (Ω_2, Ω_3) correlations in \mathbf{k}_I . We have used sensitivity analysis to assign various regions in congested spectra of globular proteins to specific secondary structures and to separate the overlapping regions. We add a small shift η_v to the energies ϵ_m^v of all modes belonging to the v th secondary structure motif (η_v should be much smaller than all J_{mn}). The difference of the perturbed and the unperturbed spectrum reveals its sensitivity to this perturbation, and its spectral region can then be assigned to the structure of type v . Figure 26 gives the simulated \mathbf{k}_I ($S_{\mathbf{k}_I}$) and \mathbf{k}_{III} ($S_{\mathbf{k}_{III}}$) signal and shows the dissected signal related to helix and hairpin segments and their couplings.

9. Chirality Effects: Enhancing the Resolution

Pulse polarizations provide a whole host of convenient control-parameters that may be easily varied to manipulate the 2DIR signals. We label a coherent heterodyne third-order

signal $\nu_s\nu_3\nu_2\nu_1$, where the three incoming pulses are polarized along the ν_1, ν_2, ν_3 directions and the signal is polarized along ν_4 , as (Figure 27).

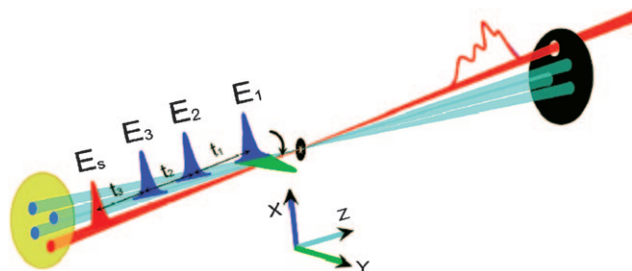


Figure 27. Pulse configuration for femtosecond coherent IR correlation spectroscopy. Three laser pulses (light blue) interact with the sample. The fourth pulse (red) is used to detect its nonlinear response. The control parameters are the time intervals between pulses t_1, t_2, t_3 . All the pulses propagate along the z direction (collinear). The nonchiral signal $xxxx$ is generated when all the pulses are polarized along x (blue and red). The chirality induced xyx signal is obtained by switching the first pulse polarization direction to y (green).

Molecules are typically smaller than the optical wavelength and their response may be adequately described by assuming that the field is uniform across the molecule; this is known as the dipole (or long wavelength) approximation. Our analysis so far was restricted to this limit. We further assumed that all pulses are polarized in parallel and did not need to specify the pulse polarizations. The nonlinear response generally depends on the orientationally averaged product of four dipoles $\langle \mu_m^{\nu_s} \mu_n^{\nu_3} \mu_k^{\nu_2} \mu_l^{\nu_1} \rangle$. In isotropic samples there are only three independent polarization configurations: $xyxy, xyx$, and $xyyx$. All other configurations can be expressed by their linear combinations.

The variation of the phase of the optical field at different points within the molecule may result in new contributions to the signal. These are caused by interferences among signals generated at different parts of the molecules and are typically 1000-times weaker than the leading (dipole) contributions (this is the ratio of chromophore size to the optical wavelength). However, by choosing polarization configurations for which the dipole term vanishes (e.g. $xxxy$), the non-dipole signals are background-free and may be readily detected. These signals change their signs upon mirror reflection; hence they vanish in racemates and in nonchiral molecules and only exist in chiral systems.

Circular dichroism (CD), the difference in the absorption of left- and right-handed circularly polarized light,^[271–273] is the simplest chiral signal. This linear 1D technique is routinely applied for probing the folding states and conformations of proteins. CD spectra have positive and negative components and the contributions of different chromophores interfere (the absorption spectrum in contrast is positive and additive and contains no interference). This property is the reason for the extra sensitivity to structure, allowing the CD technique to distinguish between various secondary structures of proteins. Similarly the structural sensitivity of 2D techniques can be greatly enhanced by a judicious choice of chiral polarization configurations. Chirality-induced (CI) 2D techniques are

extensions of CD to nonlinear spectroscopy.^[274,275] Chirality can also be measured by the Raman optical activity technique (ROA),^[276] which measures the difference in the Raman intensities induced by right and left circularly polarized incident light. Vibrational CD (VCD) band shapes are characteristic to secondary structures of polypeptides. Protonated α -helical structure give bisignate amide-I and amide-A bands,^[277,278] and a monosignate amide-II band.^[279] The amide-I has three peaks for right-handed helices upon deuteration.^[279] α -Helix and antiparallel β -sheets are distinguishable by the amide-I frequency shift and the band shapes change from the bisignate form with a small peak splitting to two well-separated negative peaks.^[280] The amide-I band shape of random-coil structures is also bisignate, but its sign is reversed compared to the α -helix.^[280,281] The 3_{10} helix has a higher frequency amide-II VCD band and a lower frequency amide-II IR band compared to the α -helix. This difference is due to the difference in hydrogen-bond patterns ($4 \rightarrow 1$ vs $5 \rightarrow 1$).^[282]

The response function for a chirality-induced \mathbf{k}_l technique depends on the averaged product [Eq. (38)]^[64] where $\mathbf{j}_e^{\nu}(\mathbf{k})$ is exciton transition dipole in \mathbf{k} space [Eq. (39)].

$$\langle \mathbf{j}_{e_4}^{\nu}(-\mathbf{k}_1 + \mathbf{k}_2 + \mathbf{k}_3) \mathbf{j}_{e_3}^{\nu_3}(\mathbf{k}_3) \mathbf{j}_{e_2}^{\nu_2}(\mathbf{k}_2) \mathbf{j}_{e_1}^{\nu_1}(\mathbf{k}_1) \rangle \quad (38)$$

$$\mathbf{j}_e^{\nu}(\mathbf{k}) = \sum_m e^{i\mathbf{k}\cdot\mathbf{r}_m} \boldsymbol{\mu}_m^{\nu} \psi_{e,m} \quad (39)$$

Molecular chirality is recast to the three-dimensional distribution of local transitions in real space. For simplicity, we neglect the local chirality of each peptide unit (because of their magnetic dipole and electric quadrupole) and only include the global (structural) chirality. Signals sensitive to chirality depend explicitly on the positions of the various local transitions. We define the transition dipole vector for the zero-momentum exciton state as in Equation (40) and the first-order contribution in \mathbf{k} as in Equation (41).

$$\mathbf{j}_e^{\nu} \equiv \mathbf{j}_e^{\nu}(\mathbf{k} = 0) = \sum_m \boldsymbol{\mu}_m^{\nu} \psi_{e,m} \quad (40)$$

$$\bar{\mathbf{j}}_e^{\kappa,\nu} = \sum_m \mathbf{r}_m^{\kappa} \boldsymbol{\mu}_m^{\nu} \psi_{e,m} \quad (41)$$

In these equations, \mathbf{r}_m is the coordinate for the m 'th transition, $\boldsymbol{\mu}_m$ is the transition dipole, and $\psi_{e,m}$ is the exciton wavefunction. Equation (40) is independent of \mathbf{r}_m and insensitive to chirality. Equation (41) goes beyond the dipole approximation. For components such as $xxxx$ with an even number of repeating indices, the first term is finite and will dominate the signal, making it insensitive to chirality. For components with an odd number of repeating indices such as $xxxy$, the first term vanishes and the signal is dominated by the other chiral-sensitive terms. The chirality-induced signals depend on products of the form $\langle \mathbf{r}_{mn}^{\nu_s} \boldsymbol{\mu}_m^{\nu_4} \boldsymbol{\mu}_n^{\nu_3} \boldsymbol{\mu}_k^{\nu_2} \boldsymbol{\mu}_l^{\nu_1} \rangle$. Nonchiral techniques depend only implicitly on the structure through its effect on the frequencies and transition dipoles which

influence peak positions and intensities. The explicit coordinate dependence of the chiral response amplifies the cross-peaks and is the reason why these techniques are more sensitive to fine details of the structure.

In isotropic samples there are three independent chirality-induced polarization configurations for collinear pulses and six additional non-collinear terms.^[61] The signals further depend on the magnitudes and directions of pulse wavevectors. Figure 28 shows the simulated IR chiral response of the amide-I vibrations where all beams propagate along *z*. The electronic CD spectra given for comparison were

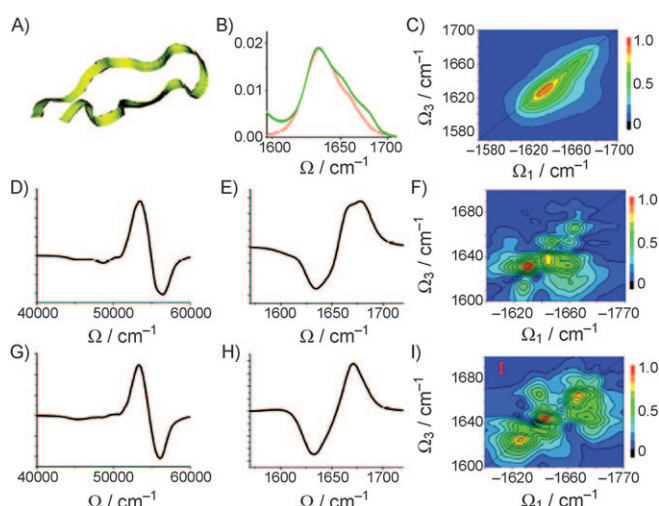


Figure 28. Using chirality-induced 2D correlation spectroscopy to discriminate between the hairpin structures that are indistinguishable by NMR spectroscopy. A) Fifteen-residue hairpin-peptide Trpzip4. B) Simulated (red) and experimental (green)^[17] absorption of the amide-I vibrational band. C) Simulated xxx 2D signals for the amide-I band. Middle and bottom rows: Comparison of the simulated spectra for two configurations drawn from the NMR-determined hairpin-structure ensembles. D and G) Electronic CD spectra of the amide band, E and H) vibrational CD of the amide-I band, and F and I) xxxy chirality induced 2D signals for the amide-I band. The CD signals are similar for the two configurations shown. Major differences of the 2D signals in the cross-peak region indicate specific couplings among vibrational modes.

simulated using Woody's standard exciton model which includes the electric and magnetic moments of the chromophores.^[271] It thus depends on both local and global chirality. Our simulations show how the CI techniques provide complementary information to CD and NMR spectroscopy for a 15-residue hairpin Trpzip4 (Figure 28A),^[283] one of the "Tryptophan Zipper" hairpins. Its robust structure makes Trpzip4 an excellent model for the characterization of the vibrational states of peptides in aqueous solution, for the investigation of the relations of the vibrational spectra with peptide conformations, and for the evaluation of the distributions of structures.^[283] The amide-I absorption band (Figure 28B) consists of three overlapping features; the 1635 cm^{-1} peak and the 1675 cm^{-1} shoulder are related to the β structure,^[283] while the 1655 cm^{-1} shoulder is related to the turn and coil structures at the two ends. The diagonal peaks of 2D xxx signals (Figure 28C) resemble the absorption. NMR

spectra are routinely used for imposing constraints on peptide structure; a distance geometry optimization is then applied to obtain an ensemble of possible conformers consistent with the NMR data.^[8] We focus on the first two conformers out of the 20-reported NMR-spectroscopy determined Trpzip4 structures, which have the lowest energy and are thus the best approximation of the structure. The RMSD between these two structures is 1.517 Å. The calculated electronic (Figure 28D and G) and vibrational CD spectra (Figure 28E and H) of these conformers are similar. However, the 2D chirality-induced spectra (Figure 28F and I) are very different. Conformer I has a strong (1635 cm^{-1} , 1655 cm^{-1}) cross-peak while II has cross-peaks (1655 cm^{-1} , 1675 cm^{-1}).

These examples demonstrate how chirality-induced 2D signals can help determine correlations between different parts of a protein by enhancing certain cross-peaks thereby allowing their assignments to structural features. The cross-peaks are very sensitive to secondary structure variations, and the chiral configuration of different chromophores can be determined from the signs of the corresponding cross-peaks (positive vs. negative cross-peaks between two transitions correspond to different sense of screw configuration of the corresponding transition dipoles). Coherent 2D techniques enhanced by the spatial sensitivity of chirality-induced polarization configurations offer a powerful tool for tracking early protein folding events and pinpointing the average structure and its fluctuations along the folding pathways with femto-second resolution.

Chirality-induced 2D signals are weaker than their non-chiral counterparts, and have not been observed experimentally to date. Nevertheless since they are background-free they may be detected using state-of-the-art IR technology. The collinear pulse configuration presented herein is the simplest such technique. The wavevector selectivity of various techniques is missed in this case, but it can be recovered using phase-cycling techniques as done in NMR spectroscopy.^[23–25, 48–55, 63, 269, 284] Combinations of several carefully arranged non-collinear experiments may lead to the cancellation of nonchiral terms, so that only the chirality-induced terms survive. The pulse configuration may be tailored for probing specific tensor components. For instance, the collinear xxxy signal can be measured in non-collinear geometry whereby all the laser beams are arranged in one (*yz*) plane, the first *y*-polarized beam propagates along *z* and the other *x*-polarized beams can have wavevector component along *y*. All nonchiral contributions vanish for this configuration and only xxxy survives.

10. The Structure of Amyloid Fibrils

The accumulation of amyloid deposits,^[285] whose dominant component is a 39–43 residue A β peptide,^[286] has been identified as a major feature of the pathogenesis of Alzheimer's disease (AD).^[287] Despite their identical 1–39 sequence, the various A β peptides have significantly different biochemical properties: The 42-residue derivative A β 42 deposits much faster than others and the fibrils formed are more stable.^[288] A β 42 is also slightly more hydrophobic, compared

with shorter analogues, such as A β 40, because of the two additional more-hydrophobic residues at the end of the peptide strand.^[289] More importantly, the protease resistance of A β 42 is drastically different from its analogues.^[289]

The structural basis of these property differences is still not fully established. Because of the fibrils are noncrystalline, insoluble, and mesoscopically heterogeneous nature, NMR spectroscopy rather than X-ray crystallography is the primary tool for fibril structure determination.^[285,290] NMR spectroscopy provides various structural constraints that, when combined with computational tools, such as geometry optimization and MD simulations, yield plausible structural models. The model of A β 42 structure was proposed by Riek et al.^[290] and denoted M42. M42 can be dissected into three motifs; 1) residues 1–16 are randomly coiled, 2) residues 26–31 are the turn and 3) the remaining residues form two β strands. NMR structural information is primarily related to the β -strand. As a result of the lack of structural constraints, the turn structure in this model is obtained by geometry optimization and depends heavily on the computational method and the empirical force field. 2D IR spectra were reported recently.^[109,110]

The simulated absorption of M42 (Figure 29 left, panel ABS) shows an intense peak at 1635 cm⁻¹ (a), a shoulder at 1655 cm⁻¹ (b), a peak at 1675 cm⁻¹ (c), two additional peaks

at 1695 cm⁻¹ (d) and 1715 cm⁻¹ (i). Figure 29 left, panel NMD, shows the normal-mode decomposition of the various normal modes into the three structural motifs (β -sheet, turn, and coil). Peaks a, b, and c have strong contributions from both β -strand and coil. Peak d has a contribution from turn plus coil, and peak i is purely turn. Figure 29 left, panel 2D, displays the simulated *xyxy* 2DCS signal. The signal is dominated by strong and broad diagonal peaks that resemble the absorption, no cross-peaks are observed. The contributions of the three structural motifs overlap. The lower resolution and normal-mode delocalization complicate the interpretation of the cross-peaks compared to the NMR spectra. However, isotope-labeling combined with a judicious design of polarization configurations can be used to manipulate the 2DCS signals by enhancing desired spectral features. ¹³C¹⁸O isotope labeling of a given peptide residue induces a 65 cm⁻¹ red shift of the amide-I vibrational frequency, creating peaks well separated from the unlabeled band and providing structural information on labeled segments.

2D signals depend on interferences among many contributions (Liouville space pathways). This interference may be controlled by varying the relative polarizations of the various beams, thereby eliminating diagonal peaks and amplifying the cross-peaks. Below we demonstrate how a coherent control algorithm may be used to manipulate the 2DIR feature of A β 42, and create well-resolved cross-peaks which are directly related to interactions within turn segments and between the turn and the β -sheet. These provide additional constraints for the turn structure.

We have optimized the following of the three linearly independent tensor components $T_j = xyxy$; $xyxy$; $xyyx$ to suppress the diagonal 1655 cm⁻¹ peak [Eq. (42)].

$$W(\omega_1, \omega_3) = \sum_j c_j T_j \quad (42)$$

The coefficients c_j were optimized using a genetic algorithm^[291] aimed at minimizing the control target: the ratio of the integrated diagonal line in the absolute magnitude of the 2D spectrum to the integrated diagonal peak at 1655 cm⁻¹ with $\delta = 10$ cm⁻¹. Fast exponential convergence was achieved using 10 members in a population within 100–200 generations. A much richer cross-peak pattern is seen in the signal (Figure 29 left, panel 2D(CP)) compared with the non-controlled *xxxx* signal (Figure 29 left, panel 2D).

The CP signal of M42 shows two strong cross-peaks related to the correlation between the absorption features d and i. These are displayed in Figure 30 on an expanded scale and marked AB-1 (1695,1715) and AB-2 (1715,1695). The normal modes contributing to the diagonal peaks were projected onto the local amide modes along the backbone to assign the cross-peaks to positions along the structure. The i modes (Figure 30 A:1715) are localized within the turn segment and residue 28 has the largest weight, while the d modes (Figure 30 B:1695) are almost evenly distributed among the coil and the residues 28–30 of the turn. Given the large distance between the coil and the turn (see Figure 30) we expect their interaction to be negligible. We thus conclude

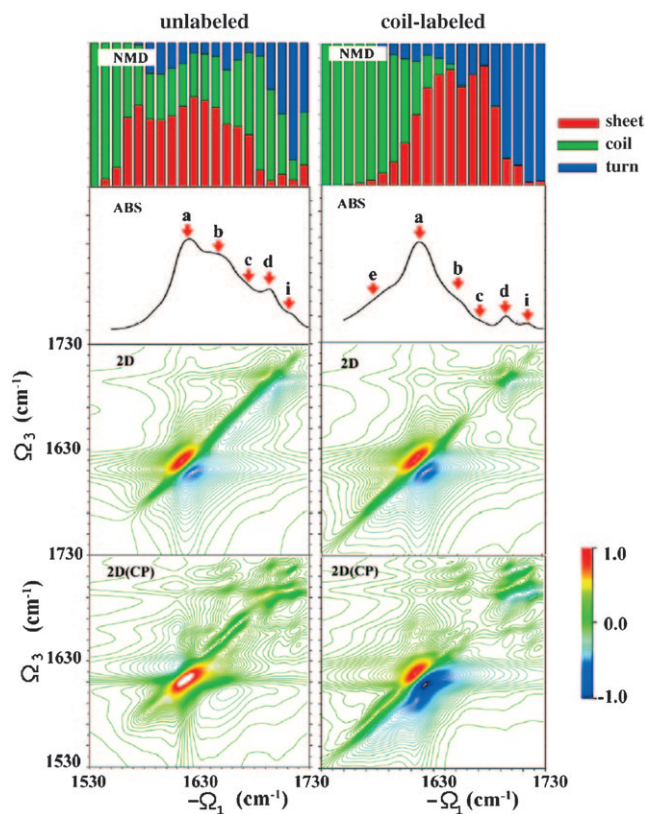


Figure 29. Left: From top to bottom: the normal mode diagram (NMD), the absorption signal (ABS), the *xyxy* polarization 2D cross spectrum (2D), and the coherent-control optimized polarization [2D(CP)] 2D cross spectrum of unlabeled M42 amyloid. In NMD, the β -strand, coil, and turn content are shown in red, green, and blue, respectively. Right: same quantities for the isotope-labeled coil fibril.

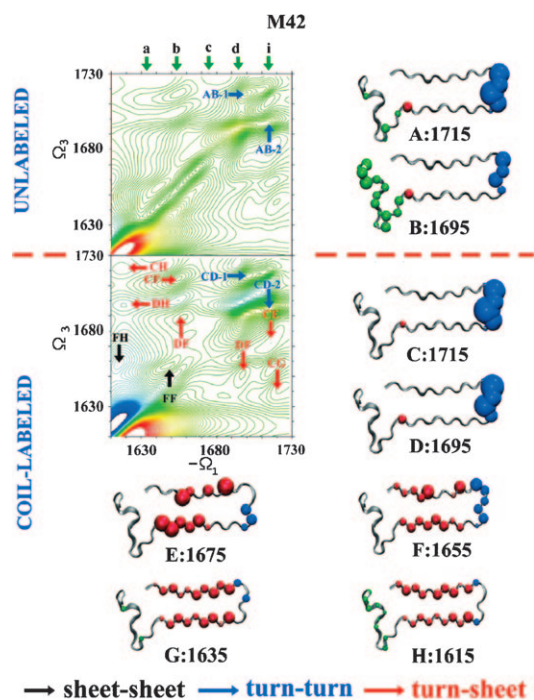


Figure 30. Above the dash line: The 2DCS signal of M42 with coherent-control-optimized polarization configuration (Figure 29, bottom left panel) on an expanded scale (1630–1730 cm^{-1}) and the projection of the normal modes contributing to the specified cross-peaks onto the local amide modes along the backbone. Below the dashed line: Same representation for isotope-labeled coil M42. In the 2DCS plot, the cross-peaks are attributed to the turn–turn interaction (blue arrows), turn–sheet (red), and sheet–sheet (black). In the normal mode projection plots, the contribution from the turn (blue), sheet (red), and coil (green) are shown. Green arrows above the 2DCS denote the positions of absorption maxima.

that these two cross-peaks reflect turn–turn interactions, especially within the residues 28–30.

Most peaks in the M42 spectra contain contributions from more than one structural motif, which will complicate their assignment. Upon isotope labeling of the coil segment (residues 1–16), the peaks will be dominated by one structural motif (Figure 29, right). The new shoulder *e* in the linear absorption (Figure 29 right, panel ABS) is dominated by the coil segment. The components *a*, *b*, and *c* are all dominated by the sheet and *d* and *i* belong to the turn. The 2D spectrum (Figure 29 right, panel 2D) has an improved cross-peak resolution over the unlabeled sample, but the main cross-peak pattern is still unresolved. Our coherent-control method may be employed to eliminate the diagonal peak of the isotopically labeled peptide at 1655 cm^{-1} (Figure 29, right, panel 2D(CP)). Most cross-peaks may now be clearly assigned.

In Figure 30 the signals C:1715 and D:1695 demonstrate that for the coil-labeled sample, peaks *d* and *i* are both dominated by the turn, the cross-peaks CD1 (1695,1715) and CD2 (1715,1695) are thus related to turn–turn interactions. In Figure 30, signals H:1615 and G:1635 shows that the 1615 cm^{-1} and 1635 cm^{-1} frequency windows are dominated by the strand motif. The CH, DH, and CG cross-peaks thus originate from interactions between the turn and the sheet

motifs close to the turn segment (mainly residues 24–25 and residues 32–33). The normal modes in the 1675 cm^{-1} window (Figure 30 E:1675) are also dominated by the sheet motif, the local mode population is non-uniformly distributed and contains no contribution from mode 25. The CE signal thus originates primarily from the interaction between the turn and residue 32. The normal modes 1655 cm^{-1} (Figure 30 F:1655), in contrast, have a significant contribution from both the sheet and the turn, thus the CF, DF1, DF2 peaks should contain mixed information about turn–turn and turn–sheet interaction. The additional cross-peaks FF and FH, marked by black arrows are related to sheet–sheet interactions.

11. Summary and Outlook

The computational arsenal presented herein may be readily applied to describe non-equilibrium processes, provided they are slower than a typical 2D measurement timescale (ca. 200 fs). We can then assume that the system is stationary during the measurement but characterized by time-dependent parameters related to the process under study (e.g. protein folding, conformational change, or hydrogen-bond breaking). 2D spectra could then provide “stroboscopic” snapshots of these processes. The numerical propagation (Figure 20) and the stochastic Liouville equation techniques are not restricted to this limit and may be used to describe an arbitrary timescale of the dynamics (fast or slow dynamics compared to the measurement).

It is instructive to point out some fundamental connections between 2D spectroscopy and another rapidly developing field of single-molecule spectroscopy.^[292] In the course of time, each molecule in an ensemble undergoes a stochastic evolution and its properties, for example, frequencies, orientations, dipole moments fluctuate through couplings with uncontrollable external “bath” degrees of freedom. Bulk measurements probe the ensemble average of these stochastic trajectories. Single-molecule spectroscopy dissects the ensemble by “brute force”: observing individual trajectories one molecule at a time. It thus provides considerably more detailed information than bulk measurements. Nonlinear spectroscopy accomplishes a similar goal by observing the entire ensemble but at multiple time points. There are many possible microscopic models with very different types of trajectories that could yield the same ensemble average at a given time. The multipoint correlation functions obtained by nonlinear spectroscopy have the capacity to distinguish between such models, even though individual trajectories are not observed. Consider, for example, a chemically reactive $A \rightleftharpoons B$ system at equilibrium. If the reaction rates are slow on the spectroscopic time scale, the absorption spectrum will be simply given by the weighted average of species A and B; No information about the kinetics is available from 1D spectroscopy. In a 2D measurement the time delay t_2 can be varied on the kinetic timescale so as to extract the kinetics from the time evolution of the cross-peaks. The cross-peaks give the joint probability of the system to be in A during t_1 and B during t_3 . Typically t_1 and t_3 are controlled by dephasing and are much shorter than t_2 . This is

therefore a two-point measurement separated by t_2 . This is complementary to triggered experiments in which the system is perturbed out of equilibrium and the subsequent relaxation is monitored.^[92,293] Single-molecule spectroscopy is a long (microsecond and longer) time-measurement. 2DIR can provide trajectory information on the femtosecond timescale. A common thread to both techniques is the analysis in terms of *ensembles of trajectories* rather than of *configurations*.^[294]

Over the past decade, 2DIR has established itself as a useful spectroscopic tool for the investigation of molecular structures and ultrafast molecular events. The technique has a lower structural resolution than NMR spectroscopy, but its unique high temporal resolution and different observation window make it an invaluable complementary tool to NMR spectroscopy.

Early studies were of the proof-of-concept kind and focused on demonstrating the various capabilities and potentials of this technique. Current activity in the field focuses on identifying specific systems where 2DIR can be particularly helpful. Developing the necessary methods for quantitatively analyzing the 2DIR signals is a major challenge. A concerted experimental and the theoretical effort, will be required to benchmark systems and improve the current methods. We expect it to go through a similar development trajectory to the history of classical force field for molecular mechanic simulations.

A computational package “SPECTRON” has been developed^[55] for simulating 2D signals. We aim at calculating a broad range of linear and nonlinear optical signals of complex biomolecules. SPECTRON includes modules for constructing Hamiltonian operators for 1) the amide-I, -II, -III, -A vibrational bands and $n-\pi^*$, $\pi-\pi^*$ electronic bands for peptides, based on simulations of the MD trajectories, 2) the C=O stretch in guanine, the in-plane or out-of-plane, symmetric or asymmetric NH or NH₂ bend in adenine, the ring C=N stretch in cytosine for RNAs, 3) the O–H stretching band of water, 4) C–O stretching band of membrane lipids. The code was used recently to benchmark various amide maps.^[295] An interface between SPECTRON and standard MD simulation packages, such as CHARMM,^[58] NAMD,^[296] and GROMOS,^[59] allows the MD trajectories to be read directly in ASCII or binary formats. The code can also simulate 2D electronic spectra of aggregates. This application has been reviewed recently^[64] and is not covered in this Review.

This work was supported by the National Institutes of Health Grant GM59230 and the National Science Foundation Grant CHE-0745891. W.Z. thanks UCI Dissertation Fellowship for financial support. Many helpful discussions with Dr. Darius Abramavicius are gratefully acknowledged. We also wish to thank Drs. Cyril Falvo and Lijun Yang for useful comments.

Received: June 5, 2008

Revised: September 17, 2008

[1] L. Stryer, *Biochemistry*, 2nd ed, Freeman, New York, **1995**.

[2] G. Rhodes, *Crystallography Made Crystal Clear: A Guide for Users of Macromolecular Models*, 3rd ed., Academic Press, Burlington, **2006**.

- [3] D. J. Segel, A. Bachmann, J. Hofrichter, K. O. Hodgson, S. Doniach, T. Kiefhaber, *J. Mol. Biol.* **1999**, 288, 489.
- [4] S. Arai, M. Hirai, *Biophys. J.* **1999**, 76, 2192–2197.
- [5] L. Pollack, M. W. Tate, N. C. Darnton, J. B. Knight, S. M. Gruner, W. A. Eaton, R. H. Austin, *Proc. Natl. Acad. Sci. USA* **1999**, 96, 10115–10117.
- [6] T. Uzawa, T. Kimura, K. Ishimori, I. Morishima, T. Matsui, M. Ikeda-Saito, S. Takahashi, S. Akiyama, T. Fujisawa, *J. Mol. Biol.* **2006**, 357, 997–1008.
- [7] M. Pfuhl, P. C. Driscoll, *Philos. Trans. R. Soc. London Ser. A* **2000**, 358, 513–545.
- [8] K. Wüthrich, *NMR of Proteins and Nucleic Acids*, Wiley, New York, **1995**.
- [9] B. Gruenewald, C. U. Nicola, A. Lustig, G. Schwarz, H. Klump, *Biophys. Chem.* **1979**, 9, 137–147.
- [10] R. R. Ernst, G. Bodenhausen, A. Wokaun, *Principles of Nuclear Magnetic Resonance in One and Two Dimensions*, Clarendon, Oxford, **1987**.
- [11] C. Rose-Petruck, R. Jimenez, T. Guo, A. Cavalleri, C. W. Siders, F. Raksi, J. A. Squier, B. C. Walker, K. R. Wilson, C. P. J. Barty, *Nature* **1999**, 398, 310–312.
- [12] M. Chergui, A. H. Zewail, *ChemPhysChem*, **2009**, 10, 28–43.
- [13] A. H. Zewail, *Physical Biology, From Atoms to Medicine*, Imperial College Press, London, **2008**.
- [14] W. A. Eaton, V. Munoz, S. J. Hagen, G. S. Jas, L. J. Lapidus, E. R. Henry, J. Hofrichter, *Annu. Rev. Biophys. Biomol. Struct.* **2000**, 29, 327–359.
- [15] *Applications of Vibrational Spectroscopy in Life, Pharmaceutical and Natural Sciences* (Eds.: J. M. Chalmers, P. R. Griffiths), Wiley, New York, **2002**.
- [16] M. Hein, A. A. Wegener, M. Engelhard, F. Siebert, *Biophys. J.* **2003**, 84, 1208–1217.
- [17] R. Brudler, R. Rammelsberg, T. T. Woo, E. D. Getzor, K. Gerwert, *Nat. Struct. Biol.* **2001**, 8, 265–270.
- [18] M. Aki, T. Ogura, K. Shinzawa-Itoh, S. Yoshikawa, T. Kitagawa, *J. Phys. Chem. B* **2000**, 104, 10765–10774.
- [19] S. A. Asher, A. Ianoul, G. Mix, M. N. Boyden, A. Karnoup, M. Diem, R. Schweitzer-Stenner, *J. Am. Chem. Soc.* **2001**, 123, 11775–11781.
- [20] E. W. Blanch, L. A. Morozova-Roche, D. A. E. Cochran, A. J. Doig, L. Hecht, L. D. Barron, *J. Mol. Biol.* **2000**, 301, 553–563.
- [21] M. H. Cho, *Chem. Rev.* **2008**, 108, 1331–1418.
- [22] J. Bredenbeck, J. Helbing, C. Kolano, P. Hamm, *ChemPhysChem* **2007**, 8, 1747–1756.
- [23] C. Scheurer, S. Mukamel, *J. Chem. Phys.* **2001**, 115, 4989.
- [24] C. Scheurer, S. Mukamel, *J. Chem. Phys.* **2002**, 116, 6803–6816.
- [25] C. Scheurer, S. Mukamel, *Bull. Chem. Soc. Jpn.* **2002**, 75, 989–999.
- [26] K. W. Kwak, S. Park, M. D. Fayer, *Proc. Natl. Acad. Sci. USA* **2007**, 104, 14221–14226.
- [27] R. Venkatramani, S. Mukamel, *J. Chem. Phys.* **2002**, 117, 11089–11101.
- [28] *Chem. Phys.* **2007**, 341(1–3) (special issue: “Ultrafast Dynamics of Molecules in the Condensed Phase”).
- [29] W. Zhao, J. C. Wright, *J. Am. Chem. Soc.* **1999**, 121, 10994–10998.
- [30] E. I. Shakhnovich, *Curr. Opin. Struct. Biol.* **1997**, 7, 29–40.
- [31] M. Karplus, J. A. McCammon, *Nat. Struct. Biol.* **2002**, 9, 646–652.
- [32] J. A. McCammon, S. C. Harvey, *Dynamics of Proteins and Nucleic Acids*, Cambridge University Press, Cambridge, **1987**.
- [33] X. Daura, K. Gademann, H. Schäfer, B. Jaun, D. Seebach, W. F. van Gunsteren, *J. Am. Chem. Soc.* **2001**, 123, 2393–2404.
- [34] J. N. Onuchic, Z. Luthey-Schulten, P. G. Wolynes, *Annu. Rev. Phys. Chem.* **1997**, 48, 545–600.
- [35] J. D. Bryngelson, J. N. Onuchic, N. D. Socci, P. G. Wolynes, *Proteins Struct. Funct. Genet.* **1995**, 21, 167–195.

- [36] P. G. Wolynes, J. N. Onuchic, D. Thirumalai, *Science* **1995**, 267, 1619–1620.
- [37] S. Gnanakaran, H. Nymeyer, J. Portman, K. Y. Sanbonmatsu, A. E. Garcia, *Curr. Opin. Struct. Biol.* **2003**, 13, 168–174.
- [38] Y. Duan, P. Kollman, *Science* **1998**, 282, 740.
- [39] J. Wang, J. Onuchic, P. Wolynes, *Phys. Rev. Lett.* **1996**, 76, 4861–4864.
- [40] C. D. Snow, B. Zagrovic, V. S. Pande, *J. Am. Chem. Soc.* **2002**, 124, 14548–14549.
- [41] P. L. Freddolino, F. Liu, M. Gruebele, K. Schulten, *Biophys. J.* **2008**, 94, L75–L77.
- [42] Y. Zhu, D. O. V. Alonso, K. Maki, C. Y. Huang, S. J. Lahr, V. Daggett, H. Roder, W. F. DeGrado, F. Gai, *Proc. Natl. Acad. Sci. USA* **2003**, 100, 15486–15491.
- [43] J. Kubelka, W. A. Eaton, J. Hofrichter, *J. Mol. Biol.* **2003**, 329, 625–630.
- [44] C. D. Snow, N. Nguyen, V. S. Pande, M. Gruebele, *Nature* **2002**, 420, 102–106.
- [45] D. Frenkel, B. Smit, *Understanding Molecular Simulation: From Algorithms to Applications*, Academic Press, San Diego, **2002**.
- [46] D. Mohanty, R. Elber, D. Thirumalai, D. Beglov, B. Roux, *J. Mol. Biol.* **1997**, 272, 423–442.
- [47] C. Dellago, P. Bolhuis, F. Csajka, D. Chandler, *J. Chem. Phys.* **1998**, 108, 1964–1977.
- [48] V. Chernyak, W. M. Zhang, S. Mukamel, *J. Chem. Phys.* **1998**, 109, 9587–9601.
- [49] S. Mukamel, A. Piryatinski, V. Chernyak, *J. Chem. Phys.* **1999**, 110, 1711–1725.
- [50] A. Piryatinski, S. Tretiak, V. Chernyak, S. Mukamel, *J. Raman Spectrosc.* **2000**, 31, 125–135.
- [51] A. Piryatinski, V. Chernyak, S. Mukamel in *Ultrafast Infrared and Raman Spectroscopy* (Ed.: M. Fayer), Marcel Dekker, New York, **2001**, pp. 349–382.
- [52] A. Piryatinski, V. Chernyak, S. Mukamel, *Chem. Phys.* **2001**, 266, 311–322.
- [53] C. Scheurer, A. Piryatinski, S. Mukamel, *J. Am. Chem. Soc.* **2001**, 123, 3114–3124.
- [54] A. Piryatinski, S. A. Asher, S. Mukamel, *J. Phys. Chem. A* **2002**, 106, 3524–3530.
- [55] W. Zhuang, D. Abramavicius, T. Hayashi, S. Mukamel, *J. Phys. Chem. B* **2006**, 108, 18034–18045.
- [56] J. P. Wang, J. X. Chen, R. M. Hochstrasser, *J. Phys. Chem. B* **2006**, 110, 7545–7555.
- [57] N. Demirdoven, C. M. Cheatum, H. S. Chung, M. Khalil, J. Knoester, A. Tokmakoff, *J. Am. Chem. Soc.* **2004**, 126, 7981–7990.
- [58] B. R. Brooks, R. E. Bruccoleri, B. D. Olafson, D. J. States, S. Swaminathan, M. Karplus, *J. Comput. Chem.* **1983**, 4, 187–217.
- [59] W. R. P. Scott, P. H. Hünenberger, I. G. Tironi, A. E. Mark, S. R. Billeter, J. Fennen, A. E. Torda, T. Huber, P. Krüger, W. F. van Gunsteren, *J. Phys. Chem. A* **1999**, 103, 3596–3607.
- [60] D. A. Pearlman, D. A. Case, J. W. Caldwell, W. S. Ross, T. E. Cheatham, S. Debolt, D. Ferguson, G. Seibel, P. Kollman, *Comput. Phys. Commun.* **1995**, 91, 1–41.
- [61] D. Abramavicius, S. Mukamel, *J. Chem. Phys.* **2005**, 122, 134305.
- [62] S. Mukamel, D. Abramavicius, *Chem. Rev.* **2004**, 104, 2073–2098.
- [63] S. Mukamel in *Molecular Nonlinear Optics* (Ed.: J. Zyss), Academic Press, New York, **1994**, pp. 1–46.
- [64] D. Abramavicius, B. Palmieri, V. Voronine, F. Šanda, S. Mukamel, *Chem. Rev.* **2008**, in press.
- [65] S. Mukamel, *Annu. Rev. Phys. Chem.* **2000**, 51, 691–729.
- [66] S. Mukamel, *Principles of Nonlinear Optical Spectroscopy*, Oxford University Press, New York, **1995**.
- [67] S. M. George, A. L. Harris, M. Berg, C. B. Harris, *J. Chem. Phys.* **1984**, 80, 83–94.
- [68] L. Allen, J. H. Elberly, *Optical Resonances and Two-Level Atoms*, Wiley, New York, **1975**.
- [69] A. Laubereau, W. Kaiser, *Rev. Mod. Phys.* **1978**, 50, 607–665.
- [70] R. F. Loring, S. Mukamel, *J. Chem. Phys.* **1985**, 83, 2116–2128.
- [71] L. J. Muller, D. Vandembout, M. Berg, *J. Chem. Phys.* **1993**, 99, 810–819.
- [72] D. Vandembout, L. J. Muller, M. Berg, *Phys. Rev. Lett.* **1991**, 67, 3700–3703.
- [73] M. Muller, K. Wynne, J. D. W. Vanvoorst, *Chem. Phys.* **1988**, 125, 225–230.
- [74] S. Mukamel, *Phys. Rev. A* **1983**, 28, 3480–3492.
- [75] S. Mukamel, R. F. Loring, *J. Opt. Soc. Am. B* **1986**, 3, 595–606.
- [76] L. E. Fried, S. Mukamel, *Adv. Chem. Phys.* **1993**, 84, 435.
- [77] Y. Tanimura, S. Mukamel, *J. Chem. Phys.* **1993**, 99, 9496–9511.
- [78] L. J. Kaufman, J. Heo, L. D. Ziegler, G. R. Fleming, *Phys. Rev. Lett.* **2002**, 88, 207402.
- [79] K. Kubarych, C. J. Milne, R. J. D. Miller, *Chem. Phys. Lett.* **2003**, 369, 635–642.
- [80] S. Saito, I. Ohmine, *J. Chem. Phys.* **1998**, 108, 250–251.
- [81] A. Ma, R. M. Stratt, *J. Chem. Phys.* **2002**, 116, 4972–4984.
- [82] K. Okumura, A. Tokmakoff, Y. Tanimura, *J. Chem. Phys.* **1999**, 111, 492.
- [83] S. Mukamel, A. Piryatinski, V. Chernyak, *Acc. Chem. Res.* **1999**, 32, 145–154.
- [84] *Ultrafast Phenomena XIII* (Eds.: R. D. Miller, M. M. Muri-name, N. F. Scherer, A. M. Weiner), Springer, Heidelberg, **2002**.
- [85] T. L. C. Jansen, K. Duppen, J. G. Snijders, *Phys. Rev. B* **2003**, 67, 134206.
- [86] S. Saito, I. Ohmine, *J. Chem. Phys.* **2003**, 119, 9073–9087.
- [87] C. J. Milne, Y. Li, R. J. D. Miller in *Time-Resolved Spectroscopy in Complex Liquids* (Ed.: R. Torre), Springer, New York, **2007**, p. 1.
- [88] S. Palese, J. T. Buontempo, L. Schilling, W. T. Lotshaw, Y. Tanimura, S. Mukamel, R. J. D. Miller, *J. Phys. Chem.* **1994**, 98, 12466–12470.
- [89] Y. L. Li, L. Huang, R. J. D. Miller, T. Hasegawa, Y. Tanimura, *J. Chem. Phys.* **2008**, 128, 234507.
- [90] W. M. Zhang, V. Chernyak, S. Mukamel, *J. Chem. Phys.* **1999**, 110, 5011.
- [91] M. C. Asplund, M. T. Zanni, R. M. Hochstrasser, *Proc. Natl. Acad. Sci. USA* **2000**, 97, 8219–8224.
- [92] C. Kolano, J. Helbing, M. Kozinski, W. Sander, P. Hamm, *Nature* **2006**, 444, 469–472.
- [93] P. Mukherjee, I. Kass, I. Arkin, M. T. Zanni, *Proc. Natl. Acad. Sci. USA* **2006**, 103, 3528–3533.
- [94] T. Brixner, J. Stenger, H. M. Vaswani, M. Cho, R. E. Blanken-ship, G. R. Fleming, *Nature* **2005**, 434, 625–628.
- [95] J. D. Hybl, Y. Christophe, D. M. Jonas, *Chem. Phys.* **2001**, 266, 295–309.
- [96] X. Q. Li, T. H. Zhang, C. N. Borca, S. T. Cundiff, *Phys. Rev. Lett.* **2006**, 96, 57406.
- [97] T. H. Zhang, I. Kuznetsova, T. Meier, X. C. Li, R. P. Mirin, P. Thomas, S. T. Cundiff, *Proc. Natl. Acad. Sci. USA* **2007**, 104, 14227–14232.
- [98] P. Hamm, M. H. Lim, R. M. Hochstrasser, *J. Phys. Chem. B* **1998**, 102, 6123–6138.
- [99] P. Hamm, M. Lim, W. F. DeGrado, R. M. Hochstrasser, *Proc. Natl. Acad. Sci. USA* **1999**, 96, 2036–2041.
- [100] S. Woutersen, P. Hamm, *J. Phys. Chem. B* **2000**, 104, 11316–11320.
- [101] M. T. Zanni, M. C. Asplund, R. M. Hochstrasser, *J. Chem. Phys.* **2001**, 114, 4579–4590.
- [102] C. Fang, J. Wang, Y. S. Kim, A. K. Charnley, W. Barber-Armstrong, A. B. Smith, S. M. Decatur, R. M. Hochstrasser, *J. Phys. Chem. B* **2004**, 108, 10415–10427.

- [103] H. Maekawa, C. Toniolo, A. Moretto, Q. B. Broxterman, N. H. Ge, *J. Phys. Chem. B* **2006**, *110*, 5834–5837.
- [104] A. T. Krummel, P. Mukherjee, M. T. Zanni, *J. Phys. Chem. B* **2003**, *107*, 9165–9169.
- [105] O. F. A. Larsen, P. Bodis, W. J. Buma, J. S. Hannam, D. A. Leigh, S. Woutersen, *Proc. Natl. Acad. Sci. USA* **2005**, *102*, 13378–13382.
- [106] Z. Ganim, H. S. Chung, A. W. Smith, L. P. Deflores, K. C. Jones, A. Tokmakoff, *Acc. Chem. Res.* **2008**, *41*, 432–441.
- [107] V. Volkov, R. Chelli, W. Zhuang, F. Nuti, Y. Takaoka, A. M. Papini, S. Mukamel, R. Righini, *Proc. Natl. Acad. Sci. USA* **2007**, *104*, 15323–15327.
- [108] J. Bredenbeck, A. Ghosh, M. Smits, M. Bonn, *J. Am. Chem. Soc.* **2008**, *130*, 2152–2153.
- [109] S. H. Shim, D. B. Strasfeld, Y. L. Ling, M. T. Zanni, *Proc. Natl. Acad. Sci. USA* **2007**, *104*, 14197–14202.
- [110] C. Paul, J. P. Wang, W. C. Wimley, R. M. Hochstrasser, P. H. Axelsen, *J. Am. Chem. Soc.* **2004**, *126*, 5843–5850.
- [111] Y. S. Kim, L. Liu, P. H. Axelsen, R. M. Hochstrasser, *Proc. Natl. Acad. Sci. USA* **2008**, *105*, 7720–7725.
- [112] J. Bredenbeck, J. Helbing, R. Behrendt, C. Renner, L. Moroder, J. Wachtveitl, P. Hamm, *J. Phys. Chem. B* **2003**, *107*, 8654–8660.
- [113] H. S. Chung, Z. Ganim, K. C. Jones, A. Tokmakoff, *Proc. Natl. Acad. Sci. USA* **2007**, *104*, 14237–14242.
- [114] J. Bredenbeck, J. Helbing, J. R. Kumita, G. A. Woolley, P. Hamm, *Proc. Natl. Acad. Sci. USA* **2005**, *102*, 2379–2384.
- [115] M. Broquier, C. Crepin, H. Dubost, J. P. Galaup, *Chem. Phys.* **2007**, *341*, 207–217.
- [116] J. N. Bandaria, S. Dutta, S. E. Hill, A. Kohen, C. M. Cheatum, *J. Am. Chem. Soc.* **2008**, *130*, 22–23.
- [117] J. F. Cahoon, K. R. Sawyer, J. P. Schlegel, C. B. Harris, *Science* **2008**, *319*, 1820–1823.
- [118] J. C. Deak, S. T. Rhea, L. K. Iwaki, D. D. Dlott, *J. Phys. Chem. A* **2000**, *104*, 4866–4875.
- [119] D. D. Dlott, *Chem. Phys.* **2001**, *266*, 149–166.
- [120] C. J. Fecko, J. D. Eaves, J. J. Loparo, A. Tokmakoff, P. L. Geissler, *Science* **2003**, *301*, 1698–1702.
- [121] J. D. Eaves, J. J. Loparo, C. J. Fecko, S. T. Roberts, A. Tokmakoff, P. L. Geissler, *Proc. Natl. Acad. Sci. USA* **2005**, *102*, 13019–13022.
- [122] J. B. Asbury, T. Steinell, C. Stromberg, S. A. Corcelli, C. P. Lawrence, J. L. Skinner, M. D. Fayer, *J. Phys. Chem. A* **2004**, *108*, 1107–1119.
- [123] D. Kraemer, M. L. Cowan, A. Paarmann, N. Huse, E. T. J. Nibbering, T. Elsaesser, R. J. D. Miller, *Proc. Natl. Acad. Sci. USA* **2008**, *105*, 437–442.
- [124] P. Hamm, M. Lim, R. M. Hochstrasser, *Phys. Rev. Lett.* **1998**, *81*, 5326–5329.
- [125] M. Kozinski, S. Garrett-Roe, P. Hamm, *Chem. Phys.* **2007**, *341*, 5–10.
- [126] C. H. Kuo, R. M. Hochstrasser, *Chem. Phys.* **2007**, *341*, 21–28.
- [127] J. J. Sines, S. A. Allison, J. A. McCammon, *Biochemistry* **1990**, *29*, 9403–9412.
- [128] D. K. Jones-Hertzog, W. L. Jorgensen, *J. Med. Chem.* **1997**, *40*, 1539–1549.
- [129] B. E. Cohen, T. B. McAnaney, E. S. Park, Y. N. Jan, S. G. Boxer, L. Y. Jan, *Science* **2002**, *296*, 1700–1703.
- [130] C. Fang, J. D. Bauman, K. Das, A. Remorino, E. Arnold, R. M. Hochstrasser, *Proc. Natl. Acad. Sci. USA* **2008**, *105*, 1472–1477.
- [131] I. T. Suydam, S. G. Boxer, *Biochemistry* **2003**, *42*, 12050–12055.
- [132] A. Piryatinski, V. Chernyak, S. Mukamel, *Chem. Phys.* **2001**, *266*, 285–294.
- [133] D. V. Kurochkin, S. R. G. Naraharisetty, I. V. Rubtsov, *Proc. Natl. Acad. Sci. USA* **2007**, *104*, 14209–14214.
- [134] Q. Shi, E. Geva, *J. Phys. Chem. A* **2003**, *107*, 9059–9069.
- [135] Y. S. Kim, R. M. Hochstrasser, *Proc. Natl. Acad. Sci. USA* **2005**, *102*, 11185–11190.
- [136] J. R. Zheng, K. Kwak, J. Asbury, X. Chen, I. R. Piletic, M. D. Fayer, *Science* **2005**, *309*, 1338–1343.
- [137] J. Bredenbeck, J. Helbing, K. Nienhaus, G. U. Nienhaus, P. Hamm, *Proc. Natl. Acad. Sci. USA* **2007**, *104*, 14243–14248.
- [138] O. Golonzka, M. Khalil, N. Demirdoven, A. Tokmakoff, *J. Chem. Phys.* **2001**, *115*, 10814–10828.
- [139] T. Miyazawa, T. Shimanouchi, S. I. Mizushima, *J. Chem. Phys.* **1958**, *29*, 611–616.
- [140] M. Tsuboi, T. Onishi, I. Nakagawa, T. Shimanouchi, S. Mizushima, *Spectrochim. Acta* **1958**, *12*, 253–261.
- [141] S. Krimm, J. Bandekar, *Adv. Protein Chem.* **1986**, *38*, 181–364.
- [142] T. Hayashi, W. Zhuang, S. Mukamel, *J. Phys. Chem. A* **2005**, *109*, 9747–9759.
- [143] J. T. Pelton, L. R. McLean, *Anal. Biochem.* **2000**, *277*, 167–176.
- [144] *Infrared Spectroscopy of Biomolecules* (Eds.: H. H. Mantsch, D. Chapman), Wiley-Liss, New York, **1996**.
- [145] T. Wang, Y. J. Zhu, Z. Getahun, D. G. Du, C. Y. Huang, W. F. DeGrado, F. Gai, *J. Phys. Chem. B* **2004**, *108*, 15301–15310.
- [146] H. Torii, M. Tasumi, *J. Raman Spectrosc.* **1998**, *29*, 81–86.
- [147] See Ref. [142].
- [148] T. Hayashi, S. Mukamel, *J. Phys. Chem. B* **2007**, *111*, 11032–11046.
- [149] see Ref. [141].
- [150] H. Torii, M. Tasumi, *J. Chem. Phys.* **1992**, *96*, 3379–3387.
- [151] R. D. Gorbunov, D. S. Kosov, G. Stock, *J. Chem. Phys.* **2005**, *122*, 224904.
- [152] P. Hamm, S. Woutersen, *Bull. Chem. Soc. Jpn.* **2002**, *75*, 985–988.
- [153] T. L. Jansen, A. G. Dijkstra, T. M. Watson, J. D. Hirst, J. Knoester, *J. Chem. Phys.* **2006**, *125*, 044312.
- [154] J. R. Cheeseman, M. J. Frisch, F. J. Devlin, P. J. Stephens, *Chem. Phys. Lett.* **1996**, *252*, 211–220.
- [155] T. Hayashi, H. Hamaguchi, *Chem. Phys. Lett.* **2000**, *326*, 115–122.
- [156] K. A. Merchant, W. G. Noid, R. Akiyama, I. J. Finkelstein, A. Goun, B. L. McClain, R. F. Loring, M. D. Fayer, *J. Am. Chem. Soc.* **2003**, *125*, 13804–13818.
- [157] J. R. Hill, A. Tokmakoff, K. A. Peterson, B. Sauter, D. Zimdars, D. D. Dlott, M. D. Fayer, *J. Phys. Chem.* **1994**, *98*, 11213–11219.
- [158] S. Ham, J. H. Kim, H. Lee, M. H. Cho, *J. Chem. Phys.* **2003**, *118*, 3491–3498.
- [159] K. Kwac, M. H. Cho, *J. Chem. Phys.* **2003**, *119*, 2247–2255.
- [160] J. R. Schmidt, S. A. Corcelli, J. L. Skinner, *J. Chem. Phys.* **2004**, *121*, 8887–8896.
- [161] T. M. Watson, J. D. Hirst, *Mol. Phys.* **2005**, *103*, 1531–1546.
- [162] T. Hayashi, S. Mukamel, *J. Chem. Phys.* **2006**, *125*, 194510.
- [163] T. L. Jansen, J. Knoester, *J. Chem. Phys.* **2006**, *124*, 044502.
- [164] W. Zhuang, D. Abramavicius, T. Hayashi, S. Mukamel, *J. Phys. Chem. B* **2006**, *110*, 3362–3374.
- [165] B. R. Brooks, R. E. Bruccoleri, B. D. Olafson, D. J. States, S. Swaminathan, M. Karplus, *J. Comput. Chem.* **1983**, *4*, 187–217.
- [166] Gaussian 03 (Revision c.01), Technical report, M. J. Frisch et al., **2003**.
- [167] J. Kubelka, T. A. Keiderling, *J. Phys. Chem. A* **2001**, *105*, 10922–10928.
- [168] See Ref. [166].
- [169] T. Hayashi, S. Mukamel, *J. Phys. Chem. A* **2003**, *107*, 9113–9131.
- [170] T. Hayashi, S. Mukamel, *Bull. Korean Chem. Soc.* **2003**, *24*, 1097–1101.
- [171] L. C. Mayne, B. Hudson, *J. Phys. Chem.* **1991**, *95*, 2962–2967.
- [172] H. Guo, M. Karplus, *J. Phys. Chem.* **1992**, *96*, 7273–7287.
- [173] S. Ham, J. H. Kim, H. Lee, M. H. Cho, *J. Chem. Phys.* **2003**, *118*, 3491–3498.
- [174] D. Thouless, *Phys. Rep.* **1974**, *13*, 94–142.

- [175] M. L. Cowan, B. D. Bruner, N. Huse, J. R. Dwyer, B. Chugh, E. T. J. Nibbering, T. Elsaesser, R. J. D. Miller, *Nature* **2005**, *434*, 199–202.
- [176] I. V. Schweigert, S. Mukamel, *Phys. Rev. A* **2008**, *77*, 033802.
- [177] R. A. Marcus, *Adv. Chem. Phys.* **2007**, *106*, 1–6.
- [178] C. Fang, J. Wang, Y. S. Kim, A. K. Charnley, W. Barber-Armstrong, A. B. Smith, S. M. Decatur, R. M. Hochstrasser, *J. Phys. Chem. B* **2004**, *108*, 10415–10427.
- [179] M. Kobus, R. D. Gorbunov, P. H. Nguyen, G. Stock, *Chem. Phys.* **2008**, *347*, 208–217.
- [180] R. Kubo, *J. Math. Phys.* **1963**, *4*, 174.
- [181] R. Kubo in *Advances in Chemical Physics, Vol. XV: Stochastic Processes in Chemical Physics* (Ed.: K. Schuler), Wiley, New York, **1969**, p. 101.
- [182] Y. Tanimura, *J. Phys. Soc. Jpn.* **2006**, *75*, 082001.
- [183] D. Gamliel, H. Levanon, *Stochastic Processes in Magnetic Resonance*, World Scientific, River Edge, **1995**.
- [184] J. H. Freed, G. V. Bruno, C. F. Polnaszek, *J. Phys. Chem.* **1971**, *75*, 3385.
- [185] D. J. Schneider, J. H. Freed in *Advances in Chemical Physics, Vol. LXXIII: Lasers, Molecules, and Methods* (Eds.: J. O. Hirschfelder, R. E. Wyatt, R. D. Coalson), Wiley, New York, **1989**, p. 387.
- [186] R. A. MacPhail, R. G. Snyder, H. L. Strauss, *J. Chem. Phys.* **1982**, *77*, 1118–1137.
- [187] J. J. Turner, C. M. Gordon, S. M. Howdle, *J. Phys. Chem.* **1995**, *99*, 17532–17538.
- [188] F. Sanda, S. Mukamel, *J. Chem. Phys.* **2006**, *125*, 014507.
- [189] S. Woutersen, P. Hamm, *J. Chem. Phys.* **2001**, *114*, 6833–6840.
- [190] R. Schweitzer-Stenner, *Biophys. J.* **2002**, *83*, 523–532.
- [191] R. Schweitzer-Stenner, F. Eker, Q. Huang, K. Griebenow, *J. Am. Chem. Soc.* **2001**, *123*, 9628–9633.
- [192] S. Woutersen, R. Pfister, P. Hamm, Y. Mu, D. S. Kosov, G. Stock, *J. Chem. Phys.* **2002**, *117*, 6833–6840.
- [193] K. Kwac, M. H. Cho, *J. Chem. Phys.* **2003**, *119*, 2256–2263.
- [194] T. L. Jansen, W. Zhuang, S. Mukamel, *J. Chem. Phys.* **2004**, *121*, 10577–10598.
- [195] Y. Mu, D. S. Kosov, G. Stock, *J. Phys. Chem. B* **2003**, *107*, 5064–5073.
- [196] M. Fayer, personal communication.
- [197] D. Eisenberg, W. Kauzmann, *The Structure and Properties of Water*, Oxford University Press, New York, **1969**.
- [198] *The Hydrogen Bond: Recent Developments in Theory and Experiments, Vol. 1–3* (Eds.: P. Schuster, G. Zundel, C. Sandorfy), North-Holland, Amsterdam, **1976**.
- [199] P. Wernet, D. Nordlund, U. Bergmann, M. Cavalleri, M. Odelius, H. Ogasawara, L. A. Naslund, T. K. Hirsch, L. Ojamae, P. Glatzel, L. G. M. Pettersson, A. Nilsson, *Science* **2004**, *304*, 995–999.
- [200] A. H. Romero, P. L. Silvestrelli, M. Parrinello, *J. Chem. Phys.* **2001**, *115*, 115–123.
- [201] E. D. Isaacs, A. Shukla, P. M. Platzman, D. R. Hamann, B. Barbiellini, C. A. Tulk, *Phys. Rev. Lett.* **1999**, *82*, 600–603.
- [202] M. Bernasconi, P. L. Silvestrelli, M. Parrinello, *Phys. Rev. Lett.* **1998**, *81*, 1235–1238.
- [203] A. Luzar, D. Chandler, *Nature* **1996**, *379*, 55–57.
- [204] S. Woutersen, H. J. Bakker, *Nature* **1999**, *402*, 507–509.
- [205] J. H. Guo, Y. Luo, A. Augustsson, J. E. Rubensson, C. Sathe, H. Agren, H. Siegbahn, J. Nordgren, *Phys. Rev. Lett.* **2002**, *89*, 137402.
- [206] *Ultrafast Hydrogen Bonding Dynamics and Proton Transfer Processes in the Condensed Phase* (Eds.: T. Elsaesser, H. J. Bakker), Kluwer, Dordrecht, **2002**.
- [207] R. Laenen, C. Rauscher, A. Laubereau, *Phys. Rev. Lett.* **1998**, *80*, 2622–2625.
- [208] J. Stenger, D. Madsen, P. Hamm, E. T. J. Nibbering, T. Elsaesser, *Phys. Rev. Lett.* **2001**, *87*, 027401.
- [209] R. Rey, K. B. Møller, J. T. Hynes, *Chem. Rev.* **2004**, *104*, 1915–1928.
- [210] C. P. Lawrence, J. L. Skinner, *J. Chem. Phys.* **2002**, *117*, 5827–5838.
- [211] M. Falk, T. A. Ford, *Can. J. Phys.* **1966**, *44*, 1699–1714.
- [212] See Ref. [211].
- [213] S. Yermenko, M. S. Pshenichnikov, D. A. Wiersma, *Chem. Phys. Lett.* **2003**, *369*, 107–113.
- [214] W. S. Benedicht, N. Gailar, E. K. Plyler, *J. Chem. Phys.* **1956**, *24*, 1139–1165.
- [215] S. Woutersen, H. J. Bakker, *Phys. Rev. Lett.* **1999**, *83*, 2077–2080.
- [216] H. Graener, G. Seifert, A. Laubereau, *Phys. Rev. Lett.* **1991**, *66*, 2092–2095.
- [217] R. Laenen, K. Simeonidis, A. Laubereau, *J. Phys. Chem. B* **2002**, *106*, 408–417.
- [218] S. Bratos, J.-Cl. Leicknam, *J. Chem. Phys.* **1994**, *101*, 4536–4546.
- [219] A. J. Lock, S. Woutersen, H. J. Bakker, *J. Phys. Chem. A* **2001**, *105*, 1238–1243.
- [220] J. Stenger, D. Madsen, P. Hamm, E. T. J. Nibbering, T. Elsaesser, *J. Phys. Chem. A* **2002**, *106*, 2341–2350.
- [221] J. Stenger, D. Madsen, J. Dreyer, P. Hamm, E. T. J. Nibbering, T. Elsaesser, *Chem. Phys. Lett.* **2002**, *354*, 256–263.
- [222] A. Piryatinski, C. P. Lawrence, J. L. Skinner, *J. Chem. Phys.* **2003**, *118*, 9672–9679.
- [223] T. Steinel, J. B. Asbury, S. A. Corcelli, C. P. Lawrence, J. L. Skinner, M. D. Fayer, *Chem. Phys. Lett.* **2004**, *386*, 295–300.
- [224] F. Ding, M. T. Zanni, *Chem. Phys.* **2007**, *341*, 95–105.
- [225] S. Garrett-Roe, P. Hamm, *J. Chem. Phys.* **2008**, *128*, 104507.
- [226] T. Hayashi, T. L. Jansen, W. Zhuang, S. Mukamel, *J. Phys. Chem. A* **2005**, *109*, 64–82.
- [227] T. L. Jansen, T. Hayashi, W. Zhuang, S. Mukamel, *J. Chem. Phys.* **2005**, *123*, 114505.
- [228] C. P. Lawrence, J. L. Skinner, *J. Chem. Phys.* **2003**, *118*, 264–272.
- [229] F. Csajka, D. Chandler, *J. Chem. Phys.* **1998**, *109*, 1125–1133.
- [230] R. Laenen, C. Rauscher, A. Laubereau, *J. Phys. Chem. B* **1998**, *102*, 9304–9311.
- [231] I. R. Piletic, D. E. Moilanen, D. B. Spry, N. E. Levinger, M. D. Fayer, *J. Phys. Chem. A* **2006**, *110*, 4985–4999.
- [232] V. V. Volkov, D. J. Palmer, R. Righini, *Phys. Rev. Lett.* **2007**, *99*, 078302.
- [233] D. Cringus, A. Bakulin, J. Lindner, P. Vohringer, M. S. Pshenichnikov, D. A. Wiersma, *J. Phys. Chem. B* **2007**, *111*, 14193–14207.
- [234] Y. R. Shen, *The Principles of Nonlinear Optics*, Wiley, New York, **1984**.
- [235] Y. R. Shen, *Nature* **1989**, *337*, 519–525.
- [236] X. Chen, T. Yang, S. Kataoka, P. S. Cremer, *J. Am. Chem. Soc.* **2007**, *129*, 12272–12279.
- [237] M. Sovago, R. K. Campen, G. W. H. Wurpel, M. Müller, H. J. Bakker, M. Bonn, *Phys. Rev. Lett.* **2008**, *100*, 173901.
- [238] A. Paarmann, T. Hayashi, S. Mukamel, R. J. D. Mirrer, *J. Chem. Phys.* **2008**, *128*, 191103.
- [239] J. Park, J. H. Ha, R. M. Hochstrasser, *J. Chem. Phys.* **2004**, *121*, 7281–7292.
- [240] J. H. Ha, Y. S. Kim, R. M. Hochstrasser, *J. Chem. Phys.* **2006**, *124*, 064508.
- [241] M. Lima, V. Volkov, P. Foggi, R. Chelli, R. Righini, *Biophysics* **2005**, *45*, S85.
- [242] A. M. Dokter, S. Woutersen, H. J. Bakker, *Proc. Natl. Acad. Sci. USA* **2006**, *103*, 15355–15358.
- [243] H. S. Tan, I. R. Piletic, M. D. Fayer, *J. Chem. Phys.* **2005**, *122*, 174501.
- [244] H. S. Tan, I. R. Piletic, R. E. Riter, N. E. Levinger, M. D. Fayer, *Phys. Rev. Lett.* **2005**, *94*, 057405.

- [245] I. R. Piletic, H. S. Tan, M. D. Fayer, *J. Phys. Chem. B* **2005**, *109*, 21273–21284.
- [246] A. M. Dokter, S. Woutersen, H. J. Bakker, *Phys. Rev. Lett.* **2005**, *94*, 178301.
- [247] V. V. Volkov, D. J. Palmer, R. Righini, *J. Phys. Chem. B* **2007**, *111*, 1377–1383.
- [248] A. Ghosh, M. Smits, J. Bredenbeck, M. Bonn, *J. Am. Chem. Soc.* **2007**, *129*, 9608–9609.
- [249] G. Otting, E. Liepinsh, K. Wüthrich, *Science* **1991**, *254*, 974–980.
- [250] S. K. Pal, A. H. Zewail, *Chem. Rev.* **2004**, *104*, 2099–2123.
- [251] S. Habuchi, H. B. Kim, N. Kitamura, *Anal. Chem.* **2001**, *73*, 366–372.
- [252] G. Sposito, N. T. Skipper, R. Sutton, S. H. Park, A. K. Soper, J. A. Greathouse, *Proc. Natl. Acad. Sci. USA* **1999**, *96*, 3358–3364.
- [253] B. Albert, A. Johnson, J. Lewis, M. Raff, K. Roberts, P. Walter, *Molecular Biology of the Cell*, Garland, New York, **2000**.
- [254] K. Simons, E. Ikonen, *Nature* **1997**, *387*, 569–572.
- [255] R. Mendelsohn, *Biochim. Biophys. Acta Biomembr.* **1972**, *290*, 15–21.
- [256] M. R. Bunow, I. W. Levin, *Biochim. Biophys. Acta Lipids Lipid Metab.* **1977**, *489*, 191–206.
- [257] S. F. Bush, H. Levin, I. W. Levin, *Chem. Phys. Lipids* **1980**, *27*, 101–111.
- [258] E. Bicknell-Brown, K. G. Brown, W. B. Person, *J. Am. Chem. Soc.* **1980**, *102*, 5486–5491.
- [259] E. Mushayakarara, I. W. Levin, *J. Phys. Chem.* **1982**, *86*, 2324–2327.
- [260] W. Hübner, H. H. Mantsch, *Biophys. J.* **1991**, *59*, 1261.
- [261] R. N. Lewis, R. N. McElhaney, W. Pohle, H. H. Mantsch, *Biophys. J.* **1994**, *67*, 2367–2375.
- [262] P. B. Hitchcock, R. Mason, K. M. Thomas, G. G. Shipley, *Proc. Natl. Acad. Sci. USA* **1974**, *71*, 3036–3040.
- [263] R. H. Pearson, I. Pascher, *Nature* **1979**, *281*, 499–501.
- [264] H. Hauser, I. Pascher, R. H. Pearson, S. Sundell, *Biochim. Biophys. Acta Rev. Biomembr.* **1981**, *650*, 21–51.
- [265] E. Mushayakarara, N. Albon, I. W. Levin, *Biochim. Biophys. Acta Biomembr.* **1982**, *686*, 153–159.
- [266] A. Blume, W. Hübner, G. Messner, *Biochemistry* **1988**, *27*, 8239–8249.
- [267] R. N. Lewis, R. N. McElhaney, *Biophys. J.* **1992**, *61*, 63–77.
- [268] V. Volkov, F. Nuti, Y. Takaoka, R. Chelli, A. M. Papini, R. Righini, *J. Am. Chem. Soc.* **2006**, *128*, 9466–9470.
- [269] P. F. Tian, D. Keusters, Y. Suzuki, W. S. Warren, *Science* **2003**, *300*, 1553–1555.
- [270] X. M. Yuan, A. K. Downing, V. Knott, P. A. Handford, *EMBO J.* **1997**, *16*, 6659–6666.
- [271] R. W. W. N. Berova, R. W. Woody, K. Nakanishi, *Circular Dichroism. Principles and Applications*, 2. Aufl., Wiley, New York, **2000**.
- [272] L. A. Nafle, *Annu. Rev. Phys. Chem.* **1997**, *48*, 357–386.
- [273] L. D. Barron, *Molecular Light Scattering and Optical Activity*, 2. Aufl., Cambridge University Press, Cambridge, **2004**.
- [274] K. K. Lee, C. Joo, S. Yang, H. Han, M. Cho, *J. Chem. Phys.* **2007**, *126*, 054505.
- [275] J. H. Choi, M. Cho, *J. Phys. Chem. A* **2007**, *111*, 5176–5184.
- [276] L. D. Barron, L. Hecht, E. W. Blanch, A. F. Bell, *Prog. Biophys. Mol. Biol.* **2000**, *73*, 1–49.
- [277] R. D. Singh, T. A. Keiderling, *Biopolymers* **1981**, *20*, 237–240.
- [278] B. B. Lal, L. A. Nafle, *Biopolymers* **1982**, *21*, 2161–2183.
- [279] A. C. Sen, T. A. Keiderling, *Biopolymers* **1984**, *23*, 1519–1532.
- [280] S. C. Yasui, T. A. Keiderling, *J. Am. Chem. Soc.* **1986**, *108*, 5576–5581.
- [281] S. C. Yasui, T. A. Keiderling, *Biopolymers* **1986**, *25*, 5–15.
- [282] S. C. Yasui, T. A. Keiderling, G. M. Bonora, C. Toniolo, *Biopolymers* **1986**, *25*, 79–89.
- [283] D. G. Du, Y. J. Zhu, C. Y. Huang, F. Gai, *Proc. Natl. Acad. Sci. USA* **2004**, *101*, 15915–15920.
- [284] K. Schulten, personal communication.
- [285] R. Tycko, *Curr. Opin. Chem. Biol.* **2000**, *4*, 500–506.
- [286] M. A. Findeis, *Biochim. Biophys. Acta Mol. Basis Dis.* **2000**, *1502*, 76–84.
- [287] J. Kang, H. G. Lemaire, A. Unterbeck, J. M. Salbaum, C. L. Masters, K. H. Grzeschik, G. Multhaup, K. Beyreuther, B. Müller-Hill, *Nature* **1987**, *325*, 733–736.
- [288] D. Burdick, B. Soreghan, M. Kwon, J. Kosmoski, M. Knauer, A. Henschen, J. Yates, C. Cotman, C. Glabe, *J. Biol. Chem.* **1992**, *267*, 546–554.
- [289] M. Knauer, B. Soreghan, D. Burdick, J. Kosmoski, C. Glabe, *Proc. Natl. Acad. Sci. USA* **1992**, *89*, 7437–7441.
- [290] T. Luhrs, C. Ritter, M. Adrian, D. Riek-Loher, B. Bohrmann, H. Doeli, D. Schubert, R. Riek, *Proc. Natl. Acad. Sci. USA* **2005**, *102*, 17342–17347.
- [291] D. Voronine, D. Abramavicius, S. Mukamel, *J. Chem. Phys.* **2008**, *94*, 3613–3619.
- [292] *Theory, Modelling and Evaluation of Single Molecule Measurements* (Eds.: E. Barkai, M. Orrit, F. Brown H. Yang), World Scientific, Singapore, **2008**.
- [293] P. Hamm, S. M. Ohline, W. Zinth, *J. Chem. Phys.* **1997**, *106*, 519–529.
- [294] P. L. Geissler, C. Dellago, D. Chandler, J. Hutter, M. Parrinello, *Science* **2001**, *291*, 2121–2124.
- [295] H. Maekawa, W. Zhuang, C. Toniolo, S. Mukamel, D. J. Tobias, N.-H. Ge, *J. Phys. Chem B* (in press).
- [296] J. C. Phillips, R. Braun, W. Wang, J. Gumbart, E. Tajkhorshid, E. Villa, C. Chipot, R. D. Skeel, L. Kale, K. Schulten, *J. Comput. Chem.* **2005**, *26*, 1781–1802.
- [297] This is not the case in NMR spectroscopy (see Table 1) in which the signal is generated in all directions.